

UNIVERSITEIT VAN PRETORIA
UNIVERSITY OF PRETORIA
YUNIBESITHI YA PRETORIA

An investigation on the influence of various heat treatments of Nb-Ti-V and V-N microalloyed steels for high strength and low-temperature impact toughness

by

Patrick Isaac Edwin Kambilinya

Supervised by

Prof. Charles W. Siyasiya

Prof. Roelf J. Mostert

Submitted in partial fulfilment of the requirements for the degree Master of Science (Applied Science) in Metallurgical Engineering

in the

Department of Materials Science and Metallurgical Engineering

Faculty of Engineering, Built Environment and Information Technology

UNIVERSITY OF PRETORIA

August 2021

ABSTRACT

The requirement for a combination of high yield strength (≥345 MPa) and impact toughness at low temperatures, typically, CVN 40 to 60 J at –20 °C, is stringent in wind tower applications of normalised Nb-Ti-V and VN microalloyed plate steel grades. In many cases, coarse and banded as-hot rolled microstructures persist even after normalising heat treatment and this leads to inconsistencies and some scatter in the mechanical properties. Hence, homogeneous microstructures are a requirement for consistent mechanical properties in normalised microalloyed plate steels. Therefore, this work focused on the response of the study-microalloyed steels to different heat treatment cycles while considering the effects of the starting as hot-rolled microstructural banding (ferrite-pearlite). The study was conducted on two grades of hot rolled microalloyed plate steels, namely; *0.13C-NbTiV* 30 mm plate steel and *0.12C-VN* 16 mm plate steel (mass %) which were industrially hot rolled differently but subjected to the same heat treatment cycles to study their response to the applied heat treatment routes. In other words, this study focused on the microstructural evolution and the subsequent mechanical properties of these steel grades after various heat treatment cycles that simulated their respective cooling rates in air. Three thermal cycles were applied, namely; normalising heat treatment (NHT), a double austenitisation heat treatment (DAHT) that involved full austenitisation followed by intercritical-austenitisation, and intercritical annealing heat treatment (IAHT).

Characterisation of the as hot-rolled material showed that both steel grades' microstructures were banded, with anisotropy indices of 1.13 and 1.31 for the 30 mm thick NbTiV and 16 mm thick VN-steel plates, respectively, showing that the VN-steel was more banded than the NbTiV-steel. A ferrite grain size gradient was also evident from the surface to the centre of the steel plates in the as-hot rolled condition. The average ferrite grain sizes of the as-hot rolled microstructures were 25.8±2.8 µm and 20.3±2 µm for the NbTiV and VN-steel respectively. In the as-hot rolled condition, the VN plate steel underwent larger deformation (93.3% reduction) than the NbTiV plate steel (87.5% reduction). This can explain the finer ferrite grain size and the higher degree of banding of the VN-steel in the as-hot rolled condition.

After applying the three heat treatments, the grain size gradient was no longer visible in both steel grades, and ferrite grain refinement was evident in the NHT and DAHT, which showed comparable mean ferrite grain size distributions. The NbTiV-steel exhibited a finer average ferrite grain size distribution after the NHT and DAHT than the VN-steel. In the NbTiV-steel, the mean ferrite grain sizes after the NHT, DAHT and IAHT were; 11±1 µm, 12±1 µm, and 18±2 µm respectively. The VN-steel's mean ferrite grain sizes after the NHT, DAHT and IAHT were; 18±1 µm, 16±1.8 µm, and 27±2 µm respectively. Regarding pearlite banding in the NbTiV-steel, the DAHT and IAHT

processes produced a more uniform pearlite distribution, while the NHT retained the pearlite banded microstructure, however, the IAHT produced a bimodal ferrite grain size distribution and the coarsest mean ferrite grain size relative to those from the NHT and DAHT. The VN-steel exhibited a similar trend but to a lesser extent, that is, it had a stronger memory of the as-hot rolled microstructure. This led to the deduction that a higher degree of banding in the as-hot rolled condition correlated to greater retention of microstructural banding after applied heat treatment. In general, of the three heat treatments, the DAHT cycle proved to be the most effective in eliminating the microstructural banding for both steel grades despite the initial as-hot rolled conditions of the study-steels.

Regarding mechanical properties of both steel grades, the NHT produced the highest yield strength, R_p (NbTiV– 404±9 MPa & VN– 377±1.5 MPa) and fracture elongation, A_5 (NbTiV– 31±0.6% & VN– 33±0.5%), which could be attributed to the ferrite grain size refinement. Despite yielding similar average ferrite grain size distributions with the NHT, the DAHT produced a lower yield strength relative to the NHT which ascribes to some loss of precipitation strengthening associated with the second annealing process of the DAHT. The lowest yield strength was observed after the IAHT due to the bimodal and coarse mean ferrite grain structure. In the NbTiV, the DAHT produced the R_p of 355±12 MPa and A_5 of 27±1%; while the IAHT produced R_p and A_5 values of 350±1 MPa and 27±0.5% respectively. In the VN, the DAHT produced the R_p of 345±20 MPa and A_5 of 29±2.5%; while the IAHT produced R_p and A_5 values of 359±3.5 MPa and 32±1.5% respectively. The highest R_m was achieved in the IAHT for both study-steels; with NbTiV– 543±4 MPa and VN– 512±3 MPa. These high ultimate tensile strength results produced by the IAHT could be attributed to pearlite strengthening by carbon enrichment of the austenite during intercritical austenitisation. Numerically the DAHT produced the highest CVN upper shelf energy values (though with a minimal difference to that of the NHT) in both steel grades;- NbTiV– 259 J and VN – 293 J, possibly due to the refined ferrite grain structure. However, the best impact toughness at –40 °C was achieved with the NHT (NbTiV– 196 J & VN– 210 J). In general, the best combination of strength and impact toughness was achieved with the NHT process. The IAHT produced the lowest impact toughness properties in both steel grades which can be ascribed to the coarseness and bimodality of the ferrite grain structure after the IAHT. Finally, the results after the heat treatment cycles showed higher impact toughness properties for the VN-steel than the NbTiV-steel, and contrastingly, higher tensile properties for the NbTiV-steel than the VN-steel. The yield strength specification requirements for structural applications in the NbTiV-steel were well met after the NHT and DAHT, and just marginally met after the IAHT. However, all the heat treatment cycles adequately met the CVN impact toughness specifications for structural applications in both steel grades. In the VN-steel on the other hand, the yield strength specification requirements were again well met after the NHT, followed by the IAHT and failed to be met after the DAHT.

RESEARCH OUTPUTS

Conference proceedings: *Conference of the South African Advanced Materials Initiative*

1. P. I. Kambilinya, C. W. Siyasiya, K. M. Banks, and R. J. Mostert, “Effect of intercritical annealing of normalised Nb-Ti-V microalloyed plate steel on microstructural evolution,” *in IOP Conf. Ser.: Mater. Sci. Eng. 655 012004,* 2019.

DECLARATION

I declare that the dissertation, which I hereby submit for the degree Master of Science (Applied Science) in Metallurgical Engineering at the University of Pretoria, is my work and has not previously been submitted by me for a degree at this or any other tertiary institution.

ETHICS STATEMENT

The author, whose name appears on the title page of this thesis, has obtained, for the research described in this work, the applicable research ethics approval.

The author declares that he has observed the ethical standards required in terms of the University of Pretoria's Code of Ethics for Researchers and the Policy guidelines for responsible research.

Signature : 

Student name : Patrick Isaac Edwin Kambilinya

Date : 05 August 2021

ACKNOWLEDGEMENTS

Above all, glory and thanks be to God Almighty who gave me the grace, strength, wisdom and guidance throughout the research journey.

This journey was made bearable and possible because of the insightful input offered by several individuals. I express my earnest gratitude to my supervisor and mentor, Professor C.W. Siyasiya for the support, guidance, valuable time, encouragement, and incisive knowledge that you provided throughout my research study. I appreciate and take nothing for granted. I also extend my gratitude to my co-supervisor Professor R.J. Mostert for the critical and constructive reproval along my research journey, your perceptions were hugely valued and considered in the building up of this manuscript and my research skills as a whole. I am also greatly grateful to Professor W. Stumpf, who has always been a mentor to me throughout my studies, for all the advice, inspirations, insights, encouragement to always take up challenges, solve problems, and instilled in me the metallurgical perspective.

I also acknowledge all the colleagues that rendered support in many ways, directly and indirectly: Dr K. Annan, Rorisang Maubane, Gabi, Kedibone, Tulani, Tresor, Lwazi, Pride Masukume. Acknowledgements to ArcelorMittal South Africa for the provision of the studied materials and financial support.

Finally, I also extend my sincere gratitude to my family and friends for all the support that you rendered to me, for all the prayers and encouragements, for having faith in me. Acknowledgements to the Awitty family, for all the support you provide. Many thanks to my fiancée, Sarah, who has always encouraged me, prayed for me and always believed in me to complete this journey.

DEDICATION

I dedicate this thesis to my parents. You made selfless and immeasurable sacrifices so that I could achieve this milestone, I hope I have made you proud and have made your sacrifices worthwhile. May God continue blessing you.

Table of Contents

CHAPTER 1 INTRODUCTION 1

1.1 Background and Significance 1

1.2 Problem Statement 4

1.3 Scope of Study 4

1.4 Study Objectives 4

CHAPTER 2 LITERATURE REVIEW 5

2.1 Introduction 5

2.2 Historical Background of HSLA Steels 5

2.3 Influence of Microalloying Elements 6

2.3.1 Niobium 7

2.3.2 Vanadium 9

2.3.3 Titanium 11

2.4 Nil-recrystallisation Temperature (T_{NR}) Empirical Models 14

2.5 Thermo-Calc Software Predictions 15

2.6 Microstructural Banding 17

2.6.1 Evolution of microstructural banding 18

2.6.2 Influence of microstructural banding on mechanical properties 29

2.7 Impact of Heat Treatment on Banding and Mechanical Properties 32

2.7.1 Normalising heat treatment 32

2.7.2 Intercritical heat treatment 36

2.8 Conclusion 42

CHAPTER 3 EXPERIMENTAL PROCEDURE 43

3.1 Introduction 43

3.2 Specimen Materials 43

3.3 Metallography 44

3.3.1 Optical Microscopy 44

3.3.2 Grain size measurements 45

3.3.3 Characterisation of the banding extent in as hot-rolled microstructures 46

3.3.4 Scanning Electron Microscopy 47

3.4 Thermal Analysis 47

3.4.1 Furnace 47

3.4.2 Bähr Dilatometry 47

3.4.3 Gleeble thermomechanical simulator 50
3.5 Mechanical Testing 51
3.5.1 Hardness measurements 51
3.5.2 Tensile testing 52
3.5.3 Charpy V-notch testing 52
3.6 Thermo-Calc^{TM} Predictions 54
3.7 T_{NR} Predictions of the Study-steels 56

CHAPTER 4 EXPERIMENTAL RESULTS 57
4.1 Introduction 57
4.2 Dilatometric Analysis 57
4.3 Microstructural Characterisation of the As-hot rolled Material 60
4.3.1 Ferrite grain size and degree of banding measurements 60
4.4 Influence of Austenitising Temperature on PAGS and Banding 63
4.5 Impact of Applied Heat Treatments on Microstructural Evolution 67
4.6 Impact of Applied Heat Treatments on Mechanical Properties 77
4.6.1 Tensile test results 77
4.6.2 Work hardening behaviour of the heat-treated samples. 78
4.6.3 Hardness 79
4.6.4 Charpy V-notch impact toughness 79
4.7 Fractographic Analysis of the CVN Fracture Surfaces 81

CHAPTER 5 ANALYSIS AND DISCUSSION 85
5.1 Introduction 85
5.2 Effect of Heat Treatment on the Microstructural Evolution of The NbTiV and VN Microalloyed Steels 85
5.2.1 Normalising Heat Treatment (NHT) 85
5.2.2 Double Austenitisation Heat Treatment (DAHT) 87
5.2.3 Intercritical Annealing Heat Treatment (IAHT) 88
5.3 Impact of Heat Treatment on Mechanical Properties of NbTiV And VN Microalloyed Steels 90
5.3.1 Tensile properties 90
5.3.2 Charpy V-Notch impact toughness 92

CHAPTER 6 CONCLUSIONS AND RECOMMENDATIONS 94
6.1 Conclusions 94

6.2 Recommendations 95

CHAPTER 7 REFERENCES 96

CHAPTER 8 APPENDIX A 110

8.1 A.1 Parameters for Assessing the Degree of Banding 110

8.2 A.2 Cooling Profile Excel Template 112

8.3 A.3 NbTiV-steel Intercritical Annealing Thermo-Calc Predictions 113

8.4 A.4 VN-steel Intercritical Annealing Thermo-Calc Predictions 114

8.5 A.5 As-hot rolled Ferrite Grain Size Measurement Templates 115

8.6 A.6 VN-steel Pearlite Volume Fraction by Thresholding 116

8.7 A.7 Prior Austenite Grain Size Measurement Templates 117

8.8 A.8 SEM-EDS Spectra Precipitate Analysis after Heat Treatment 121

LIST OF FIGURES

Figure 1.1: Evolution of microstructure and mechanical properties of microalloyed plate steels through process optimisation and alloy design [11]. 2

Figure 1.2: Typical applications of microalloyed steels in some of the leading industries [3], [16]–[18]. 2

Figure 2.1: (a) Thin foil micrograph, 120 000X, of Fe – 0.6%Mn – 0.41%Si – 0.08%Nb – 0.10%C steel austenitised at 1250 °C, air-cooled. The NbC precipitates are fine enough to pin a dislocation [46]; **(b)** Effect of niobium carbides on the yield strength for various sizes of niobium carbide particles [35]. *NB: 10 Angstrom = 1 nm.* 8

Figure 2.2: Deduced values of precipitation strengthening for isothermally transformed V-steels (650/500s). **(a)** as a function of N-content, **(b)** as function of C-content [15], [52]. 9

Figure 2.3: Effect of cooling rate on the yield strength due to the effective combination of precipitation strengthening and grain refinement in a 0.15%V steel [35]. 10

Figure 2.4: Influence of Ti and S on each other with a constant carbon level for an IF-steel (0.005%C) and a microalloyed steel (0.05%C) [58]. 12

Figure 2.5: Solubilities of microalloy precipitate phases: **(a)** carbides and nitrides, **(b)** carbides, nitrides, sulphides and carbosulphides [15], [56]. 13

Figure 2.6: HSLA steels' modelled precipitation kinetics of NbC superimposed with experimental data [70]; **(a)** in austenite, at 900 °C, experimental data from [74]; **(b)** and **(c)** in ferrite, at 600 °C, 700 °C and 800 °C experimental data from [75]. 16

Figure 2.7: Development of ferrite-pearlite microstructural banding from microsegregation in low-carbon steel; **(a)** ingot structure, **(b)** hot-rolled plate [28]. 17

Figure 2.8: Schematic diagram of the solidification of a binary alloy with equilibrium at the solid-liquid interface: **(a)** phase diagram; **(b)** composition profile across the solid-liquid interface [86]. 19

Figure 2.9: Temperature distribution profiles of the actual liquid temperature and its equilibrium liquidus temperature during solidification of a liquid alloy; **(a)** showing necessary conditions for constitutional undercooling, **(b)** conditions that eliminate constitutional undercooling [89]. 20

Figure 2.10: Microstructures showing banding mechanism as enhanced by carbide forming elements in hypoeutectoid steel; **(a)** longitudinal section of the as forged sword blade, **(b)** after heat treatment [93]. 21

Figure 2.11: Variation of Mn & Si contents across representative ferrite-pearlite bands in the central, longitudinal section of a banded as-rolled 20mm plate steel (0.25C-0.34Si-1.75Mn-0.24Cr, wt%) [91]. Note: The influence of Mn segregation has predominated that of Si which was supposed to enhance ferrite nucleation in Si-rich areas. 22

Figure 2.12: (a) Schematic *scale* models of the early stages of the ferrite nucleation. Shaded bands are assumed to be the Mn-rich regions that eventually transform to austenite. Thus, ferrite nucleation

occurs in Mn-lean regions **(*arrowed C*)** [95]. **(b)** Final microstructure showing pearlite bands labelled P and ferrite "slabs" labelled C, E-H [76]. 23
Figure 2.13: Showing a decrease in ferrite-pearlite banding severity from the most to the least severe (*a–d*) as influenced by the PAGS in 0.25C-0.35Si-1.75Mn-0.24Cr *(wt%)*. Samples were austenitised at different temperatures for 1hr then cooled at a rate of 5 °C/min; 100x; Picral. **(a)** 825 °C, **(b)** 875 °C, **(c)** 925 °C and **(d)** 1050 °C [91], *p.g.116*. 24
Figure 2.14: The relationship between cooling rate and calculated mean displacement of the γ/α phase boundary during austenite decomposition for 3 study-steels [80]. Steel 1 (C-Mn steel), steel 2 (C-NbTiV steel), steel 3 (C-NbTi steel). 27
Figure 2.15: Continuous cooling experiments microstructures showing the influence of cooling rate (CR) on ferrite-pearlite microstructural banding in a hot-rolled Fe-0.17C-1.47Mn-1.48Si (*mass %*) steel [96]. 28
Figure 2.16: Summarised tensile and impact test results for; **(a)** clean steel, longitudinal specimens, and **(b)** dirty steel, longitudinal specimens [28], *p.g. 422.* 30
Figure 2.17: (i) Schematic representation of the normalising schedule, *a*-heating, *b*-soaking, *c*-air cooling, *d*-air or furnace cooling. **(ii)** Normalising temperature ranges for plain carbon steels depending on carbon content. Note: The temperature range above the A_{cm} line is applied for secondary carbide dissolution, as cited in [111]. 33
Figure 2.18: The influence of austenitising temperature on the rate of austenite formation from pearlite in eutectoid steel, as cited in [83]. 34
Figure 2.19: Hypoeutectoid portion of the Fe-Fe_3C phase diagram depicting the phases present during different intercritical heat treatments of the hypothetical alloy, where % γ and $\%C_\gamma$ depend on the intercritical temperature [121]. 36
Figure 2.20: Kinetics of isothermal austenitisation at different temperatures for a 0.12C–1.5Mn (wt%) steel [124]. 38
Figure 2.21: Micrographs of Nb-microalloyed steel annealed at 810 °C for 16 min. **(a)** Optical microstructure, region A of retained ferrite, B of epitaxial ferrite and C of the eutectoid structure containing degenerate pearlite. Boiling alkaline chromate etch. **(b)** TEM microstructure depicting the precipitate free zone (evidential presence of epitaxial ferrite) [45]. 38
Figure 2.22: Tensile and impact properties of the HSLA steel after ICHT and Q&T [121]. 40
Figure 3.1: A schematic of the assessment parameters for the degree of banding, ASTM E1268-01 [25]. 46
Figure 3.2: Simulated air-cooling rates for the as-hot rolled 16 mm thick by 2500 mm wide VN-steel plate and 30 mm thick by 2500 mm wide NbTiV-steel plate: **(i)** Temperature vs cooling time. Applied heat treatment cycles include, **(ii)** Normalising heat treatment (NHT); **(iii)** Double

austenitisation heat treatment (DAHT), **(iv)** Intercritical annealing heat treatment (IAHT). ***NB:*** *Heating duration to test temperature, 30 minutes*..... 48
Figure 3.3: Schematic thermal profiles for the intercritical annealing temperature optimisation of the study steel microstrutcures. ***NbTiV-steel (30 mm plate)***: **(i)** IAHT-810, 775 & 740 °C, and **(ii)** DAHT-810, 775, & 740 °C. ***VN-steel (16 mm plate)***: **(iii)** IAHT-810, 775 & 740 °C, and **(iv)** DAHT-810, 775, & 740 °C. 49
Figure 3.4: (i) Tensile sample arrangement in the Gleeble chamber, **(ii)** Tensile sample during the normalising heat treatment, **(iii)** CVN specimen arrangement, **(iv)** The Gleeble™ 1500 thermo-mechanical simulator..... 51
Figure 3.5: Schematic representation of the standard size CVN specimen machining–orientation with respect to the hot-rolled plate. 52
Figure 3.6: An illustration of the arrangement for the test temperature (at –30 °C) conditioning of the CVN specimens. On the right, the black arrow showing liquid nitrogen boiling off of the surface of the ethanol. 53
Figure 3.7: NbTiV-steel Thermo-Calc™ results showing: **(i)** volume fractions of austenite & ferrite vs temperature; Ae_3 temperature. **(ii)** precipitate volume fractions and their dissolution temperatures. 55
Figure 3.8: VN-steel Thermo-CalcTM results showing: **(i)** volume fractions of austenite and ferrite vs temperature; Ae3 temperature. **(ii)** precipitate volume fractions and their dissolution temperatures. 55
Figure 4.1: Dilatation curves for **(i)** VN-steel (16 mm) and **(ii)** NbTiV-steel (30 mm) indicating the transformation temperatures. Heating and air-cooling rates in *Figure 3.2(i)* were used..... 58
Figure 4.2: Dilatometric analysis of the influence of intercritical annealing temperature on the relative austenite volume fraction (V_γ). Full austenitisation dilatation curve (solid) and intercritical austenitisation (dotted curves). **(i)** NbTiV-steel, the dotted red lines indicate the system at 775 °C, 800 °C and 825 °C. **(ii)** VN-steel, the dotted red line indicates the system at 775 °C. A heating rate of 31 °C/min. 59
Figure 4.3: Showing optical micrographs for the 30 mm plate NbTiV-steel (left) starting with **(a)** Near-surface (NS), **(b)** Quarter-thickness (QT), **(c)** Mid-thickness (MT); and 16 mm plate VN-steel (right) starting with **(d)** NS, **(e)** QT and **(f)** MT. Etched with 2% Nital. Scale bar, 100 µm (x100). 61
Figure 4.4: A plot of the average ferrite grain size vs depth from the surface to the centre of the 30 mm thick NbTiV and 16 mm thick VN-steel plates. 62
Figure 4.5: Optical images of microstructures that were austenitised for 2hrs, water-quenched followed by tempering at 496 °C for 33hrs. Only *(c)* was not tempered. NbTiV-steel (left), **(a)** austenitised at 1005 °C, **(b)** at 1050 °C; and VN-steel (right), **(c)** austenitised at 1005 °C

(untempered), **(d)** at 1050 °C. Etched with Marshall's reagent + 2 drops of HF. The scale bar is 20 µm. 64
Figure 4.6: A plot showing the influence of austenitisation temperature on the average prior austenite grain size (PAGS) of the NbTiV and VN-steels. 65
Figure 4.7: Showing optical images of microstructures that were austenitised at 1050 °C for 2hrs, water-quenched, then tempered at 496 °C for 33hrs. **NbTiV-steel** (left), **(a)** near-surface **(b)** mid-thickness; and **VN-steel** (right), **(c)** near-surface, **(d)** mid-thickness. Red circle showing banding-retention region at the mid-thickness in both samples. Etchant: Marshall's reagent + 2 drops of HF. The scale bar is, 50 µm. 66
Figure 4.8: Through-thickness average PAGS vs austenitising temperature for, **(i)** NbTiV and **(ii)** VN. 67
Figure 4.9: Optical micrographs of the NbTiV (left) and VN-steel (right) samples after the DAHT at intercritical temperatures of 740, 775 and 810 °C in the 2nd cycle as indicated in the inserts. Illustrating how the cycles had little to almost no impact on the ferrite-pearlite banding except at 775 °C. The scale bar is 50 µm. 2% Nital etch. 68
Figure 4.10: Optical micrographs of the NbTiV (left) and VN-steel (right) samples after the IAHT at 740, 775, and 810 °C as indicated in the inserts. Illustrating how the cycles had no major impact on the ferrite-pearlite banding, except at 775 °C for both steel samples and 810 °C for NbTiV. The scale bar is 50 µm. 2% Nital. 69
Figure 4.11: Optical micrographs of the NbTiV-steel samples showing respective ferrite grain sizes, volume fractions and macro-Vickers hardnesses. **(a)** NHT; **(b)** DAHT; **(c)** DAHT at higher magnification, depicting fine pearlite colonies nucleating at prior austenite grain corners and boundaries (black arrows). Also, note the refined pearlite that nucleated in the carbon-rich regions (white arrows); **(d)** IAHT. All scale bars are at 50 µm, except that in ***(c)*** which is 20 µm. 2% Nital etch. 71
Figure 4.12: Optical micrographs of the VN-steel samples showing respective ferrite grain sizes, volume fractions and macro-Vickers hardnesses. **(a)** NHT (austenitised at 930 °C); **(b)** DAHT (annealed at 930 & 775 °C); **(c)** IAHT (annealed at 775 °C). All scale bars at 50 µm. 2% Nital etch. 72
Figure 4.13: Ferrite grain size distribution of NbTiV (top, *a–c*) and VN-steel (bottom, *d–f*) heat treated microstructures. ***a), b), d)*** and ***e)*** Showing a normal distribution after the NHT and DAHT. ***c)*** and ***f)*** showing a bimodal distribution after the INHT. 73
Figure 4.14: SEM secondary images of the NbTiV (left) and VN-steel (right) samples after the DAHT and IAHT as indicated in the inserts. Illustrating the fine pearlite colonies (light phase) that nucleated at ferrite (dark matrix) grain boundaries and grain corners. The scale bar is 5 µm. 2% Nital etch. 75

Figure 4.15: SEM secondary images showing precipitate free (PF) epitaxial ferrite grains and degenerate pearlite in both steel samples after the IAHT. **(a)** NbTiV-steel, **(b)** VN-steel. 2% Nital etch. 76
Figure 4.16: Comparison of the NHT, DAHT and IAHT tensile properties of the study-steels. **(i)**&**(iii)** Engineering stress-strain curves for the NbTiV & VN-steels respectively; **(ii)**&**(iv)** tensile property comparison with respective heat treatment in NbTiV & VN-steels, respectively. 77
Figure 4.17: Determining the strain hardening exponents of the heat-treated study steels through the Hollomon power-law. (i) & (iii) True stress-strain plots. (ii) & (iv) True stress-strain log-log plots depicting the n-values for the study-steels. 78
Figure 4.18: Impact of the applied heat treatments on the hardness of NbTiV and VN-steel. 79
Figure 4.19: Charpy V-notch impact graphs for the NbTiV and VN-steels showing the effect of the heat treatments on the impact toughness properties. 80
Figure 4.20: Representation of yield strength-impact toughness combination of the heat-treated NbTiV and VN-steels. The closed symbols depict the impact energy at 20 °C, and open symbols absorbed impact energy at –40 °C. The red indicators show minimum specification requirement limits as per [157]–[159]. The highlighted green zone shows the region of the best strength-toughness combination. 81
Figure 4.21: SEM fractographs for the NbTiV (left) and VN (right) after the **NHT**. Test temperatures are also indicated in the inserts. White arrows show cleavage cracks (at –85 & –90 °C). At a test temperature of –40 °C, ductile modes are characterised by dimples and tearing (red circled area) in both samples. 82
Figure 4.22: SEM fractographs for the NbTiV (left) and VN (right) after the **DAHT**. Test temperatures also indicated in the inserts. Plane and smooth faceted fracture surfaces at a test temperature of –80 °C. Test temperature of –40 °C showing ductile modes characterised by dimples in both samples. 83
Figure 4.23: SEM fractographs for the NbTiV (left) and VN (right) after the **IAHT**. Test temperatures are also indicated in the inserts. Smooth-faceted fracture surfaces. White arrows showing cleavage cracks at a test temperature of –80 °C. A mixed-mode of fracture at a test temperature of –40 °C. 84
Figure 8.1: Templates for the simulated cooling profiles for the 30 mm thick by 2500 mm wide NbTiV-steel plate and the 16 mm thick by 2500 mm wide VN-steel plate. Cooling profiles generated from [143]. 112
Figure 8.2: NbTiV-steel Thermo-Calc predictions for the ferrite and austenite volume fractions at intercritical temperatures of 740, 775 and 810 °C respectively. 113
Figure 8.3: VN-steel Thermo-Calc predictions for the ferrite and austenite volume fractions at intercritical temperatures of 740, 775 and 810 °C respectively. 114

Figure 8.4: Showing the NbTiV and VN calculation templates that were used in the determination of ferrite grain sizes and volume fractions. 115
Figure 8.5: An illustration of the volume fraction estimation through thresholding procedure in ImageJ Software©. VN-steel microstructure, Mid-thickness. 2% Nital etch. 116
Figure 8.6: NbTiV-steel prior austenite grain size measurement excel templates. Measurements were taken at near-surface, quarter-thickness and mid-thickness. Austenitising temperature has also been included in the templates. 118
Figure 8.7: VN-steel prior austenite grain size measurement excel templates. Measurements were taken at near-surface, quarter-thickness and mid-thickness. Austenitising temperature has also been included in the templates. 120
Figure 8.8: SEM-EDS spectra analysis of precipitates in the ferrite matrix for the heat treated NbTiV and VN-steels. **(a)** NbTiV, IAHT; **(b)** NbTiV, DAHT; **(c)** VN, IAHT; **(d)** VN, DAHT. 124

LIST OF TABLES

Table 2-1: Alloying elements frequently used in microalloyed steels, with their roles [11]..... 7
Table 2-2: Volume fraction of stringers (Vs) in the four Ti-steels [58]. 12
Table 2-3: Influence of PAGS on the pearlite band spacing in the transformed microstructure [80]. 25
Table 2-4: Typical Yield Strength/Ultimate Tensile Strength ratios for cast steels subjected to various types of heat treatments [121]. 41
Table 3-1: Chemical composition of the steels (mass %). 44
Table 3-2: Heat treatment simulation schedules 48
Table 3-3: T_{NR} predictions for the study-steels based on models from the literature [61]–[63]..... 56
Table 4-1: A summary of the critical transformation temperatures for the VN and NbTiV steels. 58
Table 4-2: A summary on the degree of microstructural banding measurements in the study-steels. See Appendix A.1 for definitions of parameters in the table 63
Table 4-3: A summary of the influence of respective heat treatments on the microstructural evolution of the study-steels..... 74
Table 4-4: A summary of the mechanical properties of the heat-treated steel specimens 80
Table 5-1: Percentage decrease in the impact-absorbed energy between the upper shelf energy (USE) and at a test temperature of –40 °C in the heat treated NbTiV and VN-steel samples..... 92

LIST OF ABBREVIATIONS

HSLA	High Strength Low Alloy
TMP	Thermomechanical Processing
T_{NR}	Nil-recrystallisation temperature
IF	Interstitial-Free
CALPHAD	Calculation of Phase Diagrams
EPMA	Electron Probe Micro-Analyser
PAGs	Prior Austenite Grains
PAGS	Prior Austenite Grain Size
PAGBs	Prior Austenite Grain Boundaries
CGBNs	Contiguous Grain Boundary Networks
DIC	Digital Image Correlation
DBTT	Ductile-to-Brittle Transition Temperature
CVN	Charpy V-Notch
USE	Upper Shelf Energy
HIC	Hydrogen-Induced Cracking
JMAK	Johnson-Mehl-Avrami-Kolmogorov
CPPT	Cyclic Partial Phase Transformation
ICHT	Intercritical Heat Treatment
UTS	Ultimate Tensile Strength
OM	Optical Microscopy
FEG-SEM	Field Emission Gun Scanning Electron Microscope
ASTM	American Society for Testing Materials
NHT	Normalising Heat Treatment
DAHT	Double Austenitisation Heat Treatment
IAHT	Intercritical Annealing Heat Treatment
GNDs	Geometrically Necessary Dislocations

CHAPTER 1 INTRODUCTION

1.1 Background and significance

The growing need to efficiently utilise renewable energy and power generation while at the same time conserving and maintaining a greener environment,t has become the major focus in the renewable energy industry. Particularly, wind as a renewable resource has received attention and is harnessed for electric power generation by wind turbines in wind towers. Since its origins in the late 1970s, the modern wind power industry has been growing at a fast rate with an attempt to globalise the wind tower market [1]. In 2017 and 2016, the offshore wind segment amounted to total global cumulative installations of 539 GW, and 487 GW respectively, which exhibited an 11% increase on the annual market [2]. This signifies a global increase in the demand for wind towers.

The growing demand for wind towers has led to increased attention in the field of metallurgical engineering with regards to the design of tubular structural supports for the wind towers for high: strength, fatigue resistance, fracture and impact toughness [3], [4]. To achieve such properties, a class of steels known as microalloyed or high strength low alloy (HSLA) steels are employed in the material design of the tubular structures for the wind towers [5], [6]. This class of steels contain low levels of carbon, and very minute amounts (< 0.1%) of microalloying elements such as; niobium, vanadium, titanium and rare earth metals. These elements are utilised either as single additions or in combinations that eventually significantly improve the steels' mechanical properties through solid solution strengthening, precipitation strengthening, and strengthening by grain refinement [7], [8]. A significant contribution comes from the combination of precipitation and grain refinement strengthening, see Figure 1.1**.** These microalloying elements are strong carbide and nitride formers; and during hot rolling they, therefore, lead to nucleation of fine (30–800 nm) precipitates that retard austenite recrystallisation, consequently inhibiting austenite grain growth by pinning the austenite grain and subgrain boundaries through the Zener pinning effect [9]–[12]**.** The result of this is ferrite grain refinement, which in addition to strengthening also improves the toughness of the steel as shown in Figure 1.1.

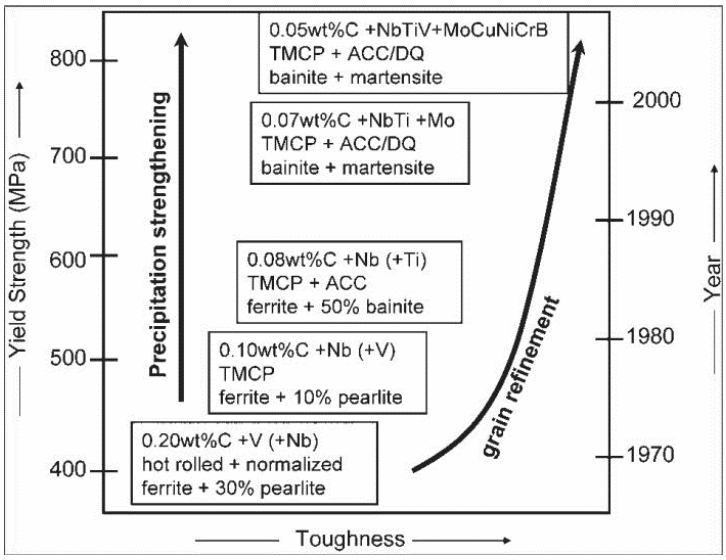


Figure 1.1: Evolution of microstructure and mechanical properties of microalloyed plate steels through process optimisation and alloy design [11].

Microalloyed steels' yield strength properties have been reported to be in the range of 350-800 MPa, as opposed to the lower values of mild steels that are typically in the range of 120-200 MPa [9], [11]. In addition to the aforementioned properties, the low levels of carbon and the other alloying elements make these metals easily weldable [3]. Not only are microalloyed steels used in the wind power industry, but also the pipeline, automotive, construction industries and many more [3], [13]–[15], Figure 1.2. These applications have increased the prominence of the microalloyed steels and the need for their study through research.



Figure 1.2: Typical applications of microalloyed steels in some of the leading industries [3], [16]–[18].

A lot of research is being done to exploit the strength qualities of Nb-Ti-V microalloyed steels while at the same time maintaining preferred levels of toughness by appropriate heat treatments. For instance, Gao *et al*., [19] conducted a study that aimed at revealing the effects of normalising and tempering temperatures on the strength and toughness of low carbon microalloyed cast steels. It was reported that niobium (Nb) containing microalloyed steels have better mechanical properties than Nb-free alloys when normalised at 900 °C and tempered at 550 °C for 2 hours. It was also reported that for a certain amount of Nb (0.044 wt. %-Nb), the yield and tensile strengths (YS & UTS) increased from 290 MPa and 485 MPa to 350 MPa and 520 MPa respectively, as compared to Nb-free steel. The room temperature impact toughness improved by 25.6% while the ductility remained almost the same. In other studies, Najafi *et al*. found similar effects of Nb addition and heat treatment on the YS and UTS [20], [21], however, the results on toughness in these two studies were different from those reported by Gao *et al*., [19]. The examination of the fracture surfaces of the microalloyed steels for the two previously mentioned studies showed a complete failure by trans-granular cleavage; proving that the increase in strength was at the expense of toughness. It is, therefore, necessary for the continuation of research currently being done focused on room temperature impact toughness.

Usually, hot-rolled HSLA steels are designed and produced in such a state that exhibit prominent mechanical properties. Nonetheless, for certain applications such as in large pressure vessels and wind tower base equipment [22][23], thicker plates are required. In such applications, normalised HSLA steel plates with a stable microstructure that gives consistent mechanical properties (mainly impact toughness) are demanded. A well-known phenomenon called microstructural banding usually occurs in hot-rolled HSLA steels. This usually originates in the cast slab during dendritic solidification and/or solid-state phase transformations as may be governed by microsegregation, subsequently resulting in the development of a banded microstructure [24]–[26]. Some factors that also influence microstructural banding include; the hot-rolling finishing temperature, the degree of hot or cold-work reduction, or split transformations due to limited hardenability or inadequate cooling rate [25]. Microstructural banding has negative effects on the ductility and the impact toughness of HSLA steels. Therefore, this work focused on studying the microstructural behaviour after normalising heat treatments to mitigate initial banding and microstructural memory effects, thereby improving the final mechanical properties. The study was done on Nb-Ti-V and VN microalloyed plate steel grades, with the VN-steel serving as the benchmark.

1.2 Problem statement

The requirement for a combination of high yield strength (≥355 MPa) and impact toughness at low temperatures typically CVN 40 to 60 J at – 20 °C, is becoming more stringent by users of normalised Nb-Ti-V microalloyed plate steel grades. The final mechanical properties (after normalising heat treatment) are largely influenced by the incoming as hot-rolled microstructures. In most cases, a non-uniform, coarse and banded as hot-rolled microstructure persists even after normalising heat treatment. Such a microstructure has direct, undesirable effects on the final mechanical properties of the product, especially the impact toughness [27], [28].

To alleviate this problem, post-hot rolling is applied to the hot-rolled steels. Normalising heat treatment serves to homogenise and bring uniformity throughout the microstructure eventually mitigating the microstructural banding. Therefore, the primary aim of this study was to mitigate the microstructural banding through optimisation of a series of normalising heat treatments, while also achieving low-temperature impact toughness, and not compromising too much on the yield strength.

1.3 Scope of study

This study was limited to microalloyed 0.12C-Nb-Ti-V (30 mm) and 0.12-VN (16 mm) plate steels in the as hot-rolled condition. The study focused on the influence of three heat treatment cycles on the microstructural evolution (aiming at microstructural banding mitigation), and the implications on the mechanical properties viz; normalising heat treatment (NHT), double austenitisation heat treatment (DAHT) that involved full austenitisation followed by intercritical-austenitisation, and intercritical annealing heat treatment (IAHT). Typical industrial normalising heat treatment parameters were employed in the process simulations of this study.

1.4 Study objectives

1. To characterise the incoming as hot-rolled banded microstructure.
2. To establish what type of heat treatment is effective in reducing microstructural banding.
3. To determine the impact of banding on mechanical properties.
4. To determine the influence of each heat treatment route on the mechanical properties.

CHAPTER 2 LITERATURE REVIEW

2.1 Introduction

This section gives a review of different literature concerning microalloyed steels, and other studies that focused on improving the microstructure of Nb-Ti-V HSLA steels for a combination of improved strength and impact toughness. Therefore, this section depicts how other researchers approached their studies; considering their experimentation, findings, conclusions and recommendations made. In addition to that, this section will try to evaluate some knowledge gaps within other research studies and hence justify the significance of the current study. Finally, this section also contains a review of some of the fundamental phase transformations as influenced by the heat treatments that have been employed in the current study.

2.2 Historical background of HSLA steels

As mentioned in section 1.1, Nb-Ti-V HSLA steels contain Nb, V, Ti as the main microalloying elements in very small quantities (<0.1%) to improve the strength of hot-rolled steels without raising the carbon (C) and manganese (Mn) contents. Originally (mid-20th century) these steels were designed merely for high strength in the as-hot rolled condition [9]. The aim was to achieve improved strength/weight ratios in transportation equipment since they permit reduced component weight which consequently reduces fuel consumption [29]. As applications for microalloyed steels increased, the need to improve and exploit some of the properties of these steels also grew larger; this needed an in-depth understanding of the processing routes and the development of microstructure [9], [30]. Therefore, this led to the use of processing methods such as; thermomechanical processing (TMP), which directly influences the microstructure to achieve the desired properties in these steels. Through research, many efforts have been made that aim at optimizing these TMP techniques to achieve combined superior properties of toughness and strength [14], [31]–[33].

For instance, concerning the original need of solely attaining high strength in the steels, cleavage failure in ships and structural components posed a very crucial knowledge gap that needed filling. This led to the realisation that impact toughness is very crucial [34]. Hence, process optimisation has proven to be one of the most effective ways of producing microalloyed steels with a good combination of strength and impact toughness.

2.3 Influence of microalloying elements

Microalloyed steels are designed to provide superior impact toughness and mechanical properties, and also a higher corrosion resistance than conventional carbon steels [30], [35]. Furthermore, these steels are designed to contribute suitable weldability and formability as a result of the low amounts of carbon, which gets to as low as 0.06% for some HSLA steels. All of this is achieved by the effects contributed by small additions in different combinations of alloying elements such as nickel, copper, molybdenum, chromium, nitrogen, niobium, vanadium, titanium, and zirconium. Much emphasis in this section will be placed on microalloyed steels with additions of niobium (Nb), vanadium (V) and titanium (Ti).

The various roles that microalloying elements play are evident in the following: grain refinement (improving strength and toughness), precipitation strengthening (formation of carbide and carbonitride precipitates) and solid solution strengthening. Nb, V and Ti have a strong affinity for carbon (C) and more especially for nitrogen (N), thus they precipitate as carbide, nitride and carbonitride particles [36]–[40]. Precipitation of these particles normally occurs during reheating, austenitisation, hot rolling and cooling (on the run-out table, coiling, after heat treatment). In the late 1930s to mid-1940s, Nb and V were first used as strengtheners in hot rolled carbon-manganese (C-Mn), and normalised steels. However, the impact toughness of these steels was poor due to the precipitation strengthening by V(C, N) and Nb(C, N) [30], [40]. Later it was then discovered and reported that through austenite grain refinement during hot rolling and an increase in the Mn content, the impact toughness properties of these steels could be improved [40]. Ti with its strong affinity for N forms TiN, a highly stable precipitate, even at very high temperatures (1300 °C) [7], [41], [42]. The size of the TiN precipitates can be controlled by managing the amounts of Ti additions to the steel [38], which means optimal amounts of Ti need to be added to produce fine TiN particles. Table 2-1 gives a summary of the roles that microalloying elements play in microalloyed steels.

Table 2-1: Alloying elements frequently used in microalloyed steels, with their roles [11].

Element	Wt-% in steel	Influence
C	<0.25	Strengthener
Mn	0.5 – 2.0	Delays austenite decomposition during accelerated cooling Decreases the ductile-to-brittle transition temperature Strong sulphide former
Al	>0.02	Deoxidiser Limits grain growth (AlN)
Nb	0.02 – 0.06	Very strong ferrite strengthener as [Nb(C, N)] Grain size control Delays austenite to ferrite transformation
Ti	0 – 0.06	Austenite grain size control by TiN Strong ferrite strengthener
V	0 – 0.1	Strong ferrite strengthener by V(C,N)
Zr	0.002 – 0.05	Austenite grain size control [Zr(C,N)] Strong sulphide former
N	<0.012	Forms nitrides and carbonitrides
Mo	0 – 0.3	Promotes bainite formation Ferrite strengthener
Ni	0 – 0.5	Increases fracture toughness
Cr	0 – 1.25	With Cu, increases atmospheric corrosion resistance

2.3.1 Niobium

The effect of Nb in microalloyed steels has been well documented in various studies. Nb produces high yield strength levels in microalloyed steels by precipitation hardening through the formation of Nb-carbides, nitrides and Nb-intermetallic precipitates. These Nb-carbides and nitrides are very stable compounds such that effective solution treatment temperatures of up to 1250 °C are necessary. Thus, the primary role of Nb additions in HSLA steels is to precipitate the fine strain-induced NbC and Nb(C, N) during the austenite-ferrite transformation upon cooling, and this leads to the strengthening of the ferrite matrix [43]. The degree of strength level is dependent on the fineness and volume fraction of the precipitates [35]. It has been reported that very fine Nb(C, N) precipitates provide effective pinning of dislocations [19], [44], [45], Figure 2.1*(a)*. Figure 2.1*(b)* depicts how the different sizes of NbC carbide particles impact the yield strength, with the smallest ones being the most effective.

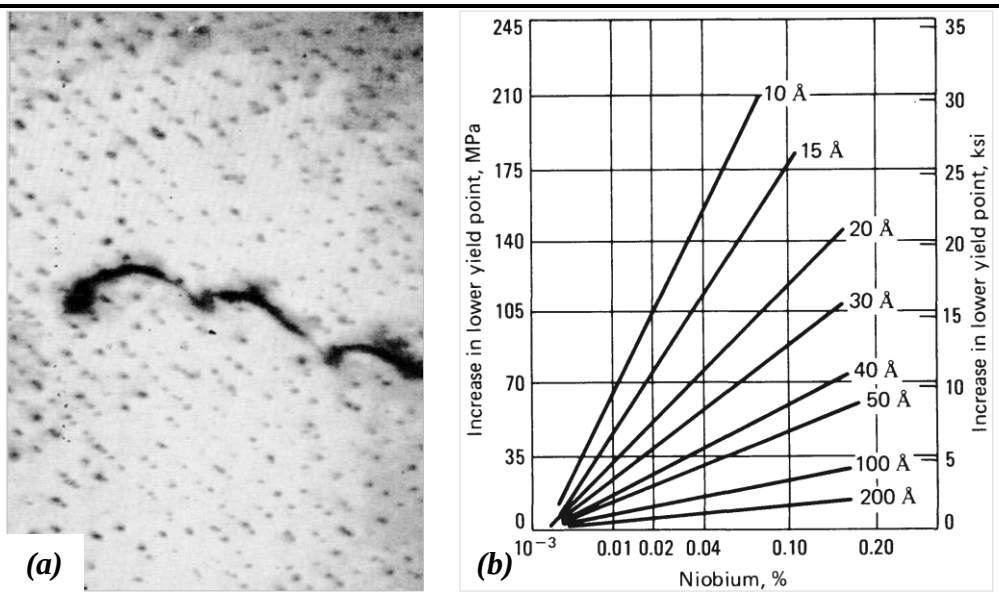


Figure 2.1: (a) Thin foil micrograph, 120 000X, of Fe – 0.6%Mn – 0.41%Si – 0.08%Nb – 0.10%C steel austenitised at 1250 °C, air-cooled. The NbC precipitates are fine enough to pin a dislocation [46]; **(b)** Effect of niobium carbides on the yield strength for various sizes of niobium carbide particles [35]. *NB: 10 Angstrom = 1 nm*.

Geib *et al*. reported that the dislocation pinning effectiveness by the Nb(C, N) particles is greatest for particle sizes of 20 nm or smaller [45]. The NbC/dislocation interactions impede dislocations from moving freely and therefore contributing to the strength of microalloyed steels containing Nb. Also, these precipitates retard austenite grain growth during austenitisation and delay the austenite-ferrite transformation, leading to grain refinement [47], [48].

It has also been argued that the strengthening contribution by Nb in solid solution to the yield strength is in the range of 35 to 40 MPa per 0.01% addition [35]. However, it should be noted that too high strength levels come at the expense of toughness, hence an optimum amount is required. Additionally, Nb in solution plays a vital role in the refinement of ferrite grains by segregating to the austenite/ferrite boundaries thereby decreasing the growth kinetics of ferrite through solute drag [49], [50]. Nevertheless, a stronger influence is brought about through pinning by Nb(C, N) precipitates of austenite grain boundaries, than Nb in solution through solute drag [39]. It is this effect of Nb(C,N) precipitates in the pinning of austenite grain boundaries, that is largely utilised in retarding dynamic recrystallization of austenite during thermally controlled rolling processes.

This is made possible because of the great stability (at high temperatures) of NbN and Nb(C, N) particles that make the precipitates less easy to dissolve in austenite during high-temperature solution treatment and the early stages of hot rolling. Consequently, this also means they precipitate earlier upon cooling. Therefore, it is the combined effect of precipitation, solid solution and ferrite grain refinement strengthening that makes Nb an effective strengthening microalloying element.

2.3.2 Vanadium

Like Nb, vanadium (V) also improves the yield strength through precipitation and grain refinement strengthening. The strengthening contribution comes from the fact that very fine and coherent V(C,N) precipitates nucleate on dislocations thereby pinning them and preventing them from movement. However, V is less effective in these aspects when directly compared to Nb [35]. This was shown in another study on microalloyed steels where higher peak and mean flow strength levels were obtained for Nb-Ti steel in comparison to a VN-steel [51]. Furthermore, strengthening from V is also dependent on the carbon and nitrogen contents. The significance of the carbon and nitrogen contents has been recognised in hot rolled microalloyed steels, for instance, in structural steels that typically contain up to 0.1%V, less than 0.1%C and up to about 0.02%N. With regards to the yield strength contribution through precipitation hardening alone, the N is marginally more effective than the C with an increase in yield strength of about 6 MPa per 0.001%N addition compared to about 5.5 MPa per 0.01%C addition. This has been shown in Figure 2.2 as reported by Lagneborg *et al*. [15], [52]. An increase in N content leads to a higher nucleation rate of VN particles leading to a higher volume fraction of fine VN precipitates, and a smaller interparticle spacing than if only C were present and precipitating as VC particles.

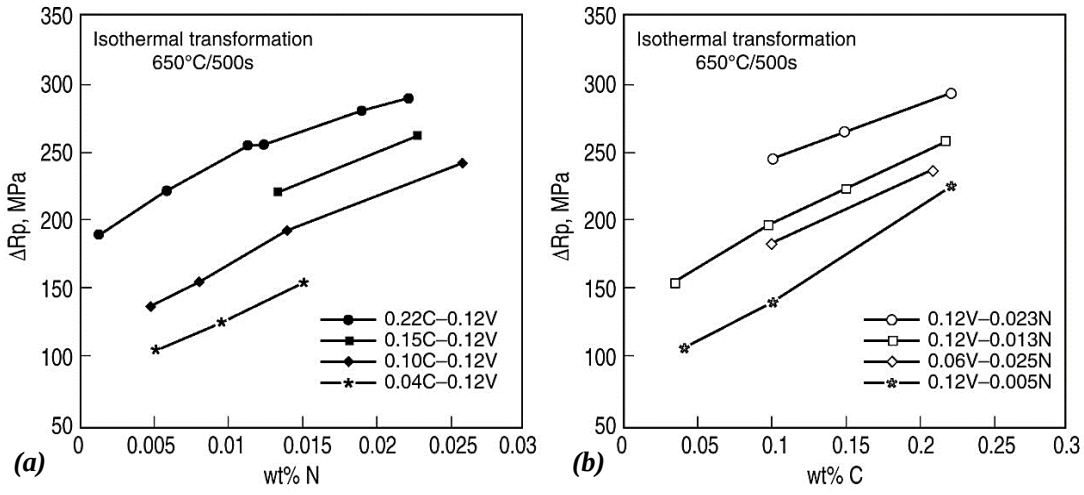


Figure 2.2: Deduced values of precipitation strengthening for isothermally transformed V-steels (650/500s). **(a)** as a function of N-content, **(b)** as function of C-content [15], [52].

Moreover, the high nitride stability results in the initial precipitation of the VN particles only until all the free N has been depleted and is then followed by the precipitation of the VC particles. Hence, the argument is made that the V(C, N) precipitates are comprised of an inner core of VN which is enfolded by C-rich V(C, N) [15], [53]. Therefore, the N content of the V-bearing microalloyed steels is very crucial in attaining the right ferrite grain size with suitable precipitation strengthening by the fine V(C, N).

In terms of grain refinement, VN and V(C, N) form in the austenite phase thereby pinning the austenite grain boundaries during hot rolling. However, this happens at much lower temperatures of the austenite phase region than is the case with Nb(C, N); with most of the VC and V(C, N) precipitating in ferrite upon cooling after hot rolling [15], [35].

In comparison to Nb, V is advantageous when it comes to its greater solubility in austenite such that the VC and V(C, N) particles readily dissolve during solution treatment and early stages of hot rolling than for the corresponding NbC and Nb(C, N) precipitates. This means that during hot rolling, the V precipitates remain dissolved and in solution at all of the usual rolling temperatures, making their precipitation more reliant on the cooling rate [9], [15], [35], [54]. The influence of the cooling rate was also reported by Davies [35] as shown in Figure 2.3.

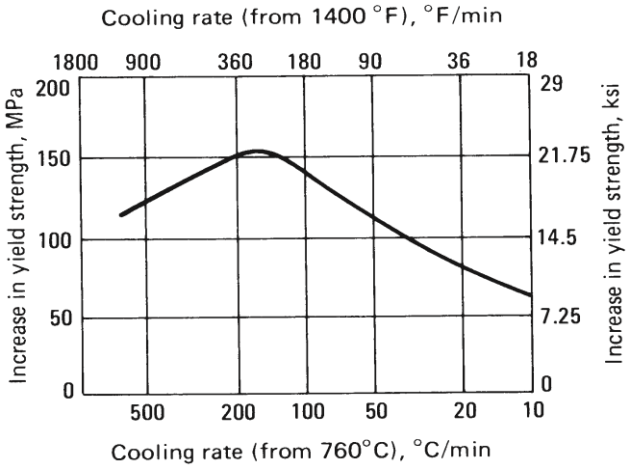


Figure 2.3: Effect of cooling rate on the yield strength due to the effective combination of precipitation strengthening and grain refinement in a 0.15%V steel [35].

The optimum level of precipitation hardening comes about at a cooling rate of approximately 170 °C/min. At cooling rates below 170 °C/min, the VC and V(CN) precipitates coarsen and are less effective for producing the required yield strength. Very high cooling rates produce a low precipitate volume fraction due to the limited amount of time for precipitation of the particles, hence reducing the yield strength of the steel as shown in Figure 2.3 for cooling rates beyond 170 °C/min.

2.3.3 Titanium

In microalloyed steels, Ti normally precipitates into a highly stable nitride called TiN that is essentially insoluble in austenite and eventually prevents austenite grain growth during solution treatment. TiN precipitates are known to precipitate even during solidification [54]; this signifies how stable the TiN precipitates are. Ti is also a strong deoxidizer and very effective in removing free N from the steel (lowering N levels in solution) to achieve good impact toughness and ductility [55]. However, it is important to control the Ti:N ratio (<3.42) to avoid coarse TiC particles, which are detrimental to the toughness properties of the steel [38].

TiN precipitates are known to be very stable even at temperatures as high as 1300 °C. These temperatures would invariably lead to abnormal austenite grain growth if attempting to dissolve the particles during solution treatment. Therefore, additions of Ti in microalloying steels while maintaining the Ti/N ratio in the optimum ranges (<3.42) results in fine TiN precipitates that inhibit austenite grain growth during processing as well as welding [15], [38], [56]. For very high Ti/N ratios, both TiN and TiC precipitates emerge, and TiC is not as effective austenite grain growth inhibitor as TiN particles. This aspect was shown by Cuddy and Raley [57], where they studied microalloyed steels with varying amounts of Ti additions. The steels with high Ti additions (0.059–0.22Ti) were designed to precipitate TiC particles and those with low Ti additions (0.016–0.02Ti) were designed to precipitate TiN particles. They reported that the most effective particles in inhibiting austenite grain growth at very high temperatures were the TiN particles as opposed to the TiC precipitates. They found that austenite grains averaging 20 μm after soaking in the temperature range of 1200–1250 °C for 15 minutes were pinned by TiN particles with mean sizes of 10 nm as measured through extraction carbon replicas (TEM) [57]. Therefore, good control of the Ti/N ratio during casting helps prevent nucleation of the coarse TiC particles that become crack initiation sites and lead to cleavage fracture modes. Small amounts of Ti are essential in recrystallisation-controlled rolling since the TiN precipitates retard the grain growth of recrystallised austenite.

Not only does Ti wield a strong affinity for N, but also Oxygen (O) and Sulphur (S). Ti forms Ti-sulphide (TiS) and carbosulphide ($Ti_4C_2S_2$), which are more stable than MnS [15], [56], and remain undeformed during hot rolling. Consequently, Ti limits the amount of S available for the formation of the well-known and unwanted MnS stringers. This can be seen in Table 2-2 as reported in a study on Ti-carbosulphide precipitation in Ti-bearing microalloyed steels [58]; where the volume fraction (V_s) of the stringers decreased as the Ti content increased.

Nonetheless, as can be seen in Figure 2.4, in trying to reduce the volume fraction of stringers by forming Ti-carbosulphide and sulfide, the amount of Ti available for the precipitation of TiN also eventually decreases. Therefore, the effects of all elements must be well-considered and optimised.

Table 2-2: Volume fraction of stringers (Vs) in the four Ti-steels [58].

Wt% Ti in steel	$V_s \times 10^4$
0.05	5.0
0.11	1.3
0.18	0.7
0.25	~0.0

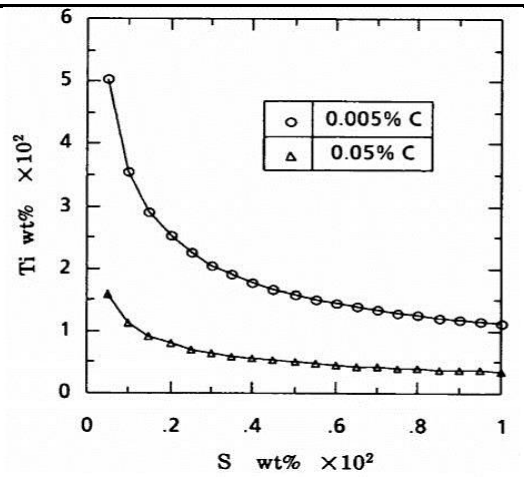


Figure 2.4: Influence of Ti and S on each other with a constant carbon level for an IF-steel (0.005%C) and a microalloyed steel (0.05%C) [58].

Ti additions have also been reported to produce precipitates that play an important role in modifying the composition, size and morphology of inclusions to less detrimental shapes [56]. It was found by Liu *et al.* [59], that the morphology of the inclusions was nonuniform and distorted; that is, the stringers were not elongated due to the presence (in high frequency) of large round Ti-rich globules that also increased in size and number with the increase in Ti concentrations. The authors then concluded that optimum levels of Ti (in the presence of 1.5wt% Mn) should be around 5 to 6 times of that required to tie up the N available as TiN particles to successfully modify the morphology of sulphide stringers. The Ti contents lower than the stoichiometric concentration necessary for the formation of TiN cannot alter the shape of Mn-sulphide.

In conclusion, Figure 2.5 [15], [56], gives a summary of the solubility products that depict the stabilities of the different compounds that form depending on the different elemental affinities and thermodynamic conditions. As previously reviewed, knowledge of the solubilities of these

microalloy carbide, nitride, carbonitride, carbosulphide and sulphide particles is required to arrive at the desired metallurgical states in microalloyed steels. This knowledge is gained through a detailed study and review of the roles of the microalloying elements and the resulting precipitates that form in HSLA steels, consequently offering clear guidance for the selection of microalloying additions for particular purposes.

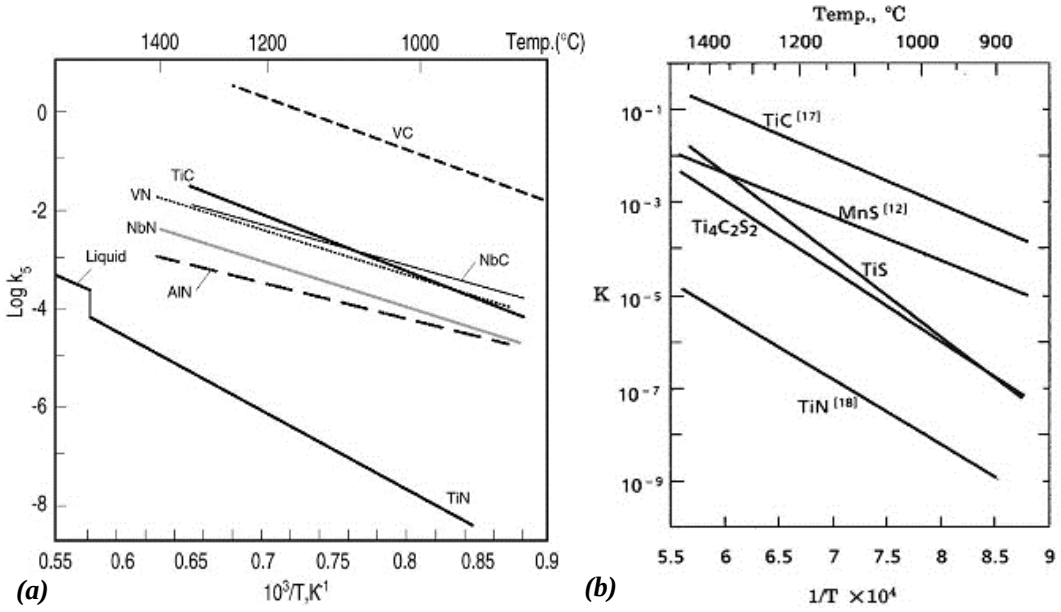


Figure 2.5: Solubilities of microalloy precipitate phases: **(a)** carbides and nitrides, **(b)** carbides, nitrides, sulphides and carbosulphides [15], [56].

2.4 Nil-recrystallisation temperature (T_{NR}) empirical models

The nil-recrystallisation temperature, T_{NR}, is a critical temperature that is vital for grain refinement during the hot rolling of microalloyed steels. If the final rolling passes occur at temperatures lower than the T_{NR}, the highly deformed austenite grain structure contains high dislocation densities that serve as ferrite nucleation sites, thereby ultimately exhibiting a fine ferrite grain structure [60]. T_{NR} is the temperature below which no recrystallisation occurs during a thermomechanical treatment, either during the hot rolling itself or during the interpass time between consecutive passes. Several empirical models for microalloyed steels that are used to predict T_{NR} values have been reported in the literature, some of which are given in equations 2.1 – 2.4 [61]–[63];

$$T_{NR} = 174\,log\left[Nb\left(C + \frac{12}{14}N\right)\right] + 1444 \quad (2.1)$$

$$T_{NR} = 849 - 349C + 676\sqrt{Nb} + 337V(R^2 = 0.72) \quad (2.2)$$

$$T_{NR} = 887 + 464C + \left(6445Nb - 644\sqrt{Nb}\right) + \left(732V - 230\sqrt{V}\right) + 890Ti + 363Al - 357Si \quad (2.3)$$

$$T_{NR} = 203 - 310C + 149\sqrt{V} + 657\sqrt{Nb} + 683e^{-0.36\varepsilon};\ \textit{where } \varepsilon \textit{ is the pass strain} \quad (2.4)$$

Equation 2.2 developed by Fletcher [62], was developed based on a database of 59 other different T_{NR} temperatures for 17 alloy-steels through stepwise regression analysis [64]. Zaky [65], reported some discrepancies associated with equation 2.3 by Boratto *et al*, [63]. Zaky [65] reported that the model (associated with equation 2.3) gave exaggerated T_{NR} values, and suggested the reason that it does not take into consideration the effect of metadynamic recrystallisation due to high accumulated strain. Furthermore, Homsher [64] also pointed out that the Boratto equation does not account for any N. Equation 2.4 was developed by Fletcher [62], as an improvement of his initial equation 2.2. In addition to the alloy content, this model also factored in the pass strain since deformation parameters also affect the T_{NR}. According to this model, a small change in the pass strain can affect the T_{NR} substantially due to the exponential term. It should be noted that while these developed empirical models reported in the literature help make quick predictions of the T_{NR}, they may not precisely predict the T_{NR} for alloys outside those studies. This is because the utilised empirical constants do not have true physical meaning [64]. Therefore, in the current study, the T_{NR} empirical models were merely used to give an estimate of the T_{NR} for the characterisation of the study-steels in the as-hot rolled conditions. There are other more accurate methods for determining the T_{NR} of steels (out of the scope of the current study). These methods require the simulation of several hot rolling passes and the successive graphical depiction of the mean flow stress *versus* the inverse of the absolute temperature for each one of the passes [11], [60], [65]–[68].

2.5 Thermo-Calc software predictions

Thermo-Calc is a thermodynamic computer software that is used to simulate and predict equilibrium phase transformations as well as precipitate and phase properties in metallic materials based on a particular database. Thermo-Calc also extends into non-equilibrium calculations, such as the so-called para equilibrium transformation [69]. Thermo-Calc performs thermodynamic calculations of which phases can form, at combinations of varying temperatures and alloy chemical compositions. For instance, with the use of the steel database (TCFE), Thermo-Calc accurately predicts the austenite/ferrite carbo-nitride equilibria by performing calculations of expressions that describe chemical potentials of elements in austenite/ferrite and metal carbonitride. It also predicts the influence of an element on the stability of phases, driving forces for nucleation, the solubility of elements in phases, volume fractions of precipitates and their compositions as a function of temperature and/or composition [53], [70]. Thermo-Calc, through its general database for the thermodynamic properties of microalloyed steels (TCFE9), can also calculate metastable equilibria through data extrapolation from stable phase regions [71], [72]. Thermo-Calc essentially links phases that form, which comprise the microstructure of the material, to the chemical composition and processing parameters. Therefore, in many applications such as in industry and scientific research, Thermo-Calc has successfully been utilized in understanding the evolution of an alloy's microstructure before and after production, and in material selection for specified applications.

As opposed to most steels, microalloyed steels are not primarily made to meet specific chemical compositions, they are however designed to provide superior mechanical properties [70]. Such mechanical properties as, high strength levels, low-temperature impact toughness, and high heat resistance [73] are achieved due to the metallurgical processes that arise during processing, resulting in a particular microstructure. Precipitation, for instance, is one of those metallurgical processes that is mainly exploited in HSLA steels to improve the strength and toughness levels. Through the precipitation and diffusion add-on modules in Thermo-Calc known as TC-PRISMA and DICTRA respectively, studies have been conducted which simulate the simultaneous kinetics of nucleation, growth and coarsening, and dissolution of multi-phase systems (precipitates) [70]–[72], [74], [75].

Jin *et al*.[70], demonstrated the simulation of NbC precipitation kinetics in austenite and ferrite for microalloyed steels using the TC-PRISMA tool, and the HSLA steels database (TCFE7). Isothermal annealing experimental data from earlier studies [74], [75], on the mean radius, number density and volume fraction of the NbC carbide as a function of time was then superimposed and plotted together for comparison with the Thermo-Calc results (see Figure 2.6). Some correlation within the experimental uncertainty was found, hence, showing good agreement between the modelled and the reported experimental results of the NbC carbides.

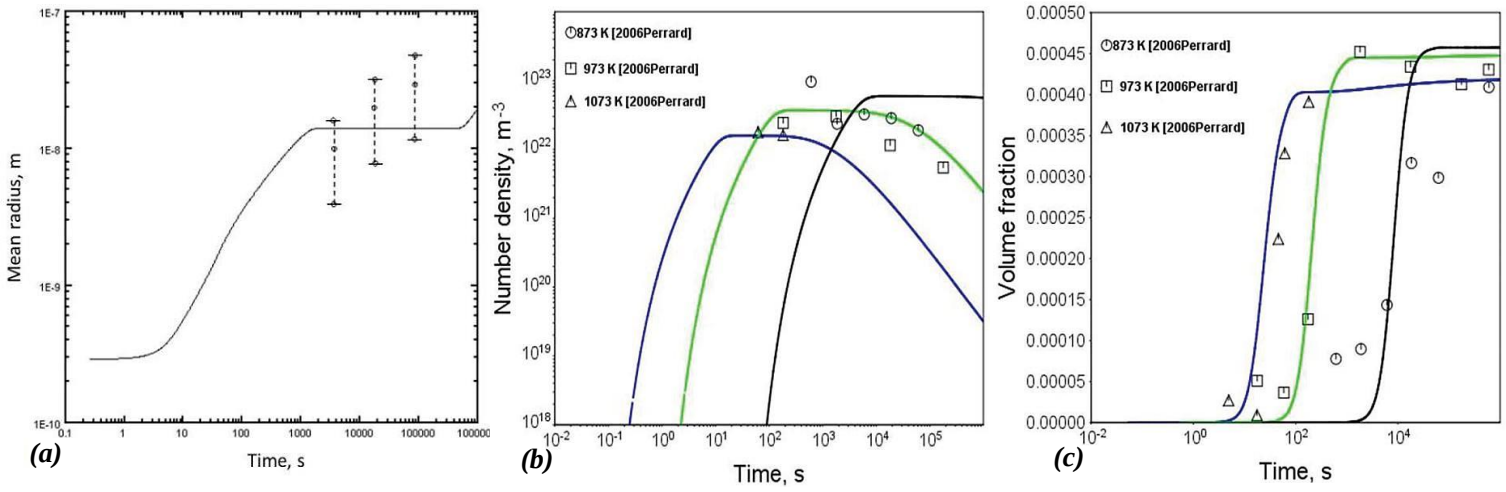


Figure 2.6: HSLA steels' modelled precipitation kinetics of NbC superimposed with experimental data [70]; **(a)** in austenite, at 900 °C, experimental data from [74]; **(b)** and **(c)** in ferrite, at 600 °C, 700 °C and 800 °C experimental data from [75].

It is therefore important to take note from the above discussion that thermodynamic and kinetic modelling using CALPHAD based software such as Thermo-Calc, TC-PRISMA and DICTRA among others provides a powerful means of predicting the effect of process and composition parameters on the microstructures of materials. These CALPHAD based pieces of software have been there since the early 1980s [69], and have been updated almost annually to this day, and therefore makes them very relevant to be utilised in process optimisation, material design and selection for various applications.

2.6 Microstructural banding

In most cases, hot rolled microalloyed steels exhibit a phenomenon called microstructural banding. This is a phenomenon in which one or more phases in a two-phase or multiphase microstructure separate into distinct alternating layers parallel to the rolling direction due to the elongation of microsegregation [25], [76]. In hypoeutectoid steels, this banded structure generally comprises of planar alternating layers of ferrite and pearlite. Depending on the cooling rate and hardenability of the steel, microstructural banding constituents can also include, ferrite-bainite, ferrite-martensite, pearlite-bainite and bainite-martensite [77]–[79]. Figure 2.7 shows a micrograph of typical microstructures showing ferrite-pearlite banding in as-cast and as-hot rolled hypoeutectoid steel. Many studies have been conducted regarding microstructural banding in hypoeutectoid steels, most of which have documented the causes and mechanisms of band formation [24], [80]. The root cause of microstructural banding has been reported to be residual interdendritic microsegregation of alloying elements during solidification, and among other influential factors such as prior austenite grain size; work-hardened condition of prior austenite; and the cooling rate during transformation [24], [76], [78], [80]. Microstructural banding eventually affects the mechanical properties of steels, and previous studies have documented how banding impacts mechanical properties and how it can be mitigated through different types of heat treatments [27], [28], [76], [81].

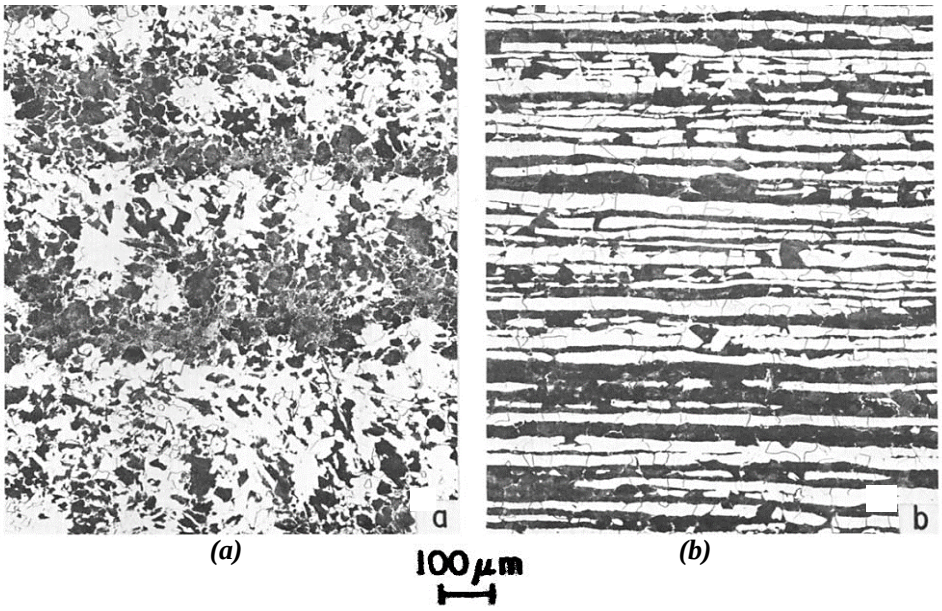


Figure 2.7: Development of ferrite-pearlite microstructural banding from microsegregation in low-carbon steel; **(a)** ingot structure, **(b)** hot-rolled plate [28].

2.6.1 Evolution of microstructural banding

Ideally, the chemical definition of steel connotes that solid steel products have uniform chemistry throughout their sections after being manufactured. While this is true for the liquid steel at the end of the steelmaking process, solidification results in both macroscopic and microscopic partitioning of chemical elements between the liquid and growing solidification front [82]. This ends up producing a nonuniform chemical element distribution throughout the solidified as-cast steel product. The partitioning of chemical elements during the solidification process is known as segregation. From a macroscopic perspective, segregation manifests itself in cast steel products (even after hot rolling) as a centre line, and on a microscopic level attests between dendrites in the solidified product. It is this microscopic segregation that ends up in the alignment into alternating longitudinal and parallel layers after hot rolling consisting of different microstructural constituents and being referred to as banding [83]. The main cause of microstructural banding has in many studies been reported as microsegregation of chemical elements [28], [79], [82]–[84].

2.6.1.1 Microsegregation

During the solidification of liquid steel, there are two main reciprocally related phenomena that govern the whole solidification process. These are known as, solid crystal growth and chemical partitioning between the solid and the liquid [83]. Solid crystal growth involves the advancement of the solidification front into the liquid metal as cooling takes place, this is then governed by the partitioning of chemical elements between the solidified metal and the liquid at the solid-liquid interface. Solidification is a slow process that does not occur instantaneously, rather it proceeds at the rate at which an interface (solidification front) between the liquid and the solid phase moves into the liquid. The chemical elements are uniformly dissolved in the liquid steel. Although it is known that diffusion in the solute-enriched liquid phase is comparatively several orders of magnitude greater than in the solid for it to be able to feed the solute-depleted solid, this does not apply with the solute-depleted solid phase when cooling [85]. Diffusion is much slower in the solid phase than in the liquid phase. Therefore, the solid phase does not accept the solute fed by the liquid phase at the same rate at which it is to be transported into the solid phase matrix to approach the average composition of the alloy at the end of the solidification process. The result of this is a nonuniform solute concentration distribution throughout the solidified metal section. The areas of the metal section that had initially solidified typically display a lower solute concentration as compared to the later solidified regions. Figure 2.8 shows two schematic diagrams: *(a)* representation of a portion of a binary equilibrium phase diagram which can be used to illustrate a departure from equilibrium where the liquid solidifies to a solid phase; and *(b)* illustration of a solid-liquid interface with accompanying changes in concentrations [86]. However, equilibrium is only assumed within the liquid up to the solid-liquid interface, and non-equilibrium conditions in the solid.

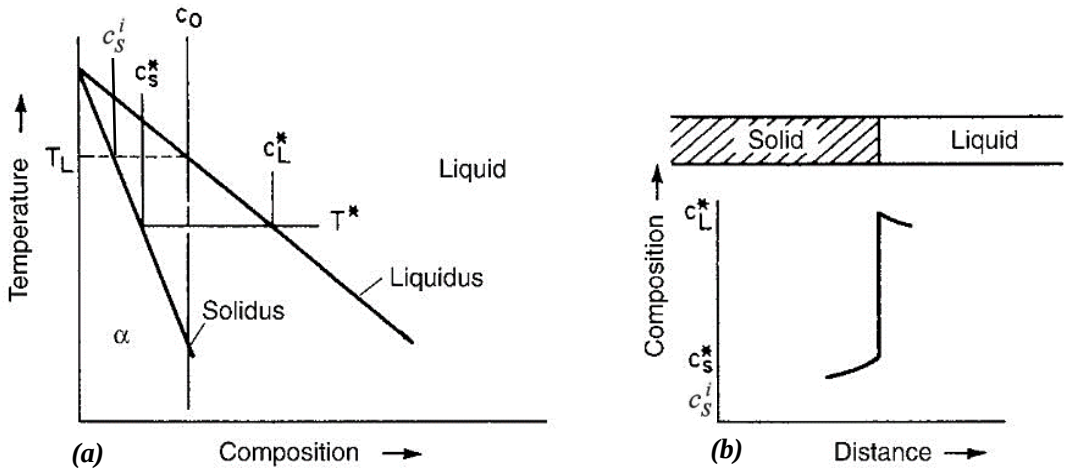


Figure 2.8: Schematic diagram of the solidification of a binary alloy with equilibrium at the solid-liquid interface: **(a)** phase diagram; **(b)** composition profile across the solid-liquid interface [86].

Solidification for the alloy in Figure 2.8 with composition C_0 will take place when the temperature is lowered below the liquidus temperature, T_L; and the first piece of solid will form at this temperature. This infinitesimally small volume of solid that first appears has a concentration given by the solid left end of the tie-line, C_S^i, connecting the point C_0 at temperature T_L. Physically, the concept of local equilibrium implies that the transfer of atoms across the interface is much faster than the diffusion of solute atoms through the solid phase [87]. Solidification advances as the interfacial temperature decreases from the liquidus temperature, T_L, to a certain temperature T*. At temperature, T*, local equilibrium dictates that the solute concentration in the solid phase at the interface is given by C_S^* and at the interface in the liquid phase is C_L^*. The solute redistribution phenomenon originates from the fact that the solid that forms at temperature, T*, has a concentration that is greater than that which forms initially at T_L [86], i.e., (C_S^*>C_S^i), which denotes solute depletion for that first infinitesimally small volume of solid, versus a wave of enrichment (C_L^*>C_S^*) ahead of the advancing growth front in the liquid. This is happening with the assumption that there is no diffusion and therefore no mixing in the solid phase, causing a nonuniform concentration profile to develop behind the advancing interface.

The solute enrichment in the liquid just at the interface causes the actual temperature of the liquid phase to drop below its freezing point. The result of this is another physical process called constitutional supercooling (or undercooling). This is a form of undercooling that is dependent on the localised chemical composition of the alloy near to the growth front as a result of the solid freezing at a different composition than the liquid immediately ahead of the growth front [87]. This concept was first proposed by Rutter and Chalmers [88]. They reported that the accumulation of

solute atoms results in the formation of a layer (adjacent to the solid-liquid interface) of liquid that is below its equilibrium liquidus temperature, therefore, rendering the interface unstable. The mechanism of this process is illustrated in Figure 2.9. As proposed by Rutter and Chalmers, to produce this effect of constitutional undercooling, the equilibrium liquidus temperature versus distance curve and the actual temperature versus distance curve in the liquid should intersect as shown in Figure 2.9 (condition *a*).

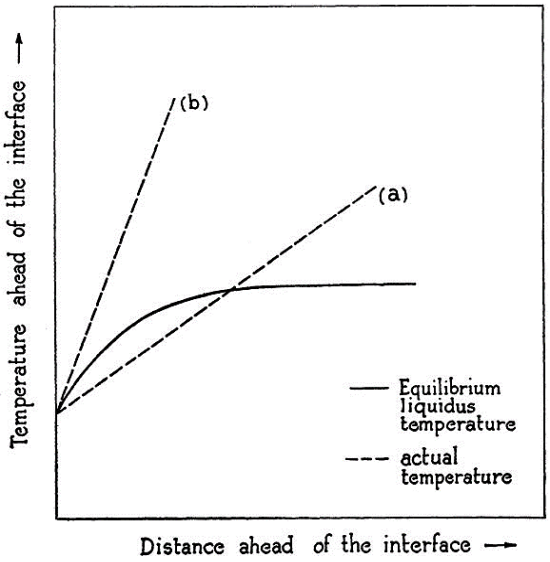


Figure 2.9: Temperature distribution profiles of the actual liquid temperature and its equilibrium liquidus temperature during solidification of a liquid alloy; **(a)** showing necessary conditions for constitutional undercooling, **(b)** conditions that eliminate constitutional undercooling [89].

Walton *et al*. [89], derived a model, equation 2.5 (based on another model by Tiller *et al*., [90]) that helps to predict the equilibrium liquidus temperature, T_E, at every point in the liquid:

$$T_E = T_0 + m C_L - m C_0/k \qquad 2.5$$

where T_0 is the temperature of the interface, m is the slope of the liquidus, C_L is the solute concentration at any distance x in the liquid ahead of the interface, C_0 is the initial concentration of the solute in the melt, k is the ratio of the concentration of solute in the solid to the concentration of solute in the liquid (k is also assumed to be constant) [89]. Therefore, this equation describes the equilibrium solidus temperature profile in Figure 2.9. The profile (a) shows the condition where the actual temperature of the liquid phase is lower than the liquidus temperature as caused by the solute enrichment, and the difference between the two temperatures is referred to as constitutional supercooling.

Following all this, the result is microsegregation that either takes the form of composition segregation associated with the cellular structure [87], [88]; or coring which is associated with entrapment between individual dendrite arms with solute enrichment after dendritic solidification as the last liquid solidifies [87]. This chemical microsegregation has a great influence on the nucleation of ferrite and pearlite in the final microstructure of the product, making certain sites preferential to ferrite or pearlite nucleation [79], [91]–[93].

For instance, Verhoeven [93] investigated banding formation mechanisms in hypoeutectoid steels and showed that the alternate bands of carbide forming elements such as V and dispersed carbide, enhanced the formation of bands. Verhoeven further documented that such elements segregate in interdendritic regions and then stabilise banded collections of spheroidised carbide particles in austenite as shown in Figure 2.10(a).

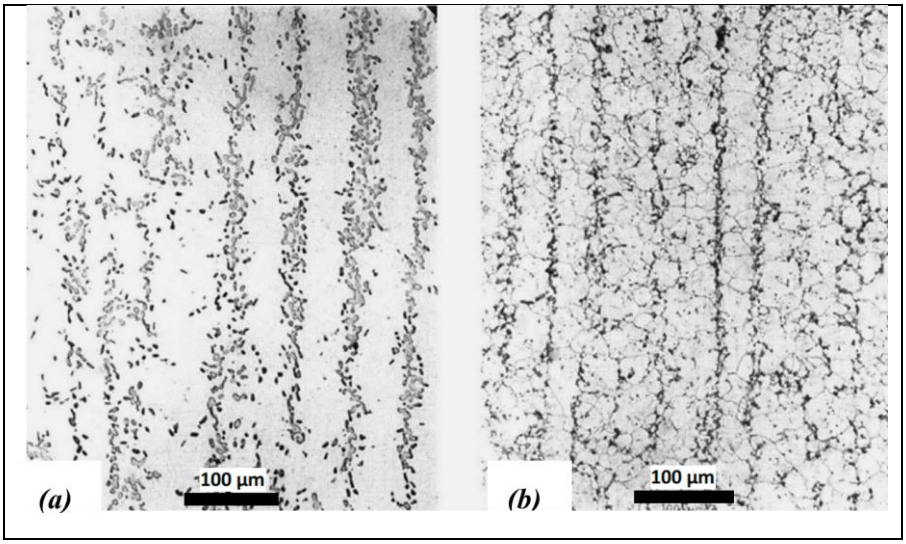


Figure 2.10: Microstructures showing banding mechanism as enhanced by carbide forming elements in hypoeutectoid steel; **(a)** longitudinal section of the as forged sword blade, **(b)** after heat treatment [93].

Again, another study by Verhoeven [79], looking at ferrite-pearlite banding, also stipulated how diffusion coefficients of alloying elements are orders of magnitudes smaller than that of C, therefore causing them to remain segregated into arrangements attributed to the dendritic arrays. The result of this is that upon slow-cooling in hypoeutectoid steels, ferrite preferentially nucleates first along the parallel arranged dendritic or interdendritic bands depending on the level of the Ar_3 in those regions [79]. In evaluating the degree to which some alloying elements influence banding, Kirkaldy *et al*. [94], determined the qualitative effects of alloying elements on the Ae_3 by analyzing and estimating their segregation and typical austenitic diffusion coefficients. With this information, they, therefore, managed to presume that all alloying elements, except for Ni, favour banding since they have large segregation coefficients and low diffusion coefficients, which means they increase the difference in

Ar_3 between the interdendritic and dendritic bands [94]. Also, alloying elements such as Si and P, that raise the Ae_3 (hence the Ar_3) temperature serve to favour nucleation of proeutectoid ferrite first in the bands rich in these elements, consequently, becoming ferrite-rich bands in the final microstructure [91] (see Figure 2.11, EPMA data).

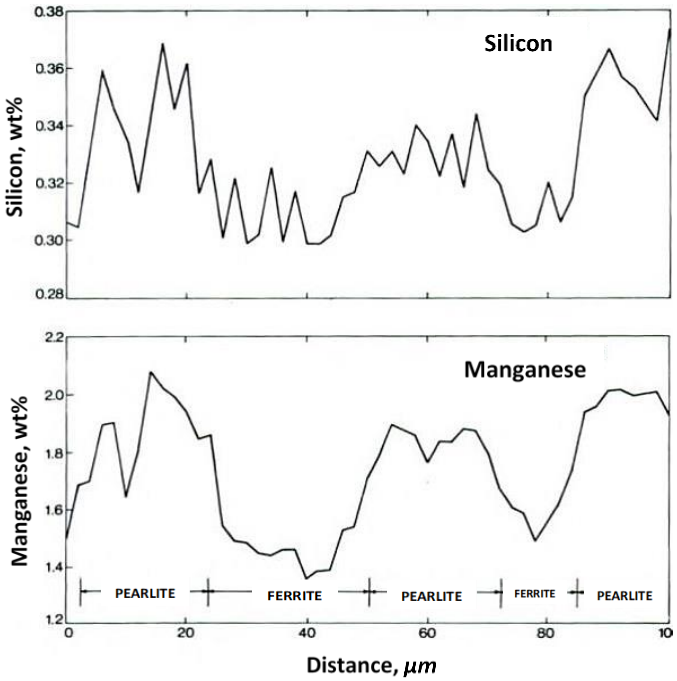


Figure 2.11: Variation of Mn & Si contents across representative ferrite-pearlite bands in the central, longitudinal section of a banded as-rolled 20mm plate steel (0.25C-0.34Si-1.75Mn-0.24Cr, wt%) [91]. Note: The influence of Mn segregation has predominated that of Si which was supposed to enhance ferrite nucleation in Si-rich areas.

Furthermore, Samuels [91] also reported that segregation of austenite stabilizing elements such as Mn results in alternating regions of ferrite (low-Mn regions) and pearlite (high-Mn regions) nucleation. As more ferrite nucleates, carbon is rejected and diffuses to the austenite with high-Mn concentrations, thereby enhancing pearlite nucleation in those regions. Therefore, subsequent hot rolling then introduces the alignment of the interdendritic chemical variations into the pancaked alternating bands parallel to the rolling direction [83].

2.6.1.2 Prior Austenite Grain Size

Prior austenite grain size (PAGS) is another factor that has been investigated and published in several studies as contributing to the development of microstructural banding. The mechanism of austenite decomposition as influenced by the PAGS affects the development of microstructural banding [76]. The effect depends on whether or not the average PAGS is greater or smaller than the chemical band wavelength. Thompson and Howell [76], investigated this aspect in severely banded microstructures and analysed the influence on the mechanism of austenite decomposition when the prior austenite grain size is less than the wavelength of microstructural bands. The authors documented that proeutectoid ferrite grains nucleate in Mn-lean regions with nucleation preferentially initiating at prior austenite grain boundaries (PAGBs), triple points and quadruple points.

Since Mn is an austenite stabiliser, it tends to depress the Ar_3 temperature. Thus, the assumption is that the initially formed proeutectoid ferrite is situated in the Mn-lean regions, on grain boundary triple junctions and quadruple points [95]**;** see the modelled diagrams in Figure 2.12. It should be noted that the schematic diagrams in Figure 2.12 are drawn to scale and therefore clearly depict how the prior austenite grains (PAGs) are smaller than the chemical band wavelength.

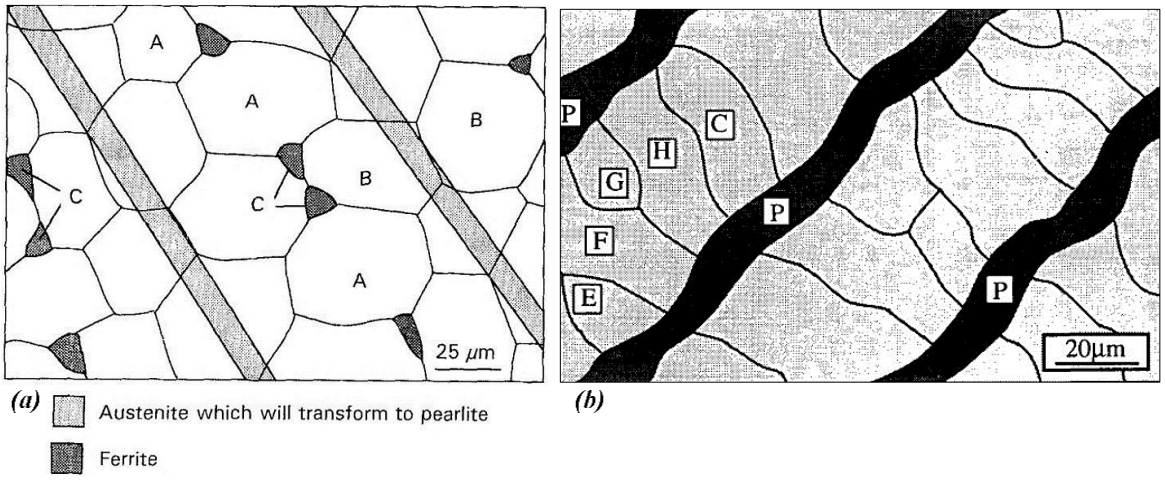


Figure 2.12: (a) Schematic *scale* models of the early stages of the ferrite nucleation. Shaded bands are assumed to be the Mn-rich regions that eventually transform to austenite. Thus, ferrite nucleation occurs in Mn-lean regions **(*arrowed C*)** [95]. **(b)** Final microstructure showing pearlite bands labelled P and ferrite "slabs" labelled C, E-H [76].

Further nucleation of ferrite and growth of the pre-existing proeutectoid ferrite along the preferred locations continues upon further cooling thereby leading to the formation of "slabs of ferrite". Gradually, these slabs end up impinging on one another thereby limiting the ferrite growth in the direction perpendicular to the microstructural bands, towards the Mn-rich regions. As austenite

decomposition finally ends and the growth of the ferrite slabs continues (by favouring a columnar ferritic structure [95]), carbon diffuses towards the remaining austenite and the Mn-rich areas leading to the pearlite transformation. The result of this process is a ferrite-pearlite banded microstructure. Eckert *et al*. [95], further argued that ferrite-pearlite banding does not occur within large pearlite nodules, which they stipulated, stem from the large austenite grains ($> \sim 100\mu m$). In agreement with the latter concept, Samuels [91] reported that prior austenite grain sizes greater than the wavelength of chemical banding result in the disappearance of microstructural banding (Figure 2.13*a–d*). Samuels [91] specifically documented that for PAGS exceeding the band wavelength by a factor of two or three, the microstructural banding tends to disappear and that the influence of the grain boundary area as a preferential site for ferrite nucleation dominates that of Mn segregation. These findings also concur with those of Grossterlinden *et al*. [80], which can be observed in Table 2-3. According to these results, the cutoff value for the critical Mn band spacing to austenite grain diameter ratio (a_{Mn}/d_A) is around 1.5 for the particular steels in their study; below this value, banding does not occur.

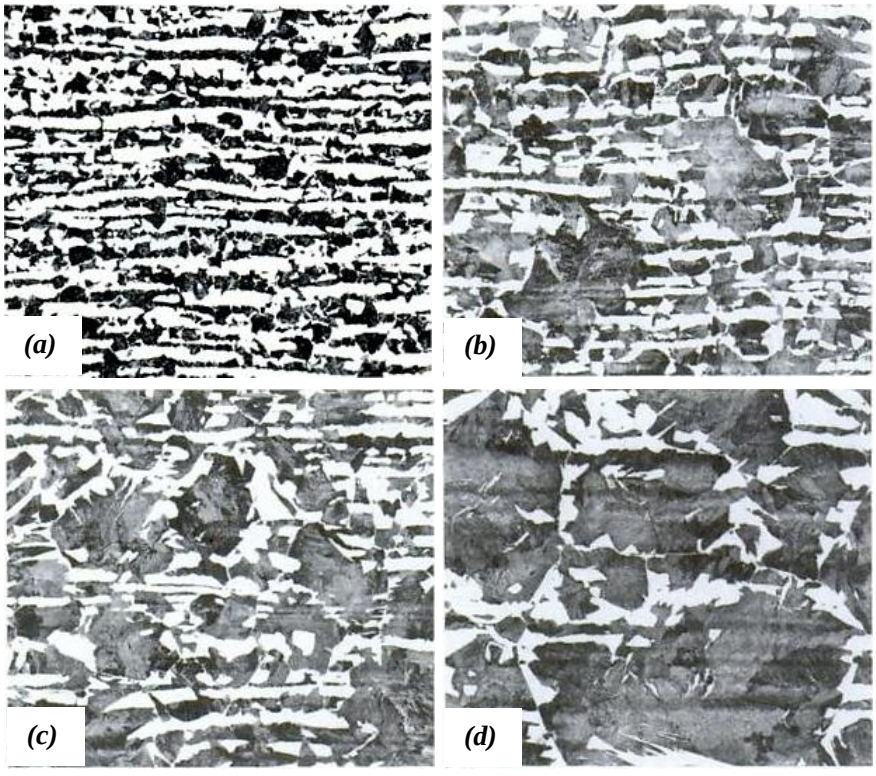


Figure 2.13: Showing a decrease in ferrite-pearlite banding severity from the most to the least severe (*a–d*) as influenced by the PAGS in 0.25C-0.35Si-1.75Mn-0.24Cr *(wt%).* Samples were austenitised at different temperatures for 1hr then cooled at a rate of 5 °C/min; 100x; Picral. **(a)** 825 °C, **(b)** 875 °C, **(c)** 925 °C and **(d)** 1050 °C [91], *p.g.116*.

Table 2-3: Influence of PAGS on the pearlite band spacing in the transformed microstructure [80].

Steel	Austenite grain diameter d_A (μm)	Pearlite band spacing (μm)	Mn band spacing, a_{Mn} (μm)	*Ratio,* a_{Mn}/d_A
1	52	No bands	59	1.1
	35	No bands	57	1.6
	15	77	63	3.9
	8	44	59	6.9
2	35	No bands	42	1.2
	26	Sporadic bands	39	2.6
	16	71	42	2.6
	8	33	39	4.8
	6	25	39	6.1

2.6.1.3 Cooling rate

The cooling rate has also been reported in several studies as a factor that plays a role in the mechanism of microstructural band formation in hypoeutectoid steels [76], [80], [84], [91]–[95]. It should be noted that the critical cooling rate that is required to completely get rid of ferrite-pearlite banding is a function of the steel and its processing history [79]. However, from a general point of view, an increase in the cooling rate from the austenite region tends to decrease the intensity of the ferrite-pearlite banding. This is because a higher cooling rate minimizes the effects caused by the differences among the Ar_3 temperatures of the alternating segregation bands [91]. On the other hand, very slow cooling usually results in severe microstructural banding. Thompson and Howell [76], in a study investigating the factors influencing ferrite-pearlite banding in 0.15C-1.40Mn *wt%* steel, discussed in a comparison between air-cooled and furnace-cooled samples in their study. They intended to show the role of cooling rate in the mechanism of band formation. They found that slow cooling rates were associated with an increased propensity towards the formation of well-defined, alternate bands of proeutectoid ferrite and pearlite thereby promoting a more severely banded microstructure. They attributed this behaviour to the driving force for the proeutectoid ferrite reaction which is higher during air cooling than that of furnace cooling [76]. This is also in agreement with Eckert [95], who also pointed out that a higher cooling rate yields greater driving forces for the ferrite reaction, and therefore lessening the effects of the differences in the Ar_3 temperatures between the Mn-lean and Mn-rich regions.

Several theories have been used to explain the mechanisms behind the relationship between ferrite-pearlite band formation and the cooling rate. Samuels [91] observed ferrite in the form of Widmanstätten and no banding in the microstructures of the 0.25C-1.75Mn-0.34Si-0.24Cr *wt%* steel that underwent higher cooling rates (1500 to 3000 °C/h). Samuels [91], therefore, suggested in his theory, that probably the loss of banding under those conditions could be attributed to the progressive

change in ferrite morphologies from the grain boundary allotriomorphic ferrite (blocky) to the Widmanstätten, Acicular ferrite and finally bainitic morphology [91]. As the Widmanstätten and Acicular ferrite grow, carbon is ejected perpendicular to the fast-growing direction of the fine ferrite needles into the surrounding austenite. Since the ferrite is growing from the microsegregated bands containing the highest Ar_3 temperature value, into the neighbouring bands, the carbon diffuses along the plane of the band. Therefore, pearlite nucleates, not in the form of a band, rather, as a matrix and is mixed between the Acicular/Widmanstätten ferrite structure [79], [92].

Grossterlinden *et al*. [80] presented another theory that describes the mechanism that favours the severe ferrite-pearlite band formation during slow cooling. The authors suggested conditions that favour the formation of banded carbon enrichments during slow cooling. One main condition was that "for banding to take place, the displacement of the γ/α phase boundary and the diffusion distance of the carbon, must be equal to half the primary band spacing" [80]. That is, the blocky ferrite allotriomorphs can only grow a distance half the band spacing to transport the carbon out of the ferrite band. Hence, adequate slow cooling will allow the diffusion of the carbon from Mn-lean to the Mn-rich regions between the Ar_3 and the end-of-ferrite formation temperature interval. Grossterlinden *et al*. [80] substantiated the validity of this condition through the computation of the carbon diffusion-controlled displacement by the finite-difference method. Their mathematical model assumed that ferrite nuclei exist on cooling beyond the Ar_3 temperature. It helped them calculate the distance travelled by the γ/α phase boundary and the adjacent carbon-concentrated region into the remaining austenite in a short cooling time interval between the Ar_3 and the end of ferrite transformation temperatures. Figure 2.14 is a plot of the displacement of the γ/α phase boundary versus the cooling rate, showing the influence of cooling rate on the formation of microstructural banding. Figure 2.15 shows a series of microstructures (***a–i***) produced after continuous cooling experiments by Farahani and Van Der Zwaag [96]. The transition can be observed in the microstructures from high (***a–c)***, intermediate (***d–f***) and low (***g–i***) cooling rates containing ferrite, pearlite, bainite/martensite phases randomly distributed; ferrite-pearlite random distribution; and well-developed ferrite-pearlite bands in the rolling direction, with each respective cooling rate.

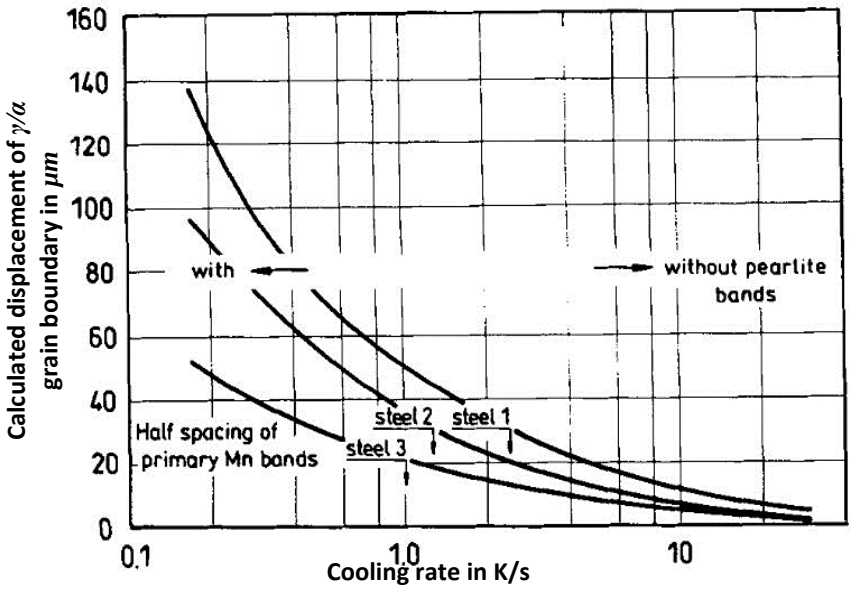


Figure 2.14: The relationship between cooling rate and calculated mean displacement of the γ/α phase boundary during austenite decomposition for 3 study-steels [80]. Steel 1 (C-Mn steel), steel 2 (C-NbTiV steel), steel 3 (C-NbTi steel).

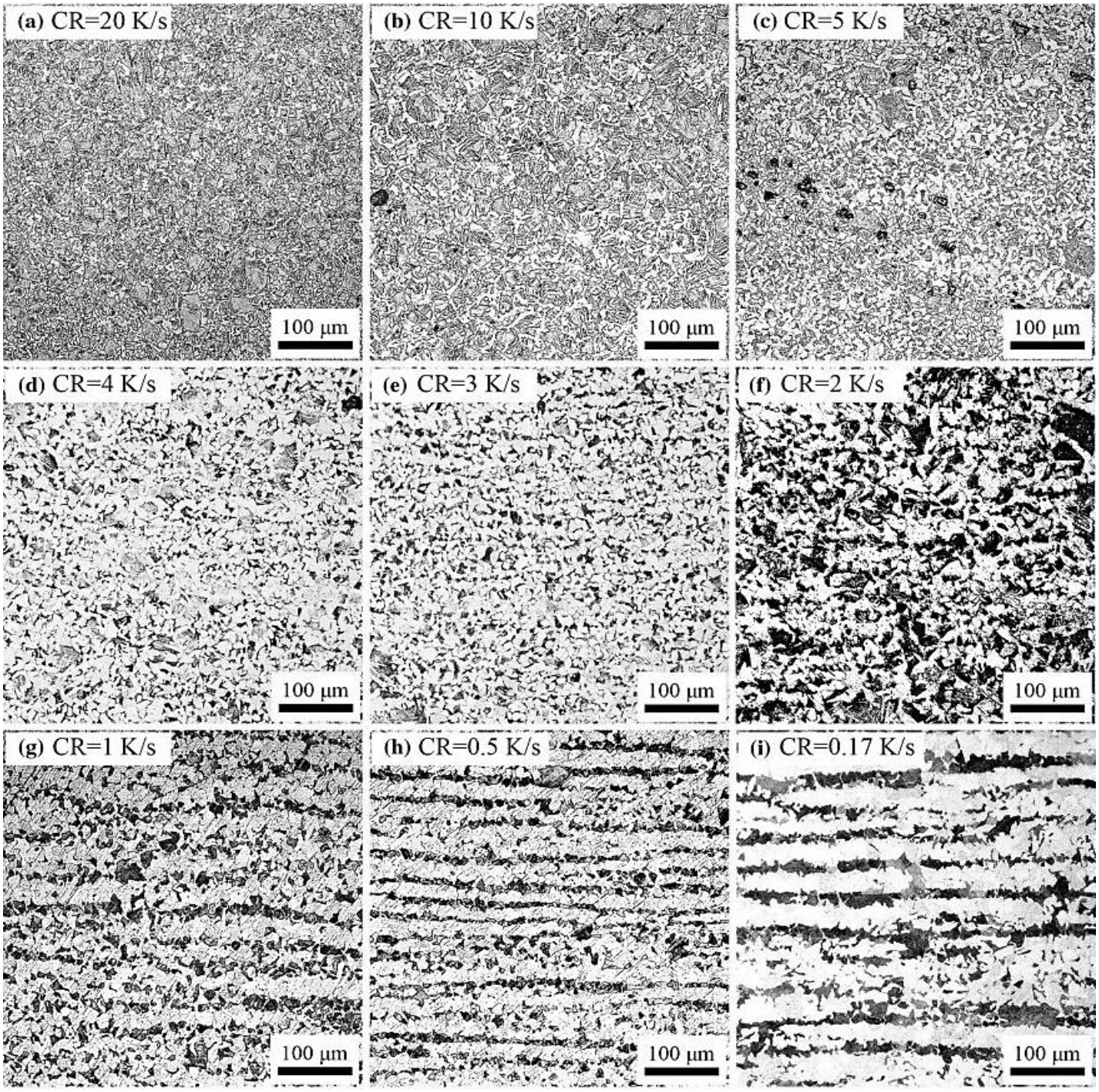


Figure 2.15: Continuous cooling experiments microstructures showing the influence of cooling rate (CR) on ferrite-pearlite microstructural banding in a hot-rolled Fe-0.17C-1.47Mn-1.48Si (*mass %*) steel [96].

2.6.2 Influence of microstructural banding on mechanical properties

Microstructural banding which is a form of inhomogeneity influences the mechanical properties of microalloyed steels, mostly in unfavourable ways. The effects of microstructural banding on the general material property behaviour have been broadly investigated in many studies and reported in the literature, though, with dissimilar conclusions. These effects of microstructural banding have been studied in detail by several researchers and their findings were reviewed as follows.

Celotto *et al*. [97] investigated a type of microstructural banding that they called contiguous grain boundary networks (CGBNs) in the rolling direction. The CGBNs comprise hard second phases. The authors classified it as a type of banding due to its evident consequential chemical segregation in combination with the elongated prior austenite grain morphology that develops in the hot-rolling stages. During tensile loading as in tensile tests, the extensive pre-existing CGBNs (especially hard second phases) and other features (such as pearlite bands) become aligned with the loading direction, thereby making them critical microstructural features regarding crack initiation and propagation. They observed this through tensile testing experiments using in situ observations in combination with digital image correlation (DIC). They found that micro-voids form first as localised plastic strains begin to accumulate in the adjacent ferrite matrix during loading. This also agrees with Khalid *et al*. [98] who observed microcracks at ferrite/pearlite band boundaries after impact loading tests. Therefore, failure originates from such locations. Celotto *et al*. [97] concluded that the pre-existing CGBNs that also contain hard second-phases are more crucial regarding the final failure than any inclusions on their own.

Spitzig [27] reported that microstructural banding had no substantial influence on the yield and tensile strength properties of the study-steels; that is, for the given steels in banded and unbanded conditions, the tensile strength properties were similar. On the other hand, the total elongation, fracture strain and reduction of area of the steel specimens containing stringer sulfide inclusions were considerably improved after the removal of pearlite banding. In banded structures with globular stringers, however, these properties were unaffected. Spitzig then suggested that pearlite banding was detrimental to tensile ductility only with the presence of stringer sulfide inclusions [27]. This implied that ferrite/pearlite banding has some indirect detrimental effects on tensile ductility and that these effects are accentuated more with the presence of stringer inclusions. This aspect was also in accord with Grange [28]. Moreover, the removal of pearlite banding lowered the ductile-to-brittle transition temperature (DBTT) and more especially increased the Charpy shelf energy [99].

Spitzig and Sober [99], however, concluded that the indirect effect of ferrite/pearlite banding was not so clear cut and obvious as it could only be deduced, hence, not directly attributed to the negative effects (on mechanical properties) to sulfide inclusions.

Grange [28] was able to isolate the microstructural banding effects on the mechanical properties from those caused by inclusions in hot-rolled steels. In the study, the author managed to simulate the production of the same grade of steel in two categories: "clean" (very few or without inclusions) and "dirty" (with numerous inclusions) steel, both in banded and unbanded conditions. The base composition of the steels was the same (0.25C-1.5Mn-0.015P, *wt%*), with the only difference being the addition of 0.019S *wt%* and 0.22Si *wt%* in the "dirty" steel, which consequentially produced numerous inclusions that were elongated in the rolling direction [28]. Similarly, as with Spitzig [27], the Grange [28] reported that the yield and ultimate tensile strength were unaffected by ferrite-pearlite banding; and so was the total elongation, but the reduction-in-area was significantly reduced. This is in agreement with several other studies [81], [98], [100]. Nonetheless, banding lowered the Charpy V-notch (CVN) shelf energy but did not significantly affect the DBTT. Together with the findings on the dirty steel, Grange [28] concluded that microstructural banding and stringer inclusions each, to some extent, evidently accentuate the effect of the other. Thus, the two roughly attribute corresponding effects on the mechanical properties of hot-rolled steel. Even so, severe banding is credibly less detrimental than a comparatively high frequency of stringer inclusions [28]. Figure 2.16 shows a summary of the tensile and CVN impact test results according to the findings of Grange [28].

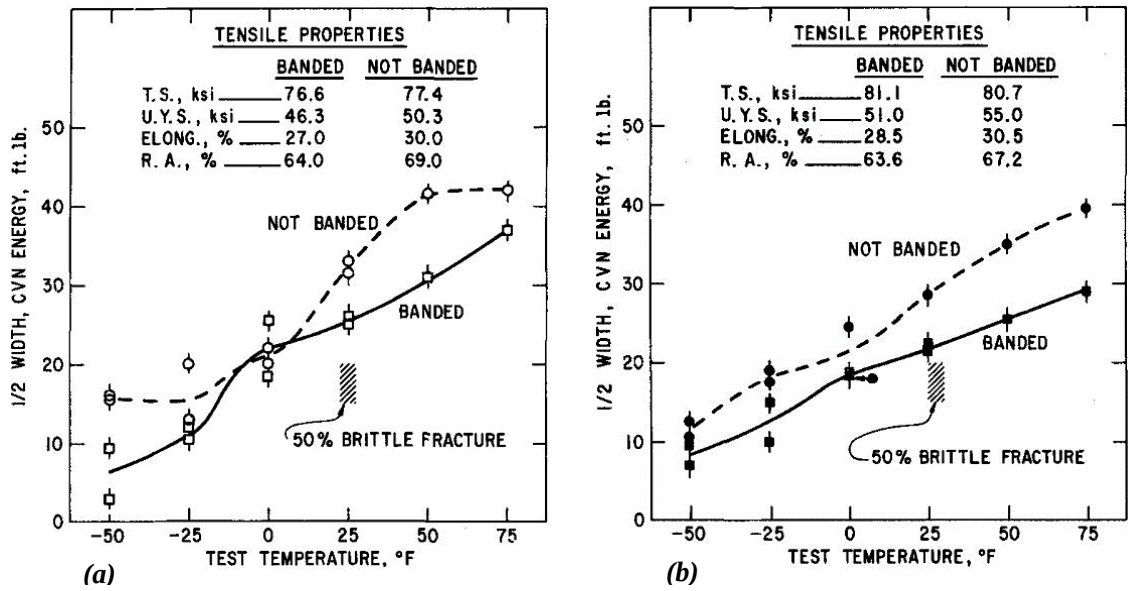


Figure 2.16: Summarised tensile and impact test results for; **(a)** clean steel, longitudinal specimens, and **(b)** dirty steel, longitudinal specimens [28], *p.g. 422.*

Ferrite-pearlite banding has also been reported to enhance hydrogen-induced cracking (HIC). Komenda *et al*. [101] reported that hydrogen diffusion in steel occurs along the ferrite-pearlite band boundaries. The authors observed that the hydrogen content in the hydrogen charged samples depended on the degree of banding, that is, the hydrogen content in the study-steel increased with an increase in the degree of banding. The fatigue crack growth rates due to HIC were amplified in the longitudinal direction of the ferrite-pearlite bands [102]. The mechanism by which the cracks propagate along the bands was described in other studies to be through delamination that manifests in the longitudinal direction of the bands, consequently emerging as microcracks progressing in the direction of crack propagation [103], [104]. With all the detrimental effects that have been reviewed in the above literature, other existing studies have also reported advantageous effects of microstructural banding. For instance, Korda *et al*. [105] investigated the role of pearlite-banded structure on the fatigue crack growth behaviour in structural steel. They observed that cracks that are in the normal orientation to the pearlite band elongation direction (rolling direction) are arrested by the pearlite. Korda *et al*. [105] in agreement with other studies, emphasized that these crack arresting properties are only effective if the banding is continuous, that is, a consistent existence of the banded phase-connectivity [105]–[107].

As it was mentioned earlier in the introduction to this subsection, there are dissenting conclusions in the literature concerning the influence of microstructural banding on the mechanical properties of hot-rolled steels. A conclusion that best summarises different studies on the effects of microstructural banding on the mechanical properties of hot-rolled steels is a quote from Krauss: “Banding may or may not have a detrimental effect on intermediate stages of processing or finished mechanical properties, and if questions arise, banding and its effects merit appropriate evaluation on a case-by-case basis” [83].

2.7 Impact of heat treatment on banding and mechanical properties

Heat treatment is one of the most powerful processes that has been used since the 12th century to alter the microstructure of steels and achieve particular mechanical properties [108]. This is a controlled process that is designed depending on the chemical composition of the steels; desired mechanical properties; and applications of the steel component, just to mention a few. Heat treatment procedures normally start by heating the steel into the austenitic region (austenitisation) to dissolve all the carbides, hence, also the alloying elements in the austenite matrix. This step is primarily for the solutionizing and achievement of a homogeneous austenitic structure. Austenitisation helps to eliminate or minimise any microstructural gradients arising from chemical inhomogeneities in the heat-treated component, otherwise, the final properties will vary in different portions of the heat-treated component. Banding being a microstructural phenomenon can, therefore, be altered with different heat treatment operations. Though heat treatment is meant to achieve desired properties in steels, each heat treatment technique has some limitations in one way or another. Therefore, in most cases, the goal is to arrive at an optimum heat treatment schedule that will produce the desired properties. This section gives a review of several studies on the impact of some heat treatments on microstructural banding, with much emphasis put on normalising and intercritical heat treatments.

2.7.1 Normalising heat treatment

This is a type of heat treatment that involves heating a steel above the upper critical temperature (Ac_3+30-80 °C) into the austenite single phase region, holding at that temperature for some time, and followed by continuous cooling in air to room temperature. The normalising temperature is dependent on the carbon content of the steel; see Figure 2.17*(ii)*. This type of heat treatment was introduced to get rid of the variability in properties that arise in hot-rolled steels [54]. Normalising is normally carried out on steels to: alleviate chemical segregation (homogenisation); improve machinability; recover original mechanical properties of forged or cold worked steels; stress relief and; most importantly grain refinement and a more uniform, finer precipitate distribution [109], [110]. A schematic representation of the normalising cycle is shown in Figure 2.17*(i)*.

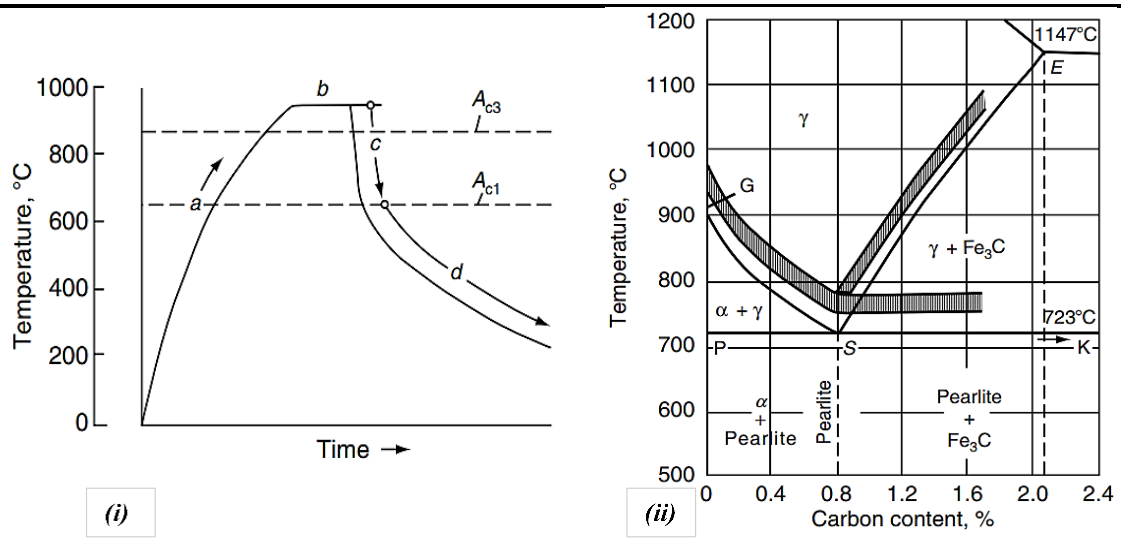


Figure 2.17: (i) Schematic representation of the normalising schedule, *a*-heating, *b*-soaking, *c*-air cooling, *d*-air or furnace cooling. **(ii)** Normalising temperature ranges for plain carbon steels depending on carbon content. Note: The temperature range above the A_{cm} line is applied for secondary carbide dissolution, as cited in [111].

The formation of austenite on the slow heating cycle during normalisation of hypoeutectoid steels occurs by nucleation preferentially at the ferrite-cementite (or pearlite) interfaces followed by growth until the austenite grains meet each other [54]. In ferrite-pearlite starting microstructures, research has shown that austenite formation follows a three-step behaviour [112]. Firstly, austenite nucleates preferentially in pearlite colonies, ferrite-pearlite boundaries, and/or ferrite-ferrite grain boundaries. Secondly, the austenite grows rapidly into the pearlite nodules. Finally, a slow ferrite-to-austenite transformation takes place [113], and the further gradual growth of austenite which consumes the ferrite [114]. In all the steps, the transformation progresses with a redistribution of the carbon in the forming austenite phase, with a varying redistribution scale with each respective step. In the pearlite-to-austenite transformation, it is known that the carbon redistributes over shorter distances than in the ferrite-to-austenite stage [111], [113]. Even after complete austenitisation, that is, after all the ferrite has transformed to austenite, regions of high carbon concentrations and other alloying elements from cementite and dissolving carbides still exist in the austenite. Hence, the need for soaking at the austenitising temperature for a certain period to even out the concentration gradients in the austenite.

The kinetics of austenite transformation during austenitising can be modelled into a sigmoidal curve (Figure 2.18) that fits the Johnson-Mehl-Avrami-Kolmogorov transformation model (JMAK) [115]:

$$V_v = 1 - \exp\{-(1/3)\,\pi\,\dot{N}\,G^3\,t^4 \qquad 2.6$$

Where *Vv* is the volume fraction of the transformed phase, $\dot{N}$ is the nucleation rate, *G* is the growth rate, all taking place after an annealing time, *t*. This model was derived on the assumption of constant $\dot{N}$ and *G*. Despite these unlikely assumptions, it has been proven to still reasonably accurately describe the nucleation and growth kinetics during transformation. Equation 2.6 can be re-written in a more generalised form as:

$$V_v = 1 - \exp(-k t^n) \qquad 2.7$$

Austenitisation, like any other nucleation process, is characterized by an initial incubation time that allows for the formation of the first stable nuclei. This is then followed by a rapid rate of formation of new stable nuclei that eventually grow as the process proceeds [83]. Figure 2.18 shows the percentage volume of austenite that has transformed from pearlite and the influence of temperature on austenite transformation kinetics. Nucleation and growth are diffusion-driven processes, hence, at higher austenitising temperatures, the diffusion rate of carbon increases, which then leads to the rapid formation of austenite. This is depicted in Figure 2.18, where the 751 °C curve appears at shorter times.

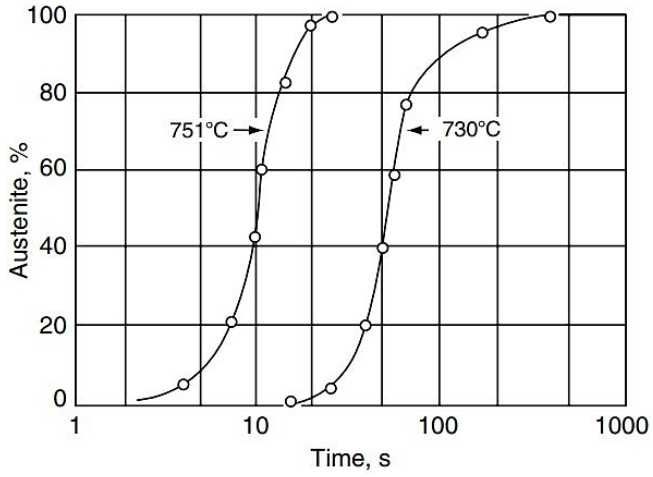


Figure 2.18: The influence of austenitising temperature on the rate of austenite formation from pearlite in eutectoid steel, as cited in [83].

During cooling of a hypoeutectoid steel, austenite decomposition starts with the nucleation of proeutectoid ferrite at the PAGBs with a preference for grain corners and grain edges [116]. However, the amount of proeutectoid ferrite decreases with an increase in the cooling rate from the austenitising temperature, and can even be entirely suppressed with a substantial degree of undercooling [111]. On the other hand, if the cooling rates are relatively slow, then the volume fraction of the proeutectoid ferrite and the carbon content of the austenite increases as the temperature is decreased. The increase in the volume fraction of the proeutectoid ferrite consequently results in the build-up of the carbon in austenite due to the low solubility of carbon in ferrite. With the continued decrease in temperature, the carbon content build-up in austenite continues to the point

where it reaches that required for the eutectoid reaction in the hypoeutectoid steel [83]. Hence, the pearlite transformation takes place in those regions.

The influence of normalising heat treatment on the banded microstructure of microalloyed steels has been documented in previous studies. Varying conclusions have been reached regarding the use of normalising heat treatment to alleviate microstructural banding in hypoeutectoid hot-rolled steels. The effect of normalising temperature on the microstructure and mechanical properties was investigated by Wen *et al*. [112]. Normalising temperatures in the single austenite and the intercritical phase regions were employed. Wen *et al*. [112] reported that austenitisation in the intercritical region led to a fine-grained pearlite band upon air cooling with the original (retained ferrite) ferrite band being coarser; banding was retained. Austenitisation in the austenite region, however, relatively produced a homogeneous ferrite and pearlite grain structure with an excellent combination of mechanical properties being produced at the normalising temperature of 880 °C.

Double austenitising normalising heat treatment cycles were adopted in a study by Chatterjee *et al*. [117], with austenitising temperatures of 950, 1025 and 1100 °C, for 1 hour followed by air cooling. Austenitisation in the second cycle was done at a lower temperature of 750°C for 1 hour and then air-cooled. The first cycle of normalisation heat treatment did not remove the banding effects of the as-hot rolled sample, which the authors reported to be evident in the elongated PAG structure in the rolling direction. After the second intercritical normalisation cycle, the PAGs were more equiaxed. The heat treatment that involved a double austenitisation eliminated the as-hot rolled banded structure and produced a more equiaxed ferrite-pearlite grain structure. The 1025 °C normalising heat treatment schedule produced the optimum combination of strength and impact toughness properties. However, such high austenitising temperatures are not used in industries during normalising heat treatments.

Wang *et al*. [118] investigated the impact of normalising heat treatment on banding in a microalloyed steel for a high-pressure seamless boiler. As reviewed earlier the cooling rate and PAGS are well-known factors that impact microstructural banding. The authors utilised high homogenising temperatures and faster cooling rates than the conventional air cooling in their normalising heat treatments by applying convection. According to their findings, the normalising heat treatments proved to be effective in achieving homogeneity and eliminating the microstructural banding in the study-steels, which was followed by improved mechanical properties. In other studies, homogenisation at 1200 °C for 3-4 hours followed by furnace cooling, and a double normalising cycle at 910 °C for 20 min then air-cooling successfully eliminated banding [119], [120], and also improved impact properties, at the slight expense of the yield strength.

2.7.2 Intercritical heat treatment

An intercritical heat treatment is carried out within the temperature range between Ac_1 and Ac_3, in the ferrite-austenite ($\alpha + \gamma$) phase region. Depending on the chemical composition of the alloy and the intercritical temperature, the percentage composition of carbon dissolved in the fraction of the austenite can be controlled as shown in Figure 2.19.

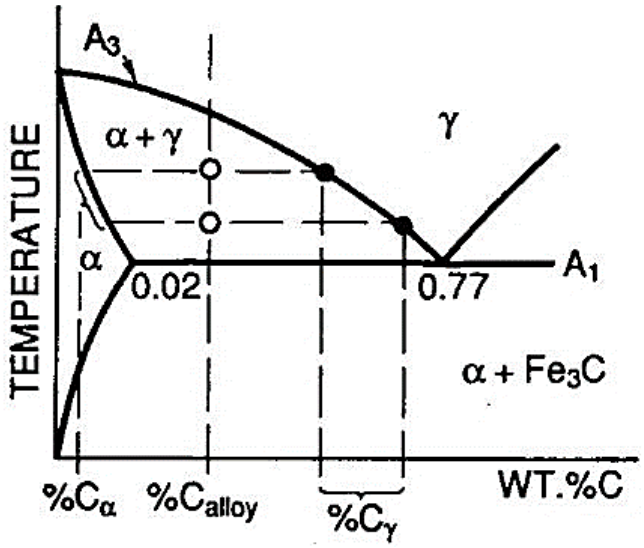


Figure 2.19: Hypoeutectoid portion of the Fe-Fe_3C phase diagram depicting the phases present during different intercritical heat treatments of the hypothetical alloy, where % γ and $\%C_\gamma$ depend on the intercritical temperature [121].

From the above Figure 2.19, one can see that a higher intercritical annealing temperature corresponds to a higher fraction of austenite (which can be estimated from the lever rule) and a reduction in its effective carbon content, thereby generally decreasing the stability of austenite [45], [122]. At lower intercritical annealing temperatures, an adequate annealing time not only enhances austenite-enrichment with C but also Mn, thus contributing to austenite stability [123]. This is a very important characteristic of the intercritical heat treatment since it facilitates the austenite of low-carbon steels to go through transformations typical of medium- and high-carbon structural steel [122]. It is through this characteristic of the intercritical heat treatment that researchers and industries utilise to alter the final microstructure of steel components to what is desired.

Intercritical annealing and the subsequent phase transformations that occur upon cooling are determined by the following features: enrichment of austenite with carbon and partitioning of austenite-forming alloying elements; transformation proceeds with the coexistence of austenite and ferrite phases, thereby facilitating the formation of ferrite from austenite; finally, the annealing time at a temperature [122]. When heating into the intercritical region, the austenite transforms from pearlite through a diffusion-controlled process that takes place by nucleation and growth. Transformation initiates with the dissolution of pearlite colonies followed by carbon redistribution in the ferrite phase which then transforms to austenite [122], [124]. Primarily, an austenite nucleus must form at sites with high carbon fluctuation. Also, austenite preferentially nucleates at ferrite grain boundaries and competes with the growing austenite that initially formed from the prior pearlite colonies [114], [125].

The intercritical annealing temperature, as pointed out earlier, is the key factor that controls the austenite volume fraction and its carbon content during soaking. Wycliffe *et al*. [126], derived an equation that describes the growth rate of the austenite phase boundary:

$$v = \mathrm{D}\frac{dC}{dx}\left(\frac{1}{\Delta C^{\gamma\leftrightarrow\alpha}} + \frac{1}{\Delta C^{c\leftrightarrow\gamma}}\right) \qquad 2.8$$

Where the velocity of the austenite phase boundary, *v*, is proportional to the diffusion constant of carbon in austenite (*D*) and the carbon concentration gradient *dC/dx* within the austenite grain; and also *v* is inversely proportional to the diffusion path *x* including the differences between the carbon concentrations on austenite–ferrite $\Delta C^{\gamma\leftrightarrow\alpha}$ and carbide–austenite interfaces $\Delta C^{c\leftrightarrow\gamma}$ [126]. An increase in temperature, therefore, influences the *v*, thereby also increasing the growth rate of the austenite phase. Hence, leading to an increase in the volume fraction of the austenite. An increase in the intercritical temperature also increases the dissolution rate of pearlite (in a case with an initial ferrite-pearlite microstructure). According to the study by Speich *et al*. [124] on the austenite growth kinetics in a 0.12C-1.5Mn (*wt%*) steel during intercritical annealing, the authors showed that at lower intercritical temperatures (~740 °C) the "equilibrium amount of austenite" only required time of more than 15 minutes, see Figure 2.20. According to this data, one can easily determine the duration for the intercritical annealing for steels with similar contents of C and Mn.

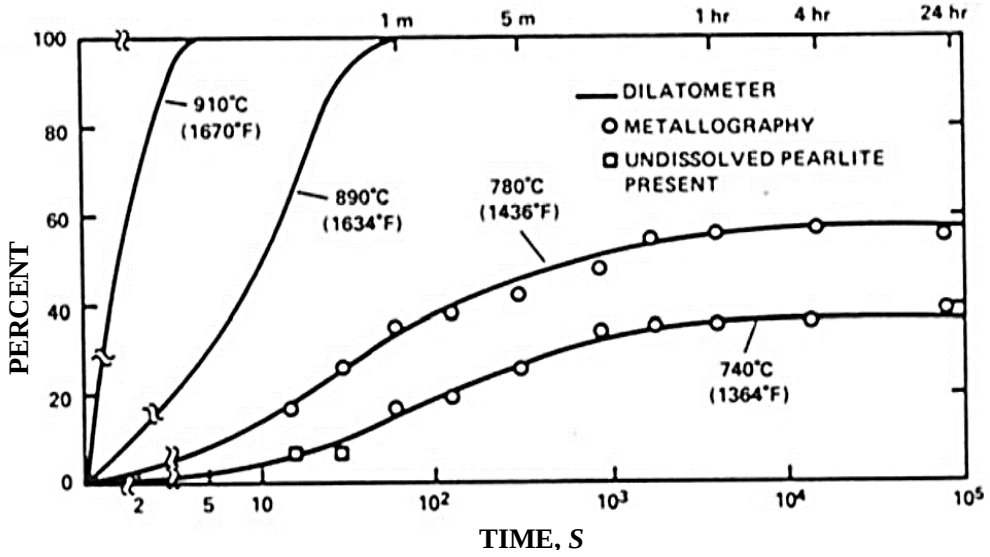


Figure 2.20: Kinetics of isothermal austenitisation at different temperatures for a 0.12C–1.5Mn (wt%) steel [124].

Some important aspects occur during cooling after intercritical annealing and are worth noting. The pre-existent austenite–ferrite interfaces play a major role in facilitating the formation of ferrite. Geib *et al*. [45] reported a unique transformation that involves ferrite forming by an epitaxial growth mechanism that does not form a new interface or grain boundary. The new ferrite (epitaxial ferrite) uses the retained ferrite as a substrate and grows on its interface without the nucleation stage. The authors also found and reported that no precipitation occurs in the epitaxial ferrite which was evident as a precipitate free zone between the epitaxial ferrite and the retained ferrite that was highly precipitated (see Figure 2.21).

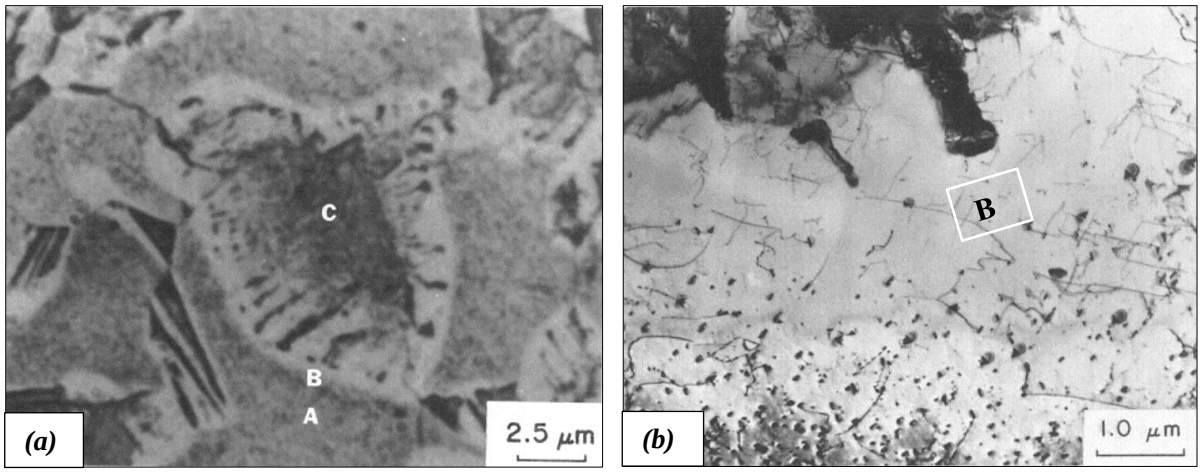


Figure 2.21: Micrographs of Nb-microalloyed steel annealed at 810 °C for 16 min. **(a)** Optical microstructure, region A of retained ferrite, B of epitaxial ferrite and C of the eutectoid structure containing degenerate pearlite. Boiling alkaline chromate etch. **(b)** TEM microstructure depicting the precipitate free zone (evidential presence of epitaxial ferrite) [45].

The epitaxial formation of the new ferrite subsequently results in the further enrichment of the surrounding austenite with carbon. Therefore, this delays the pearlite transformation when compared to cooling after full austenitisation in the austenite single phase region [122]. While the pearlite transformation is shifted toward lower temperatures and slow cooling rates, the ferrite transformation-start temperature is increased [127].

Intercritical annealing has proven to be an effective heat treatment that many research studies have utilised to minimise, eliminate or prevent microstructural band formation in hot-rolled hypoeutectoid steels. In a recent study by Farahani and Van Der Zwaag [96], they investigated the impact of continuous cooling versus the "Cyclic Partial Phase Transformation" treatments (CPPT) in eliminating microstructural banding.

The CPPT treatment was proposed in other earlier studies by Chen *et al.* [128], [129] as an intercritical annealing technique for studying the influence of alloying elements on the kinetics of interface migration. The continuous cooling experiments utilised different cooling rates from the austenitisation temperature of 1000 °C (5 minutes). The CPPT treatments, on the other hand, involved annealing of samples through different cyclic routes within the intercritical phase region aimed at controlling the partitioning of Mn at advancing austenite-ferrite interfaces to suppress the ferrite-pearlite microstructural banding. The Chen *et al.* [128], [129] observed that the CPPT heat treatments successfully suppressed microstructural banding even at those cooling rates that failed to remove banding through the continuous cooling experiments. The authors proposed a mechanism that explains the prevention of band formation due to the CPPT heat treatment in the intercritical phase region. Due to the cyclic heating and cooling within the intercritical region, the austenite-ferrite interface is impelled to reverse its progression direction. Consequently, ferrite formation is paused by the local Mn-enrichment at the advancing austenite-ferrite interface and the sharp increase of Mn that remains behind the interface due to the cycling. As the transformation is paused for that short time, carbon enrichment in the austenite is lessened, causing new ferrite formation in the higher Mn areas during the final cooling thus suppressing band formation [96]. Therefore, it was concluded that continuous cooling was only effective in preventing band formation at higher cooling rates. Furthermore, the CPPT treatments proved to be more effective in preventing microstructural banding even at the low cooling rates that were not effective in the continuous cooling experiments.

Intercritical heat treatment of HSLA steels has also proved to improve the combination of strength and toughness, in addition to minimising (even removing) ferrite-pearlite microstructural banding [80], [130]–[132]. Voigt [121] studied the influence of intercritical heat treatment (ICHT) on HSLA cast steels, which was compared with that of the quench and temper (Q & T) heat treatment. According to the findings of the study, the ICHT produced better toughness results than the Q & T. However, this was accompanied by a 13% drop in yield strength, with the ultimate tensile strength (UTS) only being 4% less than the one after the Q & T heat treatment. The observed improvement in toughness was in both upper shelf energy and DBTT. Figure 2.22 shows these results.

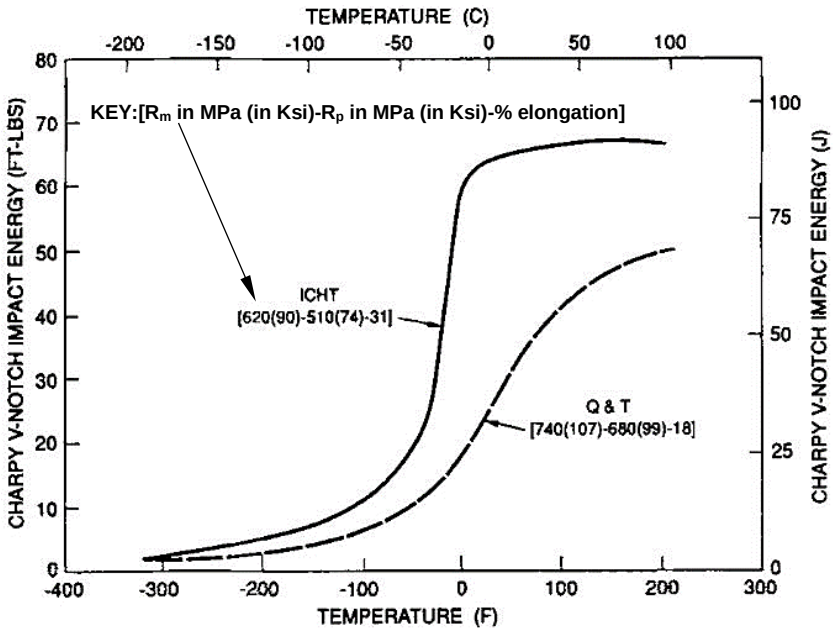


Figure 2.22: Tensile and impact properties of the HSLA steel after ICHT and Q&T [121].

Voigt [121] further emphasised that the real benefits of combined toughness and strength brought about by the ICHT are more evident in HSLA steels as compared to other grades such as C-Mn and low alloy steels. Table 2-4 shows a summary of data from the author's research as well as other literature sources that he compiled to compare the influence of the Q & T, normalise and temper (N & T) and more especially the ICHT on HSLA steels and other steel grades.

Table 2-4: Typical Yield Strength/Ultimate Tensile Strength ratios for cast steels subjected to various types of heat treatments [121].

Cast Steel	YS/UTS
C-Mn, C-Mn-Ni	
Q & T	0.75
N & T	0.65
ICHT	0.70
Low Alloy (86xx type)	
Q & T	0.89
N & T	0.72
ICHT	0.75
High Strength Low Alloy	
Q & T	0.92
N & T	0.80
ICHT	0.83

Grossterlinden *et al*.[80] also mentioned how pearlite banding makes plain carbon steels sensitive to the intercritical heat treatments in a negative manner. They showed the general influence of the intercritical heat treatment on CVN impact toughness in steels with and without ferrite-pearlite banding. In the as-hot rolled condition, the notch impact toughness curves of the two steels in their study were found to be similar. However, after the intercritical heat treatment, the toughness of the steel with banding was more greatly impaired as compared to that which had no banding. The DBTT of the banded microstructure after the heat treatment had largely increased. Caballero *et al*.[26] investigated the evolution of microstructural banding and the optimisation of the intercritical annealing temperature to avoid banding. Similar to what was reported in [28], [91], [92], Caballero *et al*.[26] concluded that banding is eliminated by fast cooling from high hot-rolling temperatures but, reverts after high-temperature (~800 °C) intercritical annealing followed by slow cooling. However, after optimisation heat treatments in the $\alpha + \gamma$ phase region, Caballero *et al*.[26] concluded that the use of low intercritical annealing temperatures (~750 °C), high cooling rates and long soaking times are effective in eliminating microstructural banding.

2.8 Conclusion

The review of the previous literature has shown that different types of heat treatment cycles have been utilised in many studies, either to minimise the degree of banding or eliminate banding, and varying conclusions are drawn from those studies. The microsegregation of alloying elements during solidification being the root cause of microstructural banding. Most authors have concluded that the complete elimination of banding is brought about by the absolute chemical homogenisation during austenitisation [91], [133]. This can only be achieved with very long soaking periods (~26 hours) at high austenitisation temperatures (~1200 °C) [134]; or short soaking periods (~10 minutes) at even higher austenitising temperatures (~1315 °C–1345 °C) [28], which Majka *et al*. [84] and Grange [28], referred to as impractical and beyond economic feasibility for industrial applications. Such high temperatures also exhibit unwanted abnormal austenite grain growth. The use of accelerated cooling rates that are usually higher than the conventional air-cooling (in normalising) has also been reported in many studies dealing with microstructural banding. However, it is not in all scenarios that the cooling rate is a control variable; when it comes to the cooling of significantly large sections or thick plates, the cooling rate largely depends on the size or thickness of the component.

CHAPTER 3 EXPERIMENTAL PROCEDURE

3.1 Introduction

This chapter presents specimen materials, specimen preparations and the experimental procedures that were used in the investigation of the microalloyed hot-rolled steels in this study. The procedures used were selected based on scientific information, industrial information (normalising cooling schedules) and knowledge provided by the available literature. The aim of the experimental procedures used in this study was to determine heat treatment parameters that will produce microstructures that attribute to a combination of high strength and impact toughness. Additionally, to eliminate or minimise the coarse and banded microstructure of the as-hot rolled microalloyed steel plates. The achievement of such microstructures requires a fine-grain matrix and precipitates in combination with a general homogeneous microstructure [110], [135]. Finally, this chapter describes the approach to analysing the response of the two studied steel grades to the subjected heat treatments.

3.2 Specimen materials

Two industrial peritectic microalloyed plate steels in the as-hot rolled conditions were provided, from which specimens for the investigations were sampled. The steels were namely VN and NbTiV-steel. These two grades of steel were industrially hot rolled and provided in the following conditions; the VN-steel was-hot rolled from a typical 240 mm thick slab to a 16 mm thick plate (93.3% reduction) in 20 passes with an exit temperature of 860 °C. The NbTiV-steel slab was hot-rolled to a 30 mm thick plate (87.5% reduction) in 18 passes with an exit temperature of 890 °C. Analysis of the as-received material was performed to characterise these hot rolling conditions. Their respective chemical compositions are given in Table 3-1.

Table 3-1: Chemical composition of the steels (mass %).

Steel	C	Mn	P	Si	Ni	Cr	Al	V	Nb	Ti	N (ppm)	S (ppm)
V-N	0.12	1.50	0.012	0.18	0.01	0.03	0.03	0.06	0.001	0.001	94	8
Nb-Ti-V	0.13	1.50	0.014	0.40	0.03	0.03	0.04	0.03	0.043	0.025	53	40

3.3 Metallography

The main aim of metallographic evaluations is to reveal the microstructural constituents of metals and their alloys by employing light optical or scanning electron microscopy (OM or SEM). Thus, microscopy techniques that were employed in the metallographic examinations in this study include the light OM and the SEM. Microstructural characterisation was done on the as hot-rolled and heat treated microstructures for both steel samples. The microstructural characterisation encompasses grain size measurements, phase volume fraction quantification, microstructural banding quantification, precipitate determination, and fractured surface analyses. The combination of these techniques, therefore, helped in the assessment and explanation of the microstructural evolution during and after heat treatment, and in the drawing of conclusions and making recommendations where necessary. All the steps that were involved in metallographic examinations were selected in compliance with the standard, ASTM E3-11 [136]. Metallographic preparations were conducted with great care since incorrect sample preparation may directly affect the interpretation of the microstructure and therefore affect conclusions.

3.3.1 Optical Microscopy

The main focus of this study was on the initial as-hot rolled and after heat treatments microstructural inhomogeneities resulting from banding. Also, the uneven ferrite grain sizes and the microstructural gradient from the near-surface to the centre of the as-hot rolled plate steels. Therefore, the as-hot rolled and post heat treatment microstructures were analysed using this technique.

To carry out the measurements of the grain sizes of ferrite (in the as-hot rolled condition), prior austenite grains (PAGs), and the phase volume fractions (in the as-hot rolled condition), the samples were sectioned from the middle of the plate in the rolling direction using a *Struers Discotom–5* cutting machine. The samples were then mounted using either Bakelite black or thermoplastic transparent hot mounting resin by a hot mounting press, which was then followed by grinding and polishing. Planar grinding to remove surface irregularities caused by the cutting was done from grit size of 240 (rough grinding), all the way to 1200 (fine grinding). This was followed by mechanical polishing from 9 µm to 3 µm finish using the diamond suspension paste and lubricant. Finally, 2% Nital solution was used to etch and reveal the microstructures in the as-hot rolled samples for light optical microscopy analysis. To reveal the PAG structure, Marshall's reagent [137], [138], modified

with two drops of hydrofluoric acid (HF) was used after a pre-etch (5-10 sec) with 2% Nital. All the etched samples were then observed under an optical microscope (*Olympus BX51M*) mounted with a high-resolution digital camera operating with the *Olympus Stream Essentials* software.

3.3.2 Grain size measurements

The quantitative metallographic technique known as the *Heyn's Lineal Intercept Procedure* [139] was used, according to the standard, ASTM E112–13, to measure the grain sizes making sure that test lines yield at least 50 intercepts. This technique was done on different micrographs with the aid of *Image J*® software where a grid of consistently separated parallel test lines of known lengths was randomly superimposed on the micrograph. All microstructures were analysed through-thickness of the plate steels, that is, from the near-surface to the centre. The average ferrite grain size distribution from the surface to the centre in both steel specimens was measured followed by determining its standard deviation. For microstructures containing two or more phases (in this case, ferrite-pearlite), the mean lineal intercept length of the matrix, $\bar{l}_\alpha$, is expressed as a function of the volume fraction of the matrix as shown in equation 3.1 [139]. Therefore, the average ferrite grain size, $\bar{l}_\alpha$, was determined by:

$$\bar{l}_\alpha = \frac{(V_{V\alpha})(L/M)}{N_\alpha} \qquad 3.1$$

where the volume fraction of ferrite, $V_{V\alpha}$, is expressed as a fraction in equation 3.1 and is calculated by a systematic manual point count method [140]; L is the test-line length; M is the magnification and N_α is the number of ferrite grains intercepted by the test line. In addition to the systematic manual point count method, *Image J*® software was also used to verify the volume fraction of pearlite and ferrite through the threshold method.

The as-hot rolled samples were sectioned for austenitisation and quenching thermal cycles to study the PAG structure. To achieve hardenability, the samples to be austenitised were sectioned into 5×16×16 mm (for the V-N steel) and 5×16×30 mm (Nb-Ti-V). Austenitisation was done at various temperatures (870–1050 °C) in muffle furnaces for 2 hours followed by water quenching. For the PAGS measurements, the number of grains intercepted by test lines were counted and then the PAGS was determined from a combination of equations 3.2 and 3.3 [139]:

$$\bar{N}_L = \frac{N_i}{L/M} \qquad 3.2$$

where $\bar{N}_L$ is the average number of intercepts per unit length of the test-line, L; N_i is the number of intercepts on the field and M is the magnification at which the micrograph was taken. The mean lineal intercept length (average grain size), $\bar{l}$, was determined by equation 3.3 and then its standard deviation calculated:

$$\bar{l} = (\bar{N}_L)^{-1} \quad 3.3$$

3.3.3 Characterisation of the banding extent in as hot-rolled microstructures

Microstructural banding can be identified qualitatively through the appearance of the banded or layered structures, which is normally the initial stage of determining microstructural banding. More details on the banded structure can then be determined through a quantitative approach that measures the degree of microstructural banding. The ASTM E 1268-01 standard practice [25] for assessing the degree of banding or orientation of microstructures was used to characterise the extent to which the as-hot rolled microstructures were banded. The following set of parameters were used to characterise the extent of microstructural banding in the as-hot rolled samples: anisotropy index (AI); mean spacing, centre-to-centre, of the banded phase ($SB_\perp$); mean free path spacing, edge-to-edge, of band spacing ($\lambda_\perp$). Equations 3.4 –3.6 [25], express these parameters respectively. Figure 3.1 is an illustration of these parameters.

$$\text{AI} = \bar{N}_{L\perp} \Big/ \bar{N}_{L\parallel} \quad 3.4$$

$$SB_\perp = (\bar{N}_{L\perp})^{-1} \quad 3.5$$

$$\lambda_\perp = \frac{1 - V_V}{\bar{N}_{L\perp}} \quad 3.6$$

where $\bar{N}_{L\perp}$ and $\bar{N}_{L\parallel}$ is the average number of feature interceptions per test line with the test lines perpendicular and parallel to the deformation direction respectively, and V_V is the volume fraction of the banded phase. Statistical results were also calculated, and the parameters used are defined in Appendix A.1.

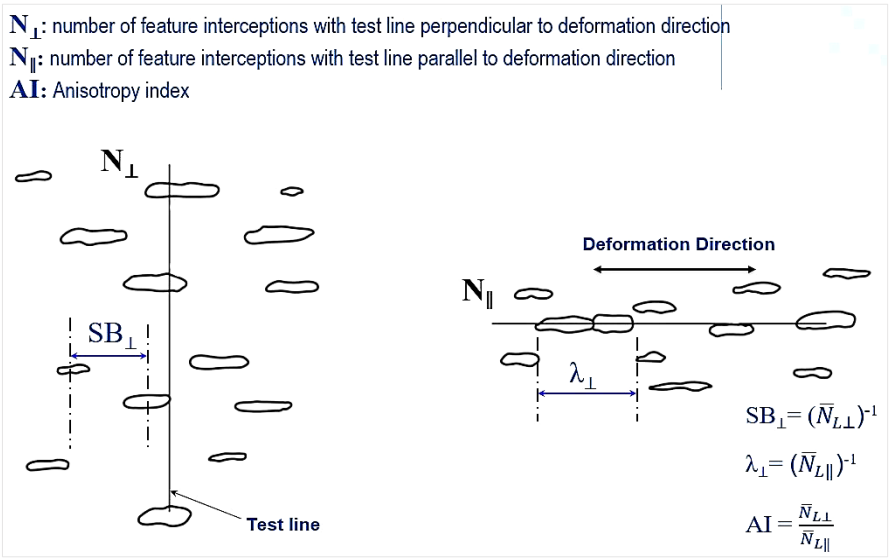


Figure 3.1: A schematic of the assessment parameters for the degree of banding, ASTM E1268-01 [25].

3.3.4 Scanning Electron Microscopy

In this study, SEM had been used mainly for characterisation and qualitative analysis of the heat-treated microstructures. Samples from the heat treatment experiments were mounted in mounting resin and prepared for SEM analysis. The *Zeiss Crossbeam 540 FEG-SEM* was used for the analyses with the use of the *Aztec 3.0 SP1* software. All the steps involved in sample preparations for OM were also followed during the preparation for SEM with some additional polishing steps. SEM samples were fine polished down to 1µm, and then proceeded on to 0.04 µm colloidal silica with the frequent addition of water as a lubricant for 30–60 seconds per sample according to [136]. After polishing, the samples were then etched with 2% Nital solution and taken for SEM secondary imaging analysis.

3.4 Thermal Analysis

3.4.1 Furnace

Muffle furnaces were used to conduct the austenitisation and quench tests for prior austenite grain structure characterisations. The steel specimens were austenitised for 2 hours in the temperature range of 870 to 1050 °C, followed by quenching in still water. The samples were then tempered for 26 to 36 hours at the temper embrittlement temperature of 496 °C. This is one of the techniques that is normally used in hardened low-carbon steels in which tempering is used as a post austenitisation heat treatment that aids the revealing of PAGBs at room temperature after chemical etching. When the steel samples are tempered in the embrittlement range, phosphorus segregates to the PAGBs which then aids the delineation of the PAGBs upon etching [137], [141]. Hence, the post austenitisation tempering heat treatment in the hardened steel samples was utilised in this study to aid the delineation of the PAGBs considering the low amounts of carbon in the study-steels.

3.4.2 Bähr Dilatometry

Bähr dilatometer samples were wire cut from the centre of the as-hot rolled steels in the rolling direction with dimensions of 5 mm diameter ×10 mm length. The *DIL 805A/D* Bähr dilatometer was used in the heat treatment experiments, and the Ac_3 temperatures for the steels were also determined according to the ASTM A1033 [142]. The heat treatment schedules and profiles are shown in Table 3-2 and Figure 3.2 respectively. The parameters (heating rate, soaking temperature and air-cooling rate) that were used in the design of the thermal schedules were selected based on the simulation of the industrial process. A heating duration of 30 minutes to the soaking temperature was used. Simulated air cooling rates as influenced by the size of the products were used as shown in Figure 3.2*(i)*. These cooling rates were generated according to the industrial data in [143]. The heat-treated samples were thereafter subjected to microstructural characterisation.

Table 3-2: Heat treatment simulation schedules

Heat treatment type	Austenitisation temperature [°C]	Soaking time [min]	Cooling rate [air cooling]
NHT	930	30	–
DAHT	930, 775	30	–
IAHT	775	30	–

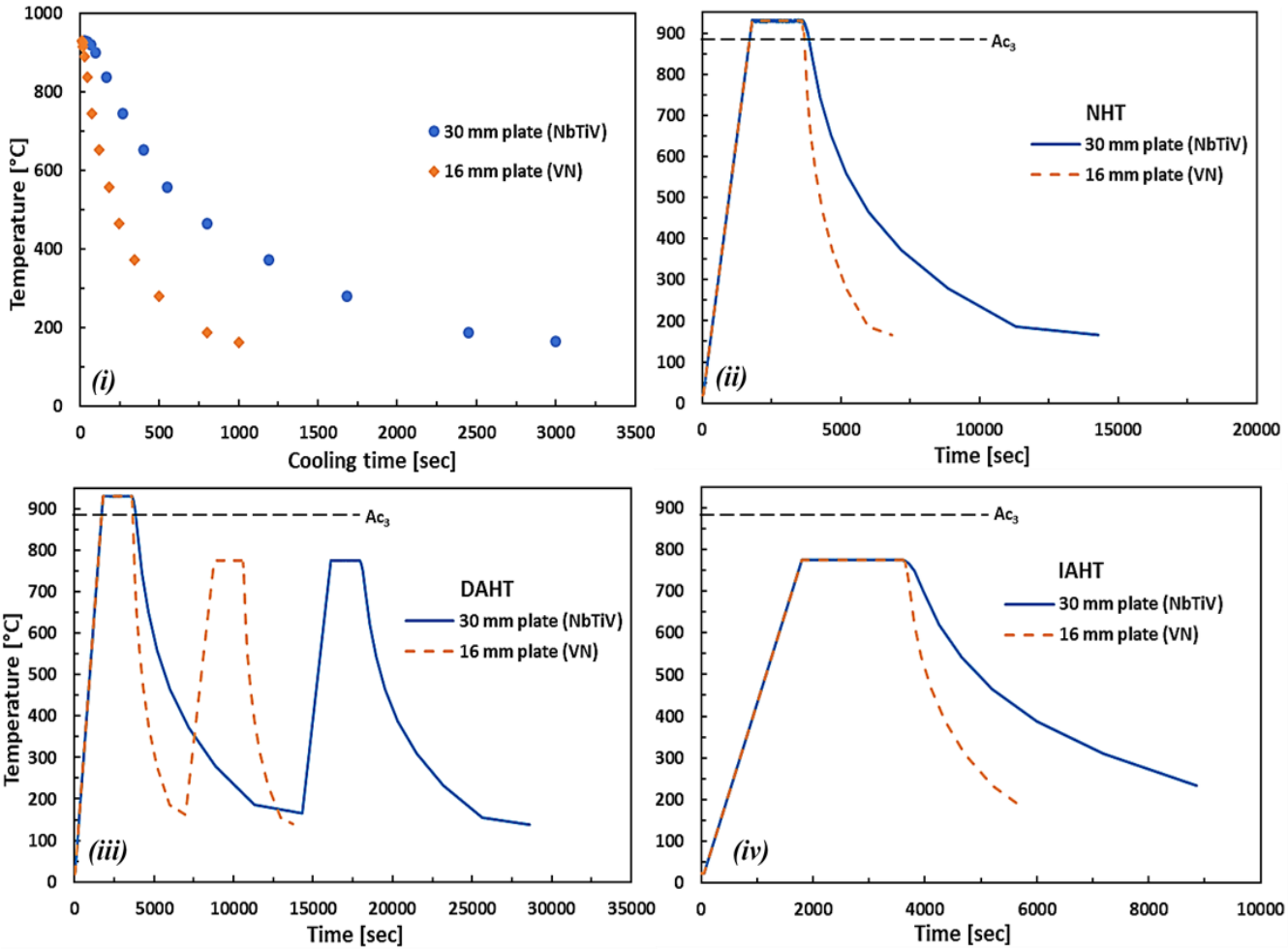


Figure 3.2: Simulated air-cooling rates for the as-hot rolled 16 mm thick by 2500 mm wide VN-steel plate and 30 mm thick by 2500 mm wide NbTiV-steel plate: **(i)** Temperature vs cooling time. Applied heat treatment cycles include, **(ii)** Normalising heat treatment (NHT); **(iii)** Double austenitisation heat treatment (DAHT), **(iv)** Intercritical annealing heat treatment (IAHT). ***NB:*** *Heating duration to test temperature, 30 minutes*.

The 775 °C intercritical annealing temperature was preferred as the optimum (based on the microstructural evolution) among the two other intercritical temperatures of 740 and 810 °C. This was an optimisation investigation of the microstructures of both steel samples. The optimisation was performed for the IAHT and the DAHT. In IAHT, the samples were heated to each respective temperature for 30 minutes and then soaked at the temperatures for 30 minutes after which the samples were then air-cooled by simulation of natural air cooling (see Figure 3.2) depending on the plate thickness. In the DAHT, the first heat treatment cycle was similar to that of the NHT, after which in the second step cycle the intercritical annealing temperatures (740, 775 and 810 °C) were varied. These optimisation heat treatment schedules are shown in Figure 3.3.

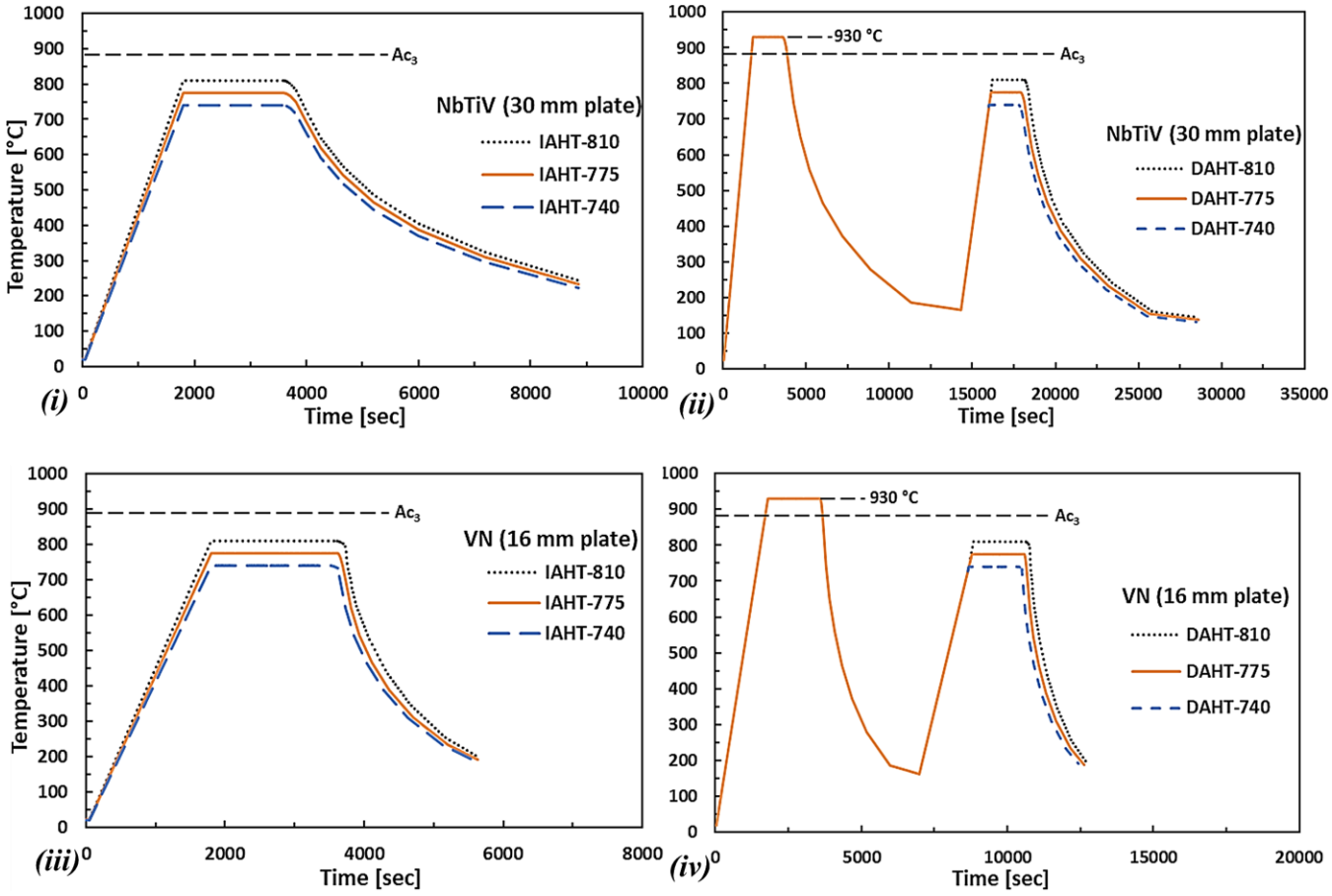


Figure 3.3: Schematic thermal profiles for the intercritical annealing temperature optimisation of the study steel microstructures. ***NbTiV-steel (30 mm plate)***: **(i)** IAHT-810, 775 & 740 °C, and **(ii)** DAHT-810, 775, & 740 °C. ***VN-steel (16 mm plate)***: **(iii)** IAHT-810, 775 & 740 °C, and **(iv)** DAHT-810, 775, & 740 °C.

3.4.3 Gleeble thermomechanical simulator

Physical simulation has become a vital process that is used in engineering materials research and industry. The concept behind the physical simulation of materials is to replicate in a laboratory setting the actual production of the thermal and mechanical procedures that materials undergo during industrial fabrications [144]. The aim is to be able to use the generated information to gain a deeper understanding and improve the full-size manufacturing process. Production processes such as continuous casting, thermomechanical processing, strip annealing, welding and heat treatment can be simulated on the Gleeble thermo-mechanical simulator [145]. In this study, the Gleeble thermo-mechanical simulator was used solely for the simulation of the heat treatments on the steel samples that were supposed to undergo mechanical testing.

The Gleeble™ 1500 thermo-mechanical simulator with resistance heating shown in Figure 3.4*(iv)* was used to heat treat the full-size tensile test and CVN specimens. The same heat treatment schedules shown in Table 3-2 were used. Since the Gleeble was only being used for the heat treatments, the copper grips were therefore used to merely hold the samples; Figure 3.4 *(i)–(iii)* shows the specimen setup. The heat treatment experiments were conducted in an Argon atmosphere and followed by controlled cooling as per the air-cooling simulation cycles in Figure 3.2 *(i)*, also in Appendix A.2 (section 8.2). The K-type thermocouple was spot-welded at the centre of the samples and, therefore, was responsible for the temperature control of the samples during heat treatment. Charpy samples were only notched after the heat treatments to maintain uniform temperature distribution during heat treatment in the unnotched samples, which might not be the case with notched samples. Additionally, it is recommended to finish-machine (including notching) heat-treated materials after the final heat treatment [146]. Three K-type thermocouples were spot-welded on the tensile test specimens as shown in Figure 3.4 *(i)* with the control thermocouple in the middle of the tensile specimens to measure and monitor any temperature differences at a 25 mm distance from the centre.

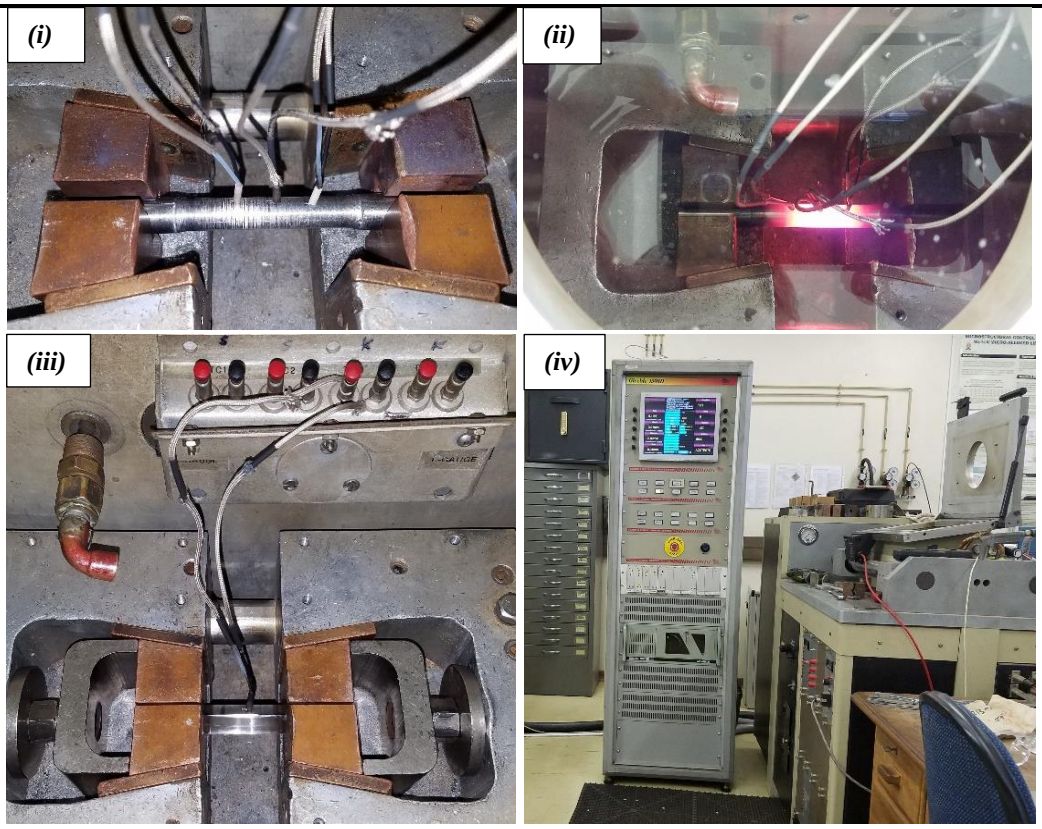


Figure 3.4: (i) Tensile sample arrangement in the Gleeble chamber, **(ii)** Tensile sample during the normalising heat treatment, **(iii)** CVN specimen arrangement, **(iv)** The Gleeble™ 1500 thermo-mechanical simulator.

3.5 Mechanical testing

3.5.1 Hardness measurements

The samples were mounted in plastic resin, ground and polished. Vickers hardness tests were then conducted on the heat treated samples according to ASTM E92 [147] as an initial step to compare the impact of the heat treatments on the samples. The ultimate tensile strength was then estimated from the hardness results according to the ASTM E92 and the use of hardness conversion tables in ASTM E140 [148]. The macro-Vickers hardness test of the heat-treated samples was conducted using a *Future-Tech Macro-Hardness Tester FV-700e* with a diamond indenter. The micro-Vickers hardness test was also conducted on phases for comparison using a *Future-Tech Micro-Hardness Tester FM-700*. Ten readings were recorded per data point of each respective heat treatment. A load of 3 Kg (29.42 N) was used for the macro-Vickers hardness test, while loads of 0.01 Kg (98.06 mN) and 0.05 Kg (490.3 mN) were used for the micro-Vickers test. This variation in the load used for the micro-Vickers was prompted by the fineness of the microstructure to ensure that the indent fell within the targeted phase. A dwell time of 10 seconds was used throughout all the hardness tests.

3.5.2 Tensile testing

Tensile tests were conducted on the steel samples, and the tests were done according to the ASTM E8M [149], and these were done using the *MTS Criterion™ Model 45* tensile testing machine with a load cell capacity of 95 kN, an extensometer with a gauge length of 50 mm, and a crosshead speed of 2mm/min. The tests were conducted on the standard size round tensile test specimens that were machined in the rolling direction and were sampled from the centre of the as hot-rolled steel plates. The specimens were machined according to the dimensions in [149]; that is, the standard 12.5 mm gauge diameter by 50 mm gauge length. Eight samples were machined from both steel grades, with two tests to be done in each condition namely; as hot-rolled and after the 3 heat treatments (16 tensile samples in total). The offset method in ASTM E8M was used to determine the 0.2% proof stress for test specimens that did not exhibit the yield point phenomenon. Upon reaching a plastic strain in the range, $2 < x \leq 5$ %, the extensometer was removed to prevent it from being damaged by the shock at fracture. The tensile mechanical properties were finally calculated according to the same standards.

3.5.3 Charpy V-notch testing

Standard size Charpy specimens (10×10×55 mm) with a 45º V-notch and KV 8 type notch were machined from the plates according to the specifications of the ASTM A370–17a [150]. According to the standard for wrought products, the sample orientation shall be longitudinal, with the notch perpendicular to the major surface (rolling plane) of the product being tested [150]. All the CVN specimens were therefore machined from the as-hot rolled plate in the orientation shown schematically in Figure 3.5. To determine the impact toughness of the steels in their respective conditions, impact tests were conducted using a pendulum impact tester under the standardised procedures according to [146], [150]. The CVN specimens were fractured upon impact by the hammer of a mass of 20.13kg swinging at a speed of ~5.2 m/sec from a height of 1.5m above the CVN specimen resting on the anvils.

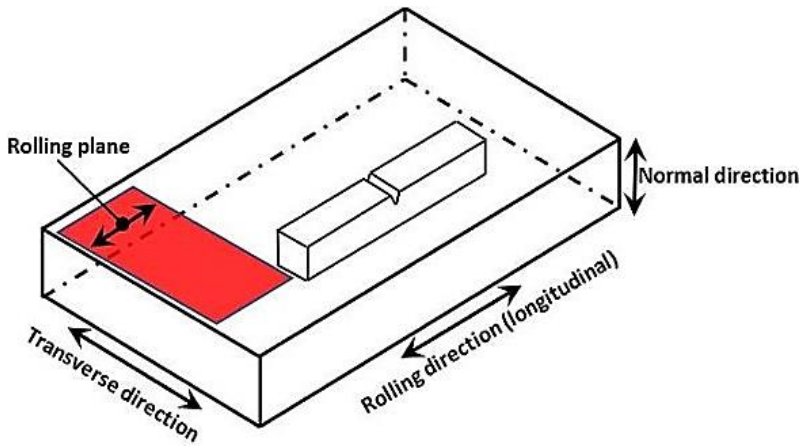


Figure 3.5: Schematic representation of the standard size CVN specimen machining–orientation with respect to the hot-rolled plate.

Before any test was conducted, the first swing of the Charpy machine pendulum was done without any Charpy specimens inserted, that is, it was a free fall run aimed at testing for any friction on the upper bearing of the pendulum. The tests were conducted at a series of temperatures ranging from room temperature to –196 °C (samples submerged in liquid nitrogen). This was to determine the DBTT of the steels in their respective conditions. To ensure the subzero temperature conditions, a mixture of liquid nitrogen and ethanol was used as a conditioning medium which was consistently measured by a thermocouple as shown in the arrangement in Figure 3.6. The samples were held at a particular test temperature (within ±1 °C) for at least 5 minutes and were then transferred to the anvils within 5 seconds. To ensure that the transfer was indeed not more than 5 seconds, the container with the conditioning medium was placed right next to the anvils. If transfer took more than 5 seconds, or if the sample was dropped during the transfer, the sample was returned into the temperature conditioning medium. The transfer was done using centring tongs that were also placed in the conditioning medium, and the centring was done using a self-centring device that is part of the impact tester.



Figure 3.6: An illustration of the arrangement for the test temperature (at –30 °C) conditioning of the CVN specimens. On the right, the black arrow showing liquid nitrogen boiling off of the surface of the ethanol.

3.6 Thermo-Calc™ Predictions

Thermo-Calc is a thermodynamic computer software that is used in the simulation, estimation and prediction of equilibrium phase transformations, precipitates and phase properties in multicomponent materials based on a particular database. Thermo-Calc performs thermodynamic calculations of which phases form at combinations of varying temperatures and alloy compositions under both equilibrium and non-equilibrium conditions. It also predicts the influence of an element on the stability of phases, the solubility of elements in phases, volume fractions of precipitates and their compositions as a function of temperature and/or composition [70].

Before designing any heat treatment schedules for this study, Thermo-Calc version 2018b (TCFE7 steel database) was used to predict and estimate equilibrium phases and precipitates in the two microalloyed steels at soaking temperatures. Although Thermo-Calc is based on equilibrium conditions, it still assists in predicting what to expect regarding microstructural behaviour during thermal treatments. Hence, this information was used to explain the microstructural changes in the studied steels during heat treatment. The phases were calculated according to the chemistry of the two steel grades shown in Table 3-1, in the temperature range of 500 to 1200 °C. Finally, the experimental tests (heat treatment schedules) that were used in this study were then designed according to the results that were initially acquired from the Thermo-Calc software predictions.

Property diagrams plotting the volume fractions of the parent phases and secondary phases (precipitates) as a function of temperature for the study-steels are shown in Figure 3.7 and Figure 3.8 respectively. The plots in the figures show the upper equilibrium transformation temperatures (Ae_3) for both steels. These Ae_3 temperature results were then used to decide on the preliminary austenitisation temperatures before the Ac_3 temperatures were determined through dilatometry experiments. Figure 3.7*(i)* also depicts the ferrite volume fraction of about 0.57 at the intercritical temperature of 775 °C. This served as the optimum volume fraction (closest to 50%) for the intercritical annealing among other intercritical temperatures of 740 and 810 °C with ferrite volume fractions of 0.72 and 0.32 respectively (see Appendix A.3, section 8.3).

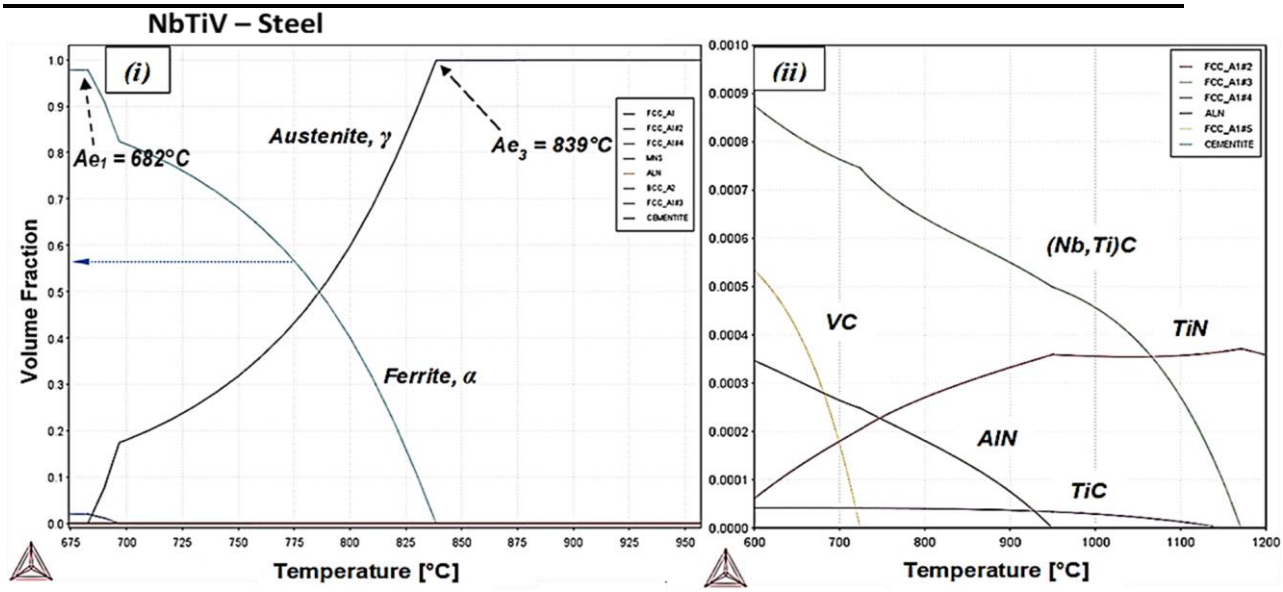


Figure 3.7: NbTiV-steel Thermo-Calc^{TM} results showing: **(i)** volume fractions of austenite & ferrite vs temperature; Ae_3 temperature. **(ii)** precipitate volume fractions and their dissolution temperatures.

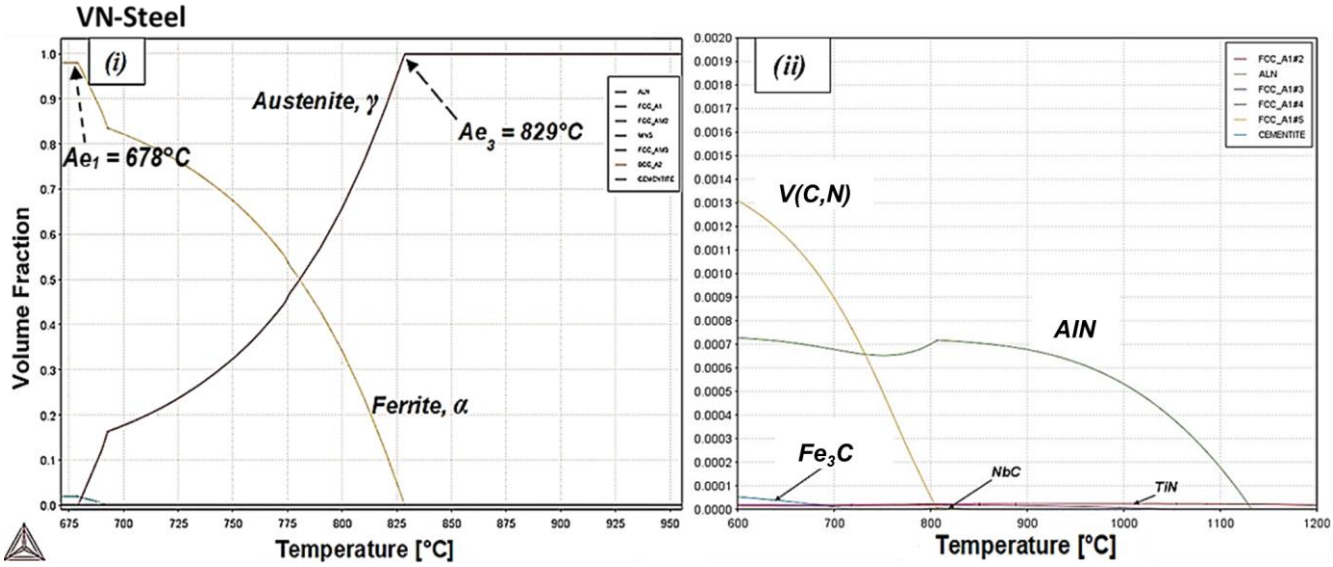


Figure 3.8: VN-steel Thermo-CalcTM results showing: **(i)** volume fractions of austenite and ferrite vs temperature; Ae3 temperature. **(ii)** precipitate volume fractions and their dissolution temperatures.

Figure 3.7 *(ii)* and Figure 3.8 *(ii)* show the expected precipitates in the steels, their decreasing volume fractions with the increase in temperature and the dissolution temperatures for some of the precipitates in the two study-steels. It can be seen that with the austenitisation temperature of 930 °C, only VC and V(CN) precipitates were predicted to dissolve below this temperature in both study-steels, making the VN-steel less effective to grain boundary pinning in comparison to the NbTiV-steel that also contains (Nb, Ti)(CN), Nb(CN) and Ti(CN) precipitates. Only aluminium nitrides (AlN) in the VN-steel have been predicted above 930 °C. This means that grain boundary pinning during austenitisation was to be expected to a greater extent in the NbTiV-steel.

3.7 T_{NR} predictions of the study-steels

Table 3-3 shows the predicted nil-recrystallisation (T_{NR}) temperatures for the two steel grades that were calculated using equations 2.1–2.3 from the literature [61]–[63]. According to the predictions, the NbTiV-steel shows higher T_{NR} temperatures than the VN-steel. From this information, it should be expected that under the same hot rolling conditions the NbTiV-steel should have a finer average ferrite grain size distribution than the VN-steel that has lower predicted T_{NR} temperatures [151].

Table 3-3: T_{NR} predictions for the study-steels based on models from the literature [61]–[63].

Steel	T_{NR} predictions [°C]		
	Eqn 2.1	**Eqn 2.2**	**Boratto Eqn 2.3**
VN	767	849	864
NbTiV	1055	954	967

CHAPTER 4 EXPERIMENTAL RESULTS

4.1 Introduction

The main focus of this study was to investigate the response of the study-steels to the applied heat treatment cycles and also analyse their subsequent mechanical properties. And thereby, finally determine the optimum cycle with the best combination of tensile and impact mechanical properties, while at the same time minimizing and/or eliminating the coarse and banded microstructure of the as-hot rolled microalloyed steels. The same procedures during experimentation were applied on both steel grades and hence results were acquired for both grades of steel. Thus, this chapter compiles and presents chronologically all the experimental results obtained in this study. The results on the two microalloyed steel grades (VN and NbTiV-steel) are presented under the subsections as follows: Thermo-Calc prediction results on determination of critical temperatures and precipitation behaviour; heat treatment simulation schedules; microstructural characterisation before and after heat treatment simulations; the influence of heat treatment on mechanical properties; and fractography.

4.2 Dilatometric analysis

Dilatometric experiments using the Bähr dilatometer were conducted for both study-steels to determine the transformation temperatures that were used in the design of the heat treatment simulations. The heating and cooling dilatation curves were generated, analysed and solid-state phase transformation temperatures were determined as shown in Figure 4.1. The cooling rates used were those of the simulated air cooling for the 16 mm VN-steel and 30 mm NbTiV-steel plates that were earlier presented in Figure 3.2*(ii)*. With natural air cooling, the cooling rate is highly dependent on the thickness of the steel plates, hence, the respective cooling rates used in the simulations. The transformation–start and finish temperatures were determined from the flexions in the heating and the cooling slopes of the relative change in length–temperature plot. These temperatures have also been shown in Figure 4.1 and summarised in Table 4-1.

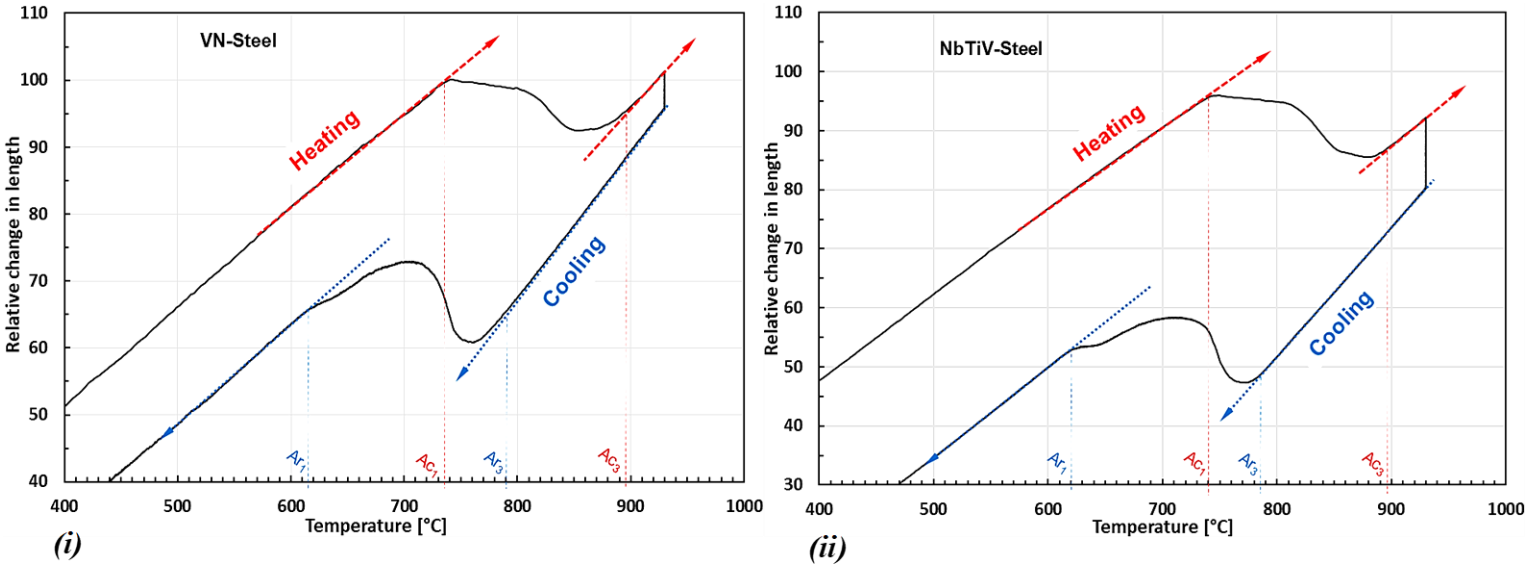


Figure 4.1: Dilatation curves for **(i)** VN-steel (16 mm) and **(ii)** NbTiV-steel (30 mm) indicating the transformation temperatures. Heating and air-cooling rates in *Figure 3.2(i)* were used.

Table 4-1: A summary of the critical transformation temperatures for the VN and NbTiV steels.

STEEL TYPE	TEMPERATURE [°C]					
	Ae_3	Ac_3	Ac_1	Ar_3	Ar_1	Ac_3+30
VN	829	895	735	790	615	925
NbTiV	839	896	740	785	620	926

NB: *The Ae_3 temperature is that which was predicted from Thermo-Calc. The rest is determined from dilatation curves.*

Figure 4.2 shows the dilatation curve results of the study-steels that were generated by the Bähr dilatometer after the NHT and the IAHT. These results can be used to illustrate the influence of the intercritical annealing temperature on the relative volume fraction of austenite during heating of the study-steels. It can be observed from Figure 4.2 that an increase in the intercritical annealing temperature along the x-axis consequently raises the austenite volume fraction. This can be shown by the lever rule calculation ({A–B}/{A–C}) along the tie line connecting points A, B and C. Approximately, the calculated relative austenite volume fractions for the NbTiV-steel (according to Figure 4.2 *(i)*) as the temperatures increase from 775 °C, 800 °C, to 825 °C (depicted with the dotted red arrows) are 0.15, 0.30 and 0.46 respectively. Therefore, this implies that the effective carbon content in austenite during intercritical annealing decreases with increasing intercritical annealing temperature.

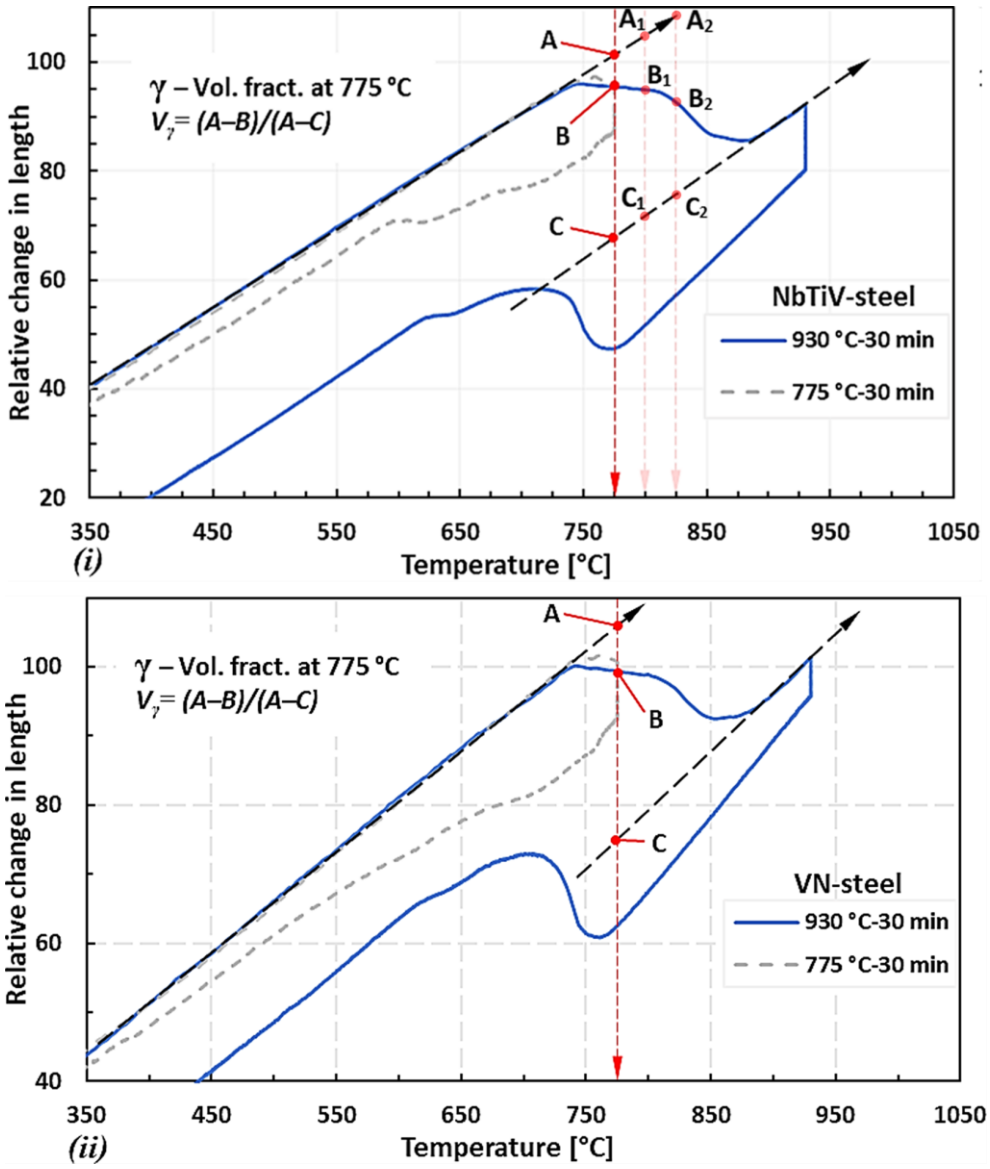


Figure 4.2: Dilatometric analysis of the influence of intercritical annealing temperature on the relative austenite volume fraction (V_γ). Full austenitisation dilatation curve (solid) and intercritical austenitisation (dotted curves). **(i)** NbTiV-steel, the dotted red lines indicate the system at 775 °C, 800 °C and 825 °C. **(ii)** VN-steel, the dotted red line indicates the system at 775 °C. A heating rate of 31 °C/min.

4.3 Microstructural characterisation of the as-hot rolled material

The initial microstructural characterisation was done on the study-steels in their industrial as-hot rolled conditions. This section has characterised the microstructural banding of the microalloyed steels in the current study. Apart from the qualitative characterisation of banding, a quantitative characterisation that involved through-thickness grain size measurements and evaluation of the degree of banding is being presented in this section.

4.3.1 Ferrite grain size and degree of banding measurements

Figure 4.3 shows optical micrographs for the NbTiV-steel (a–c) on the left and the VN-steel (d–f) on the right in the as-hot rolled conditions. The microstructure of these hot-rolled hypoeutectoid steels typically comprises ferrite (light phase) and pearlite (dark phase) that have been aligned in alternating layers, in the rolling direction as shown in Figure 4.3. As expected, the average ferrite grain size of the as-hot rolled material was generally finer in the 16 mm thick VN-steel than in the 30 mm thick NbTiV-steel. This was attributed to the fact that the VN-steel was subjected to a higher deformation in 20 passes (93.3% reduction) than the NbTiV-steel which underwent 18 passes with a total reduction of 87.5%. Moreover, this also implies that the exit temperature of the NbTiV-steel was higher than that of the VN-steel.

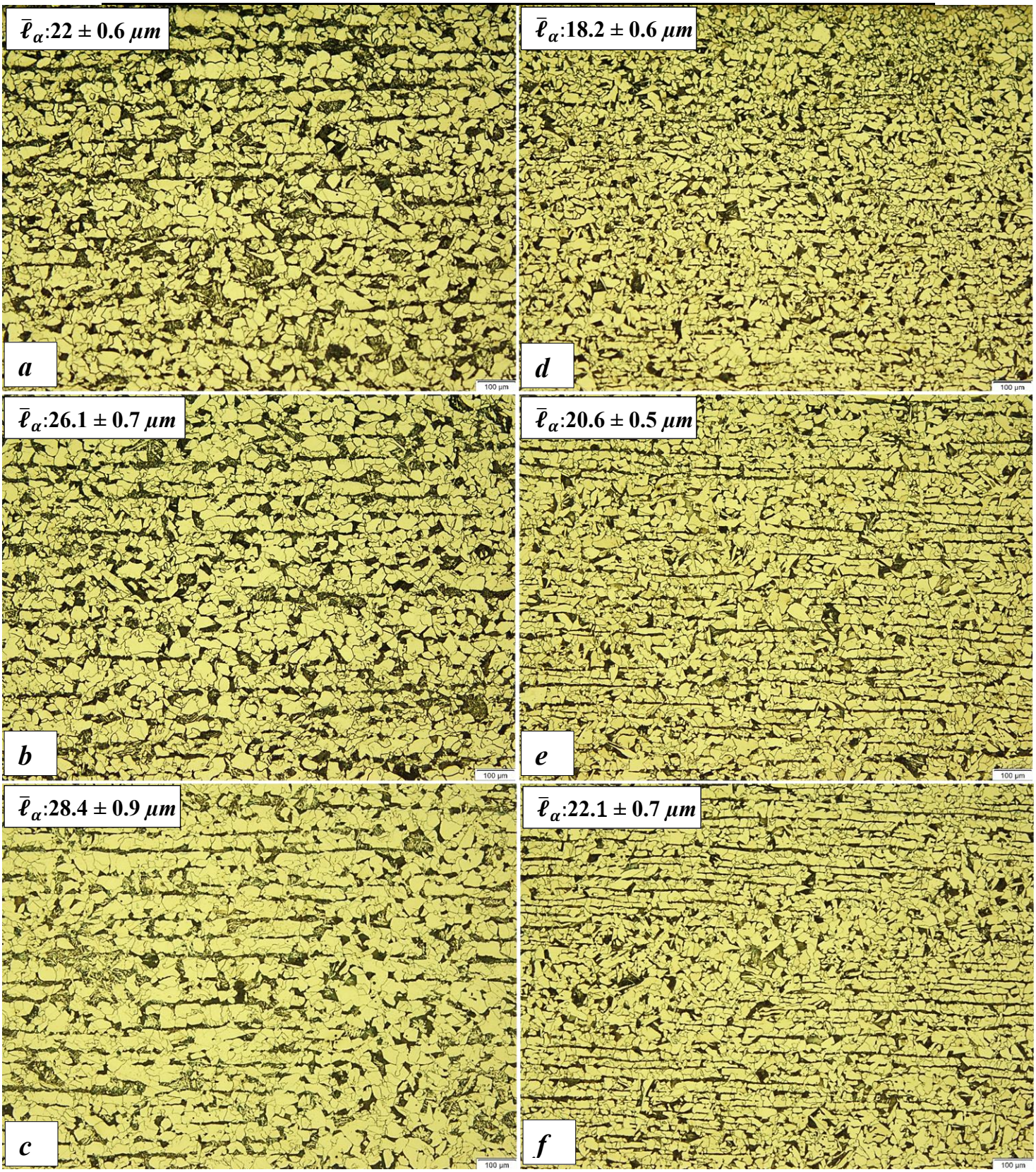


Figure 4.3: Showing optical micrographs for the 30 mm plate NbTiV-steel (left) starting with **(a)** Near-surface (NS), **(b)** Quarter-thickness (QT), **(c)** Mid-thickness (MT); and 16 mm plate VN-steel (right) starting with **(d)** NS, **(e)** QT and **(f)** MT. Etched with 2% Nital. Scale bar, 100 µm (x100).

Grain size measurements for both steel samples were taken from near-surface, quarter-thickness and mid-thickness. The results show a ferrite grain size gradient from the surface to the centre. This has been plotted in Figure 4.4 as *mean ferrite grain size versus plate depth* from the surface to the centre. The volume fractions of ferrite were also determined through the manual point count and the threshold method in *ImageJ*® (Appendix A.6, section 8.6). See Appendix A.5 for the ferrite grain size Excel templates that were used for the study-steels.

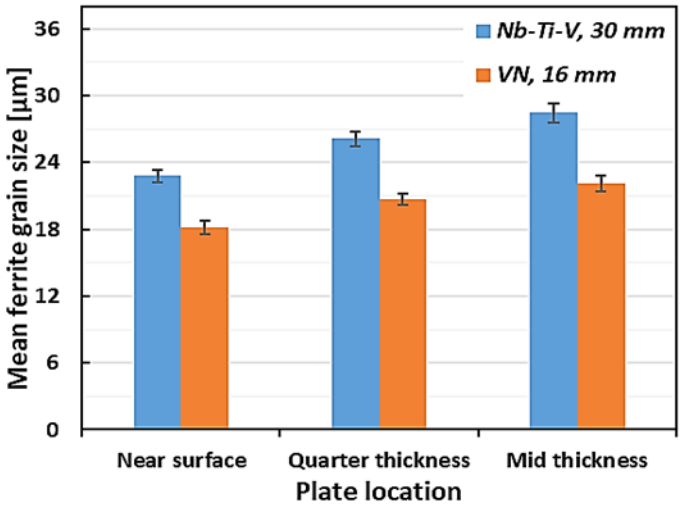


Figure 4.4: A plot of the average ferrite grain size vs depth from the surface to the centre of the 30 mm thick NbTiV and 16 mm thick VN-steel plates.

Both steel samples were banded in the hot-rolled condition and the extent of microstructural banding was quantified. Table 4-2 gives a summary of the results on the degree of banding in the study-steels. The average anisotropy index (AI) values for the pearlite bands in both steel samples were found to be greater than 1. According to ASTM E 1268, this confirms that the steels were banded and oriented in the rolling direction, with a higher degree of microstructural banding (16% greater) in the VN-steel than in the NbTiV-steel ($AI_{VN} > AI_{NbTiV}$). It can also be seen from the table that the $SB_{\perp}$ and $\lambda_{\perp}$ quantities for the pearlite bands in the VN-steel are smaller than those of the NbTiV-steel. This implies that the pearlite bands in the VN-steel sample were more closely spaced than in the NbTiV-steel since the $SB_{\perp}$ and $\lambda_{\perp}$ quantities give a measure of how far apart the pearlite bands are, see Figure 3.1

Table 4-2: A summary on the degree of microstructural banding measurements in the study-steels. See Appendix A.1 for definitions of parameters in the table

Parameter	NbTiV-Steel				VN-Steel			
	Near Surface	**Quarter-Thick.**	**Mid-Thick.**	**Mean Values**	**Near Surface**	**Quarter-Thick.**	**Mid-Thick.**	**MEAN Values**
Mean, $\bar{X}$ (No./μm)	17.1	15.6	15.2	16	22.7	23.8	23.8	23.4
St.Dev.	2.57	2.92	1.71	2.4	2.22	1.66	3.42	2.43
%Relative Acc.	11	14	9	11.3	7.4	5	11	7.83
95% Conf. Int., ±	1.94	2.2	1.29	1.81	1.68	1.25	2.58	1.81
Aniso. Ind. (AI)	1.07	1.21	1.1	**1.13**	1.01	1.35	1.56	**1.31**
$SB_{\perp}$, μm	69.3	71.5	77	**72.6**	53.7	44.8	42.2	**46.9**
$\lambda_{\perp}$, μm	46.4	47.2	53.9	**49.2**	36.5	27.2	27.4	**30.4**
($SB_{\perp}$ - $\lambda_{\perp}$), μm	22.9	24.3	23.1	**23.4**	17.2	17.5	14.8	**16.5**

4.4 Influence of austenitising temperature on PAGS and banding

The evolution of the prior austenite grains was also studied, and the influence of austenitisation temperature on the PAG structure and retention of microstructural banding of the studied steels are presented in this subsection. Both steel samples were austenitised at temperatures between 965 and 1050 °C for two hours. Figure 4.5 *a & b* depicts some selected optical micrographs of the PAGs for the NbTiV-steel, *c & d* for the VN-steel samples that were austenitised at 1005 °C and 1050 °C for two hours and quenched in still water, and then followed by tempering at 496 °C for 33 hours. PAGBs were revealed by etching with Marshall's reagent as described in section 3.3.1. The mean grain sizes and the standard deviations have also been included in the micrographs. Figure 4.6 shows a graphical plot of the average PAGS against austenitisation temperature for both steel samples. For all austenitisation temperatures, as expected, the NbTiV-steel exhibited the finer PAGS as compared to the VN-steel.

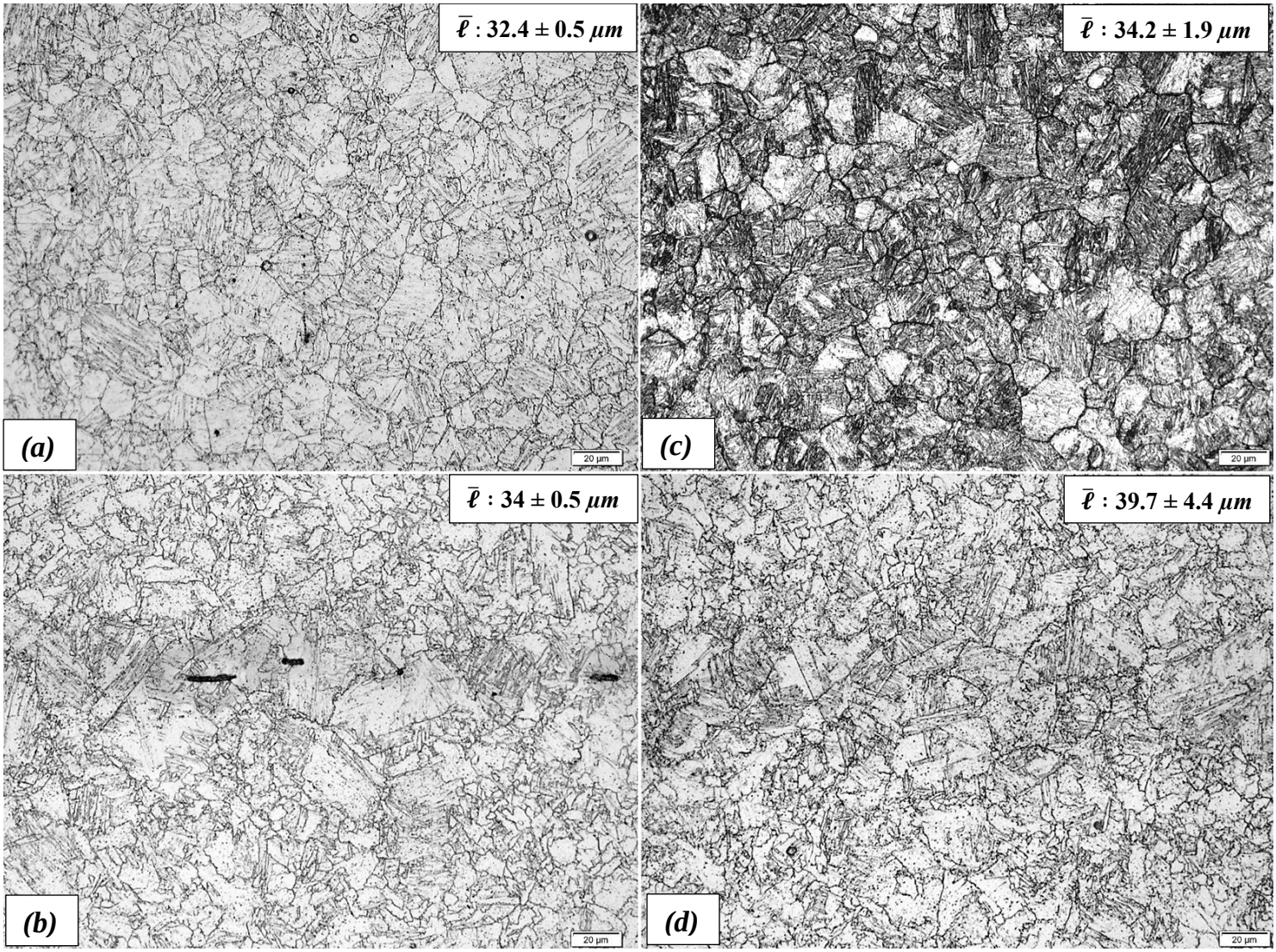


Figure 4.5: Optical images of microstructures that were austenitised for 2hrs, water-quenched followed by tempering at 496 ℃ for 33hrs. Only *(c)* was not tempered. NbTiV-steel (left), **(a)** austenitised at 1005 °C, **(b)** at 1050 °C; and VN-steel (right), **(c)** austenitised at 1005 °C (untempered), **(d)** at 1050 °C. Etched with Marshall's reagent + 2 drops of HF. The scale bar is 20 μm.

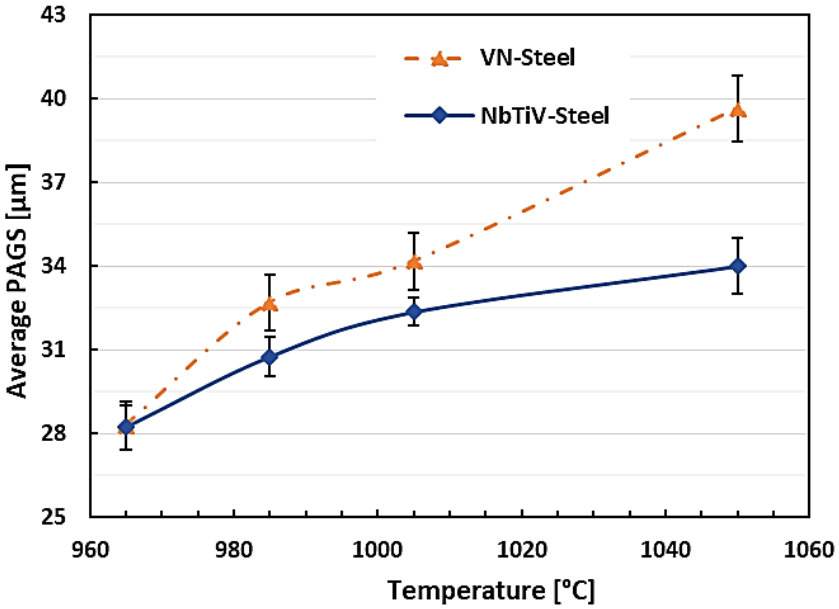


Figure 4.6: A plot showing the influence of austenitisation temperature on the average prior austenite grain size (PAGS) of the NbTiV and VN-steels.

On the retention of banding at austenitisation temperature, Figure 4.7 shows optical micrographs of NbTiV *(b)* and VN *(d)* that were taken at the mid-thickness (also see Figure 4.5 *b*). Both of the steel samples showed some retention (marked with the red circle) of the banding with an evident band of coarse grains which still manifests as a centre-line and some oriented particles. Through-thickness grain size measurements were also done to investigate the retention of the grain size gradient that was observed in the as-hot rolled microstructures. Figure 4.8 shows graphical plots for both steel samples. The through-thickness grain size distribution was almost uniform in both steel samples, with just a coarse band of grains only appearing at the mid-thickness.

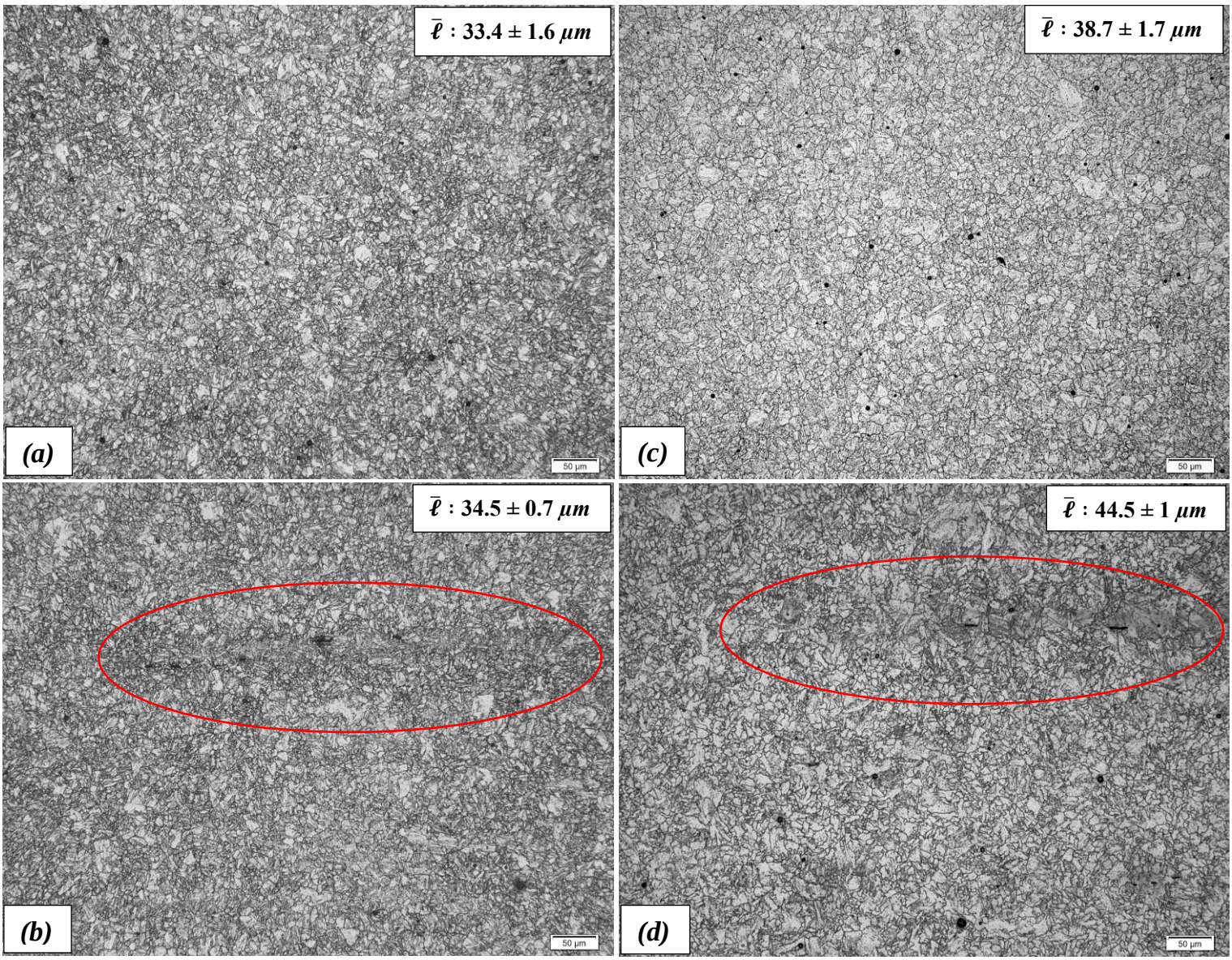


Figure 4.7: Showing optical images of microstructures that were austenitised at 1050 °C for 2hrs, water-quenched, then tempered at 496 °C for 33hrs. **NbTiV-steel** (left), **(a)** near-surface **(b)** mid-thickness; and **VN-steel** (right), **(c)** near-surface, **(d)** mid-thickness. Red circle showing banding-retention region at the mid-thickness in both samples. Etchant: Marshall's reagent + 2 drops of HF. The scale bar is, 50 μm.

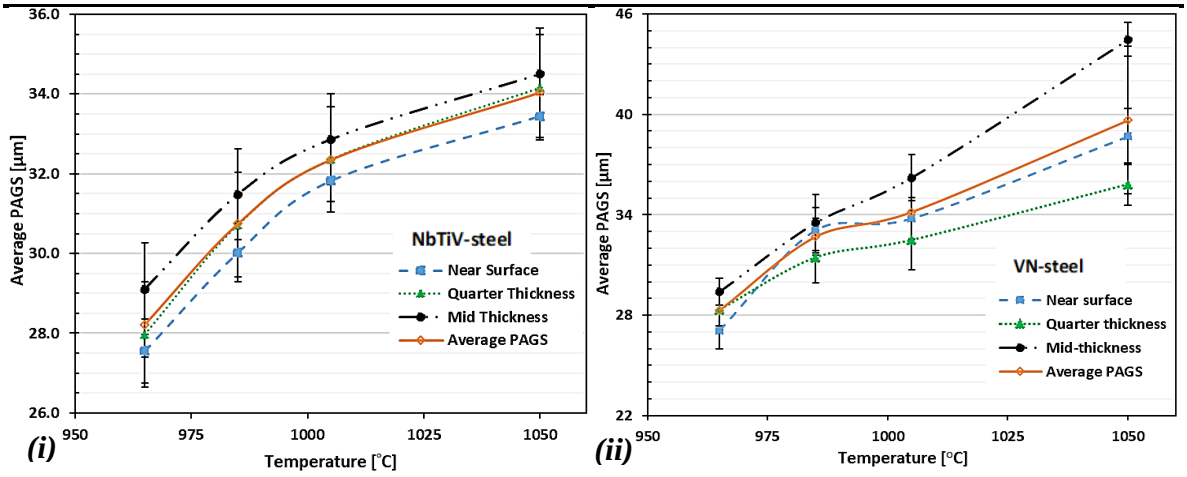


Figure 4.8: Through-thickness average PAGS vs austenitising temperature for, **(i)** NbTiV and **(ii)** VN.

4.5 Impact of applied heat treatments on microstructural evolution

The results of the influence of different heat-treatment schedules on the microstructural evolution vis-à-vis banding are presented in this section. The heat treatment cycles that were employed were the normalising heat treatment (NHT), double austenitisation heat treatment (DAHT) and intercritical annealing heat treatment (IAHT) of the NbTiV and VN-steel, and the mechanical properties are presented in this section.

Firstly, other intercritical austenitisation temperatures for the DAHT (as pointed out in section 3.4.2) were also considered to select the optimum route based on the microstructural evolution. The other two temperatures in the second cycle of the DAHT (apart from the 775 °C) were 740 °C and 810 °C. The resulting microstructures are shown in Figure 4.9. Banding was still apparent in the microstructures of both steel samples, with the more severe case in the DAHT–740 °C. The DAHT–775 °C produced the optimum microstructure in terms of the ferrite-pearlite homogenisation. Another thing worth noting in the microstructures is that the DAHT–810 °C produced the apparent finest ferrite grain size distribution. This could be attributed to the magnitude of undercooling in this cycle. Again, the VN-steel microstructure under these conditions was once more banded than that of the NbTiV-steel. The same temperatures namely 740 and 810 °C, were used for the IAHT. The microstructures were analysed to identify the optimum IAHT for reduced banding and grain size. Figure 4.10 shows the microstructures after the IAHT. In general, the ferrite-pearlite banding was still retained with intercritical annealing temperatures of 740 and 810 °C in both samples with an exception in the NbTiV-steel grade at the intercritical annealing temperatures of 775 and 810 °C. At the same annealing temperature, the VN-steel still showed high retention in banding relative to that of the NbTiV-steel.

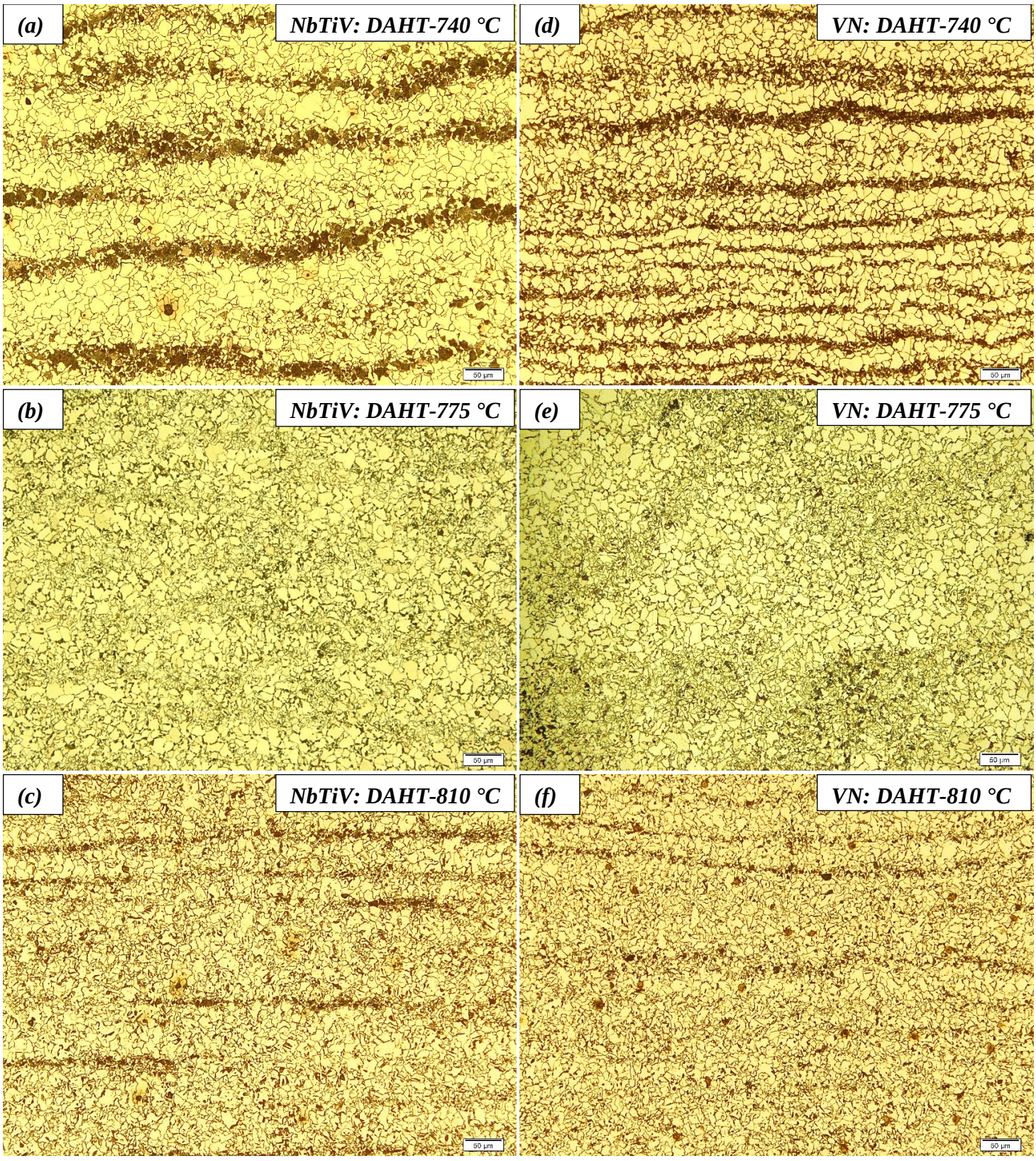


Figure 4.9: Optical micrographs of the NbTiV (left) and VN-steel (right) samples after the DAHT at intercritical temperatures of 740, 775 and 810 °C in the 2nd cycle as indicated in the inserts. Illustrating how the cycles had little to almost no impact on the ferrite-pearlite banding except at 775 °C. The scale bar is 50 µm. 2% Nital etch.

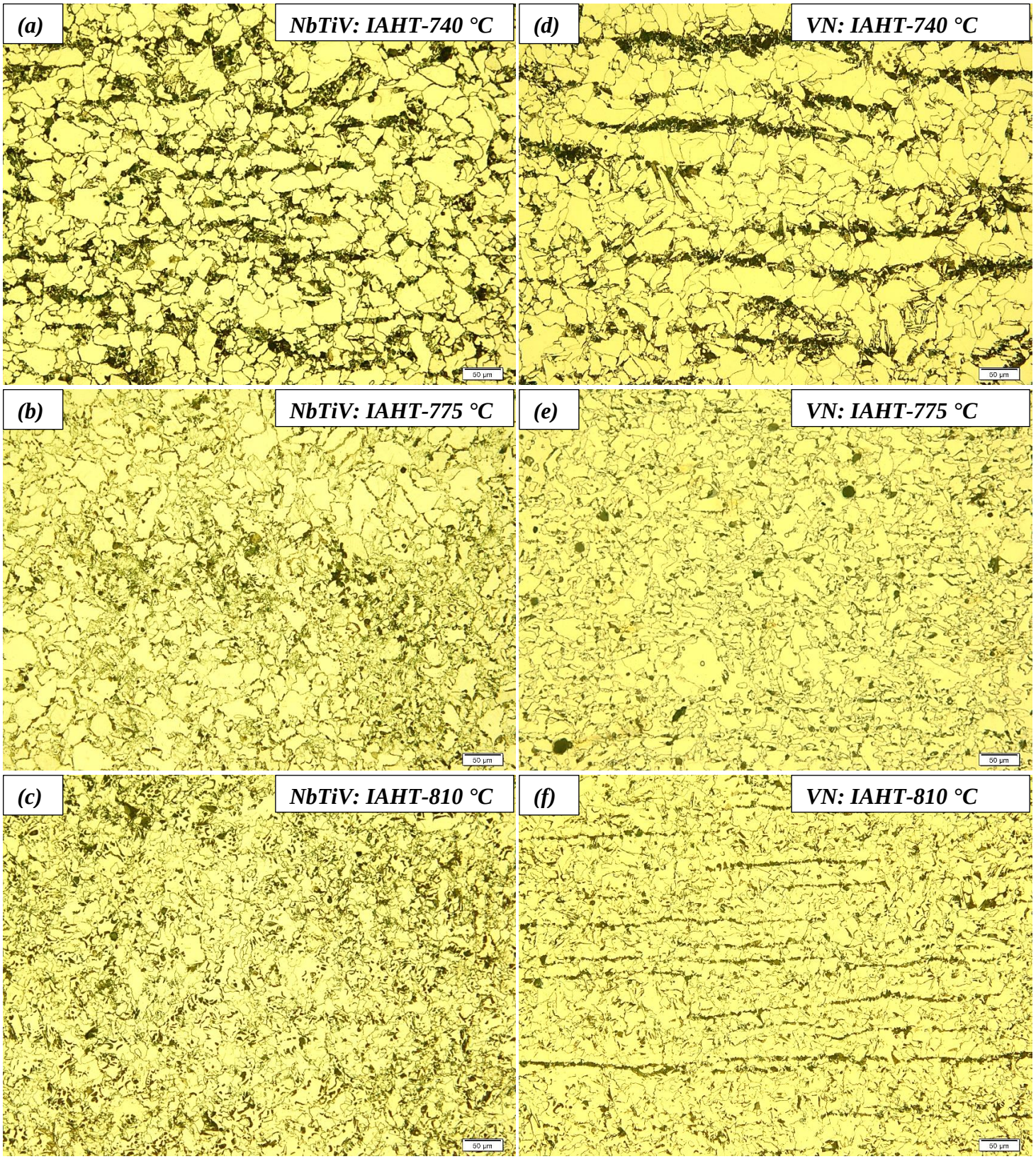


Figure 4.10: Optical micrographs of the NbTiV (left) and VN-steel (right) samples after the IAHT at 740, 775, and 810 °C as indicated in the inserts. Illustrating how the cycles had no major impact on the ferrite-pearlite banding, except at 775 °C for both steel samples and 810 °C for NbTiV. The scale bar is 50 µm. 2% Nital.

Based on the results from the microstructural optimisation exercise shown in this section, the heat treatment routes with the intercritical annealing temperature of 775 °C were selected as the most successful heat treatment remove banding. Optical micrographs for the heat treated NbTiV and VN-steels are shown in Figure 4.11 and Figure 4.12 respectively. After each of the heat treatment cycles, the final transformation products in both steel samples were ferrite and pearlite. The general response of the study-steels to each of the heat treatments was similar. Ferrite-pearlite banding was still present after the NHT in both steel grades, but marginally more severe in the VN-steel. The DAHT had a significant impact on the microstructural evolution of both steel specimens; the ferrite-pearlite banding was no longer visible in the NbTiV-steel, and very faint in the VN-steel. In both study-steels, the IAHT also removed the banding, however, it exhibited a bimodal (see Figure 4.13) ferrite grain structure in both alloys, which was also coarse. Finally, it should also be noted that, in general, the NbTiV-steel had a finer mean ferrite grain size than the VN-steel after heat treatment (thermal cycle–to–thermal cycle comparison). Some aspects worth noting from each of the heat treatments have been summarised in Table 4-3.

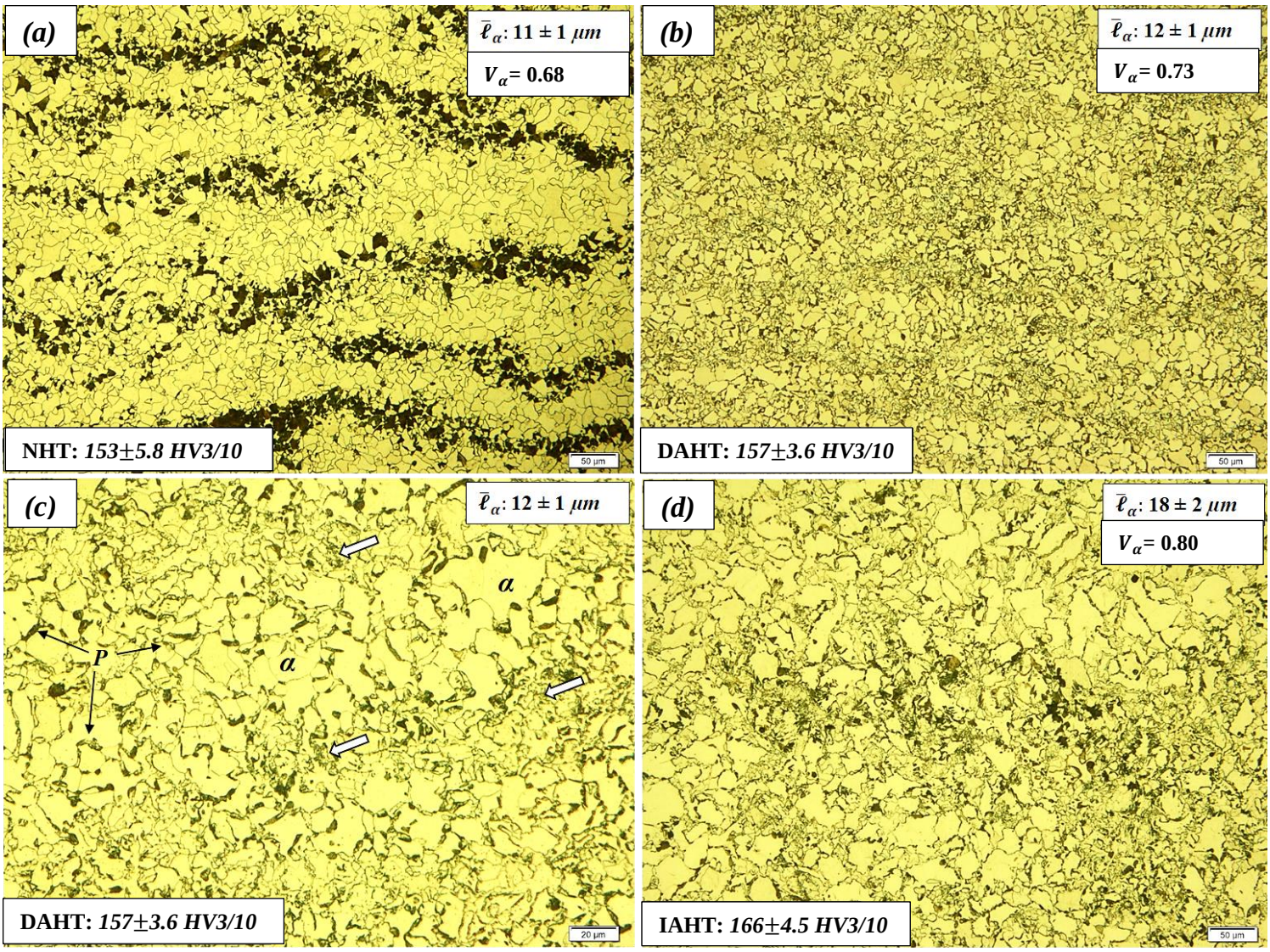


Figure 4.11: Optical micrographs of the NbTiV-steel samples showing respective ferrite grain sizes, volume fractions and macro-Vickers hardnesses. **(a)** NHT; **(b)** DAHT; **(c)** DAHT at higher magnification, depicting fine pearlite colonies nucleating at prior austenite grain corners and boundaries (black arrows). Also, note the refined pearlite that nucleated in the carbon-rich regions (white arrows); **(d)** IAHT. All scale bars are at 50 μm, except that in ***(c)*** which is 20 μm. 2% Nital etch.

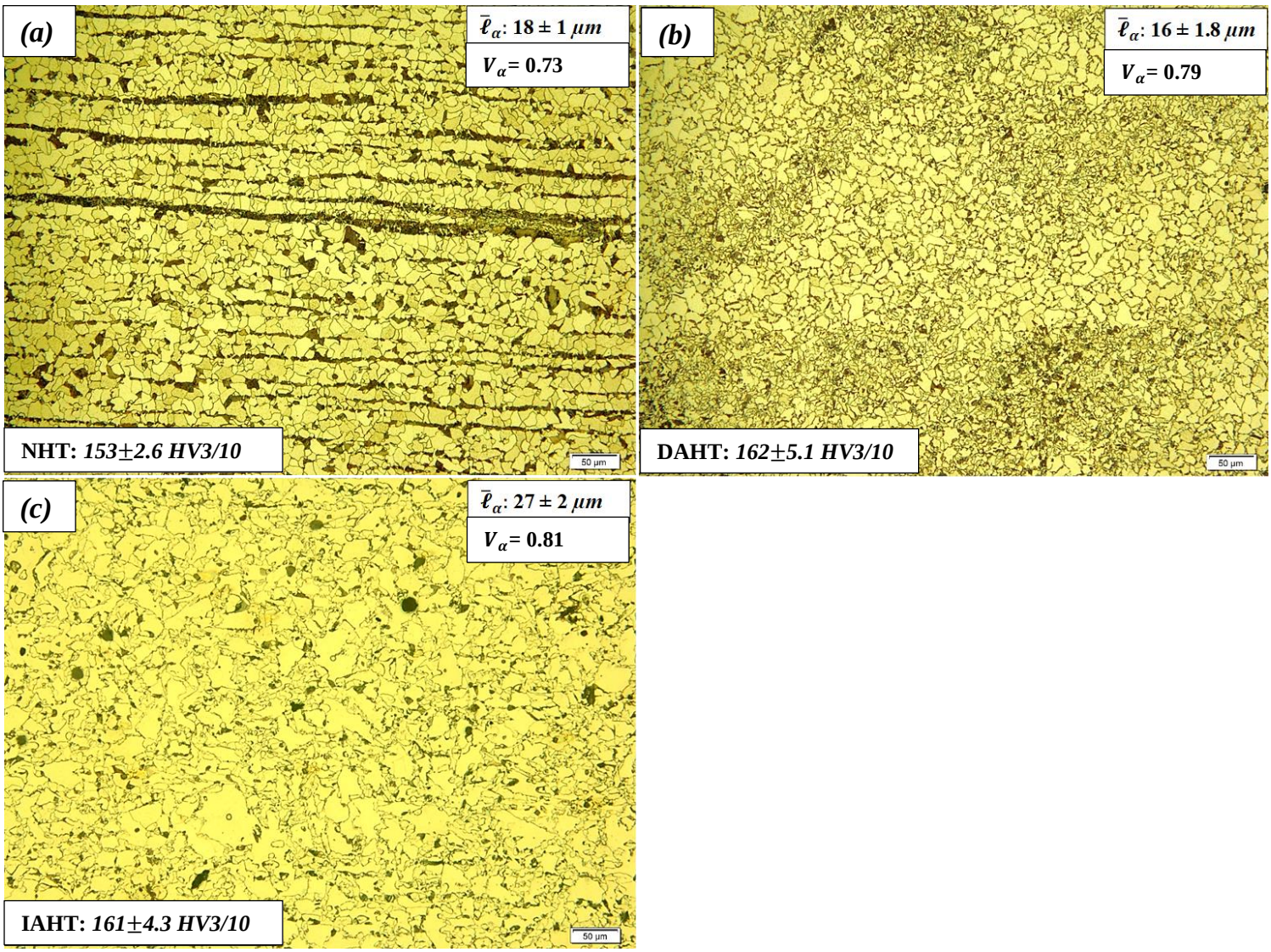


Figure 4.12: Optical micrographs of the VN-steel samples showing respective ferrite grain sizes, volume fractions and macro-Vickers hardnesses. **(a)** NHT (austenitised at 930 °C); **(b)** DAHT (annealed at 930 & 775 °C); **(c)** IAHT (annealed at 775 °C). All scale bars at 50 µm. 2% Nital etch.

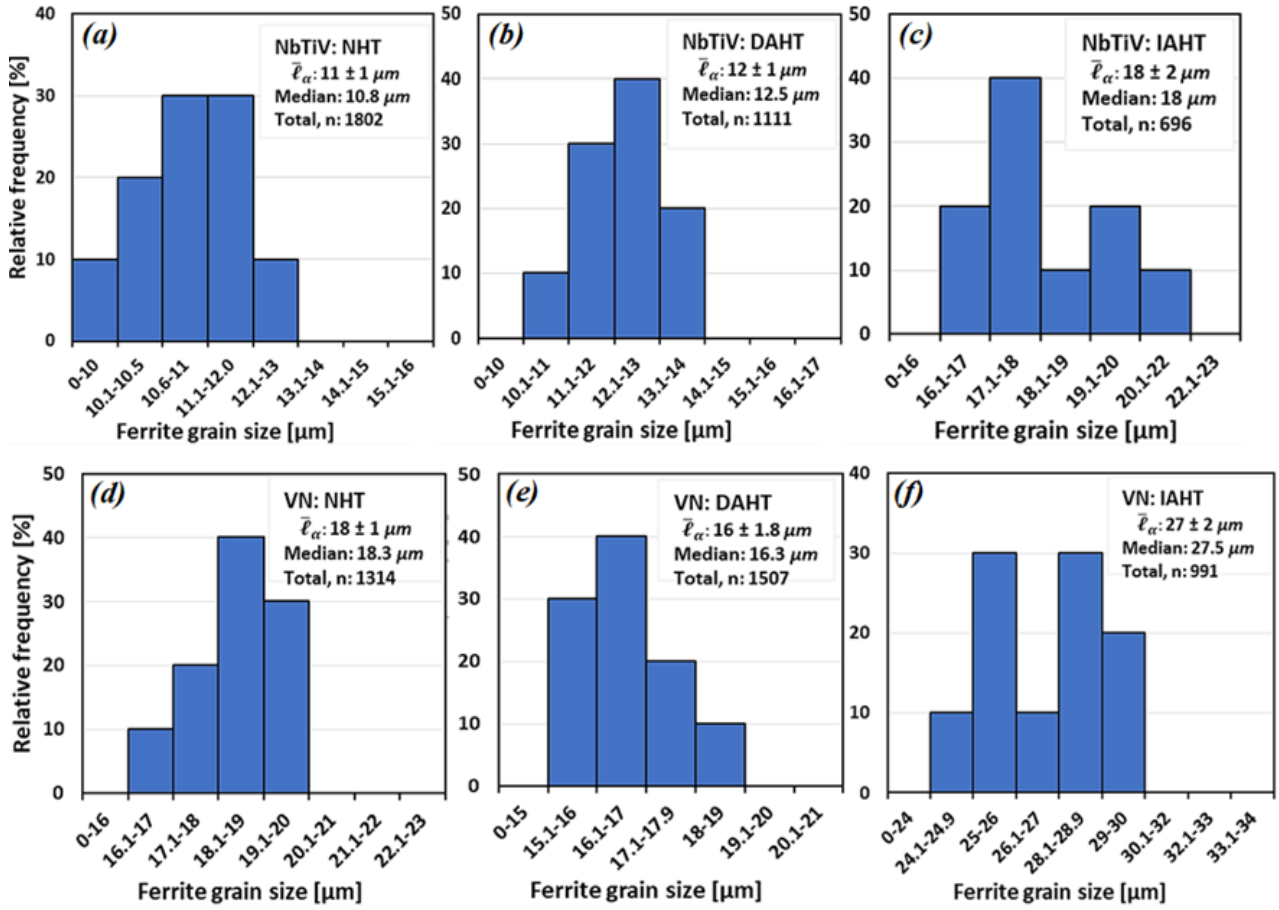


Figure 4.13: Ferrite grain size distribution of NbTiV (top, *a–c*) and VN-steel (bottom, *d–f*) heat treated microstructures. ***a), b), d)*** and ***e)*** Showing a normal distribution after the NHT and DAHT. ***c)*** and ***f)*** showing a bimodal distribution after the INHT.

Table 4-3: A summary of the influence of respective heat treatments on the microstructural evolution of the study-steels.

	NbTiV-Steel				VN-Steel			
	Banding	**Ferrite grain refinement**	**Pearlite refinement**	**Comments**	**Banding**	**Ferrite grain refinement**	**Pearlite refinement**	**Comments**
NHT	Yes	Yes	Yes	- Wavy & discontinuous but **fine** pearlite (mildly banded)	Yes	Yes	Yes	- Continuous & narrow but **fine** pearlite (still heavily banded)
DAHT	No	Yes	Yes	- Homogeneous and **finest** pearlite	Mild	Yes	Yes	- Pearlite is not entirely homogeneous, but still **finest**. - Faint, broad, band of refined pearlite.
IAHT	No	No	Yes	- Degenerate and **finer** pearlite. - Coarse and **bimodal** ferrite grain size	No	No	Yes	- Degenerate and **finer** pearlite. - Coarse and **bimodal** ferrite grain size

Further microstructural analysis through SEM at very high magnifications was performed on those samples that involved an intercritical annealing cycle to verify the availability of other austenite decomposition phases, such as bainite. It is well known that intercritical annealing increases the austenite hardenability, hence, the decision to verify the availability of other phases. Therefore, the DAHT and IAHT samples were selected for SEM analysis. SEM was merely used for qualitative analysis of the microstructures in this task. The SEM micrographs in Figure 4.14 confirm that the microstructure was only comprised of ferrite and refined pearlite colonies.

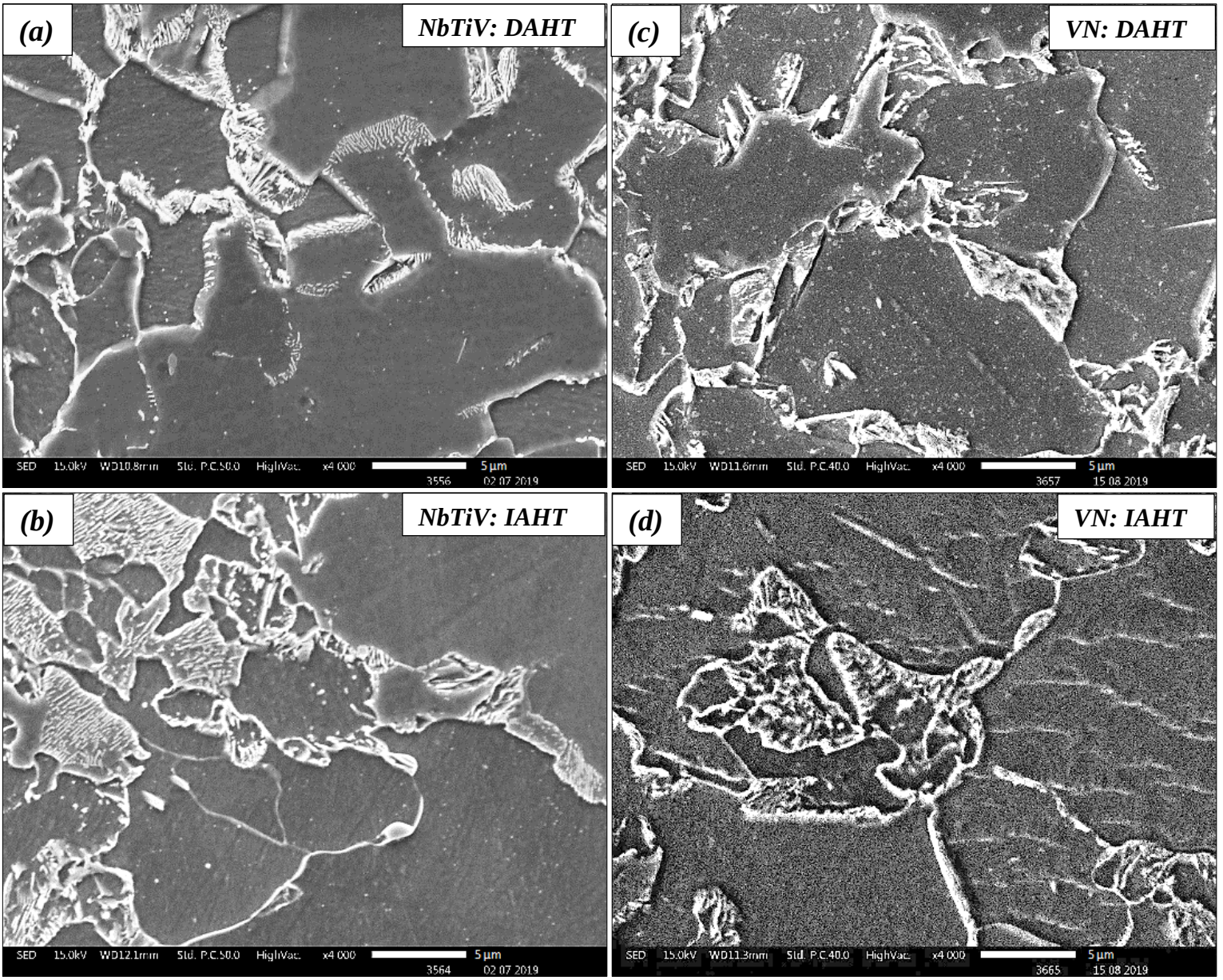


Figure 4.14: SEM secondary images of the NbTiV (left) and VN-steel (right) samples after the DAHT and IAHT as indicated in the inserts. Illustrating the fine pearlite colonies (light phase) that nucleated at ferrite (dark matrix) grain boundaries and grain corners. The scale bar is 5 µm. 2% Nital etch.

The refined pearlite colonies are comprised of degenerate pearlite; see the red circled regions in Figure 4.15. Degenerate pearlite is morphologically different from the usual lamellar kind of pearlite. This pearlite has discontinuous lamella as can be observed in Figure 4.15. Another important microstructural feature that was very prominent after the IAHT was the precipitate free (PF) epitaxial ferrite grains. Figure 4.15 shows the PF epitaxial ferrite grains that have formed on other ferrite interfaces (retained ferrite) in a mechanism that uses the retained ferrite as a substrate (to be discussed in section 5.2.3).

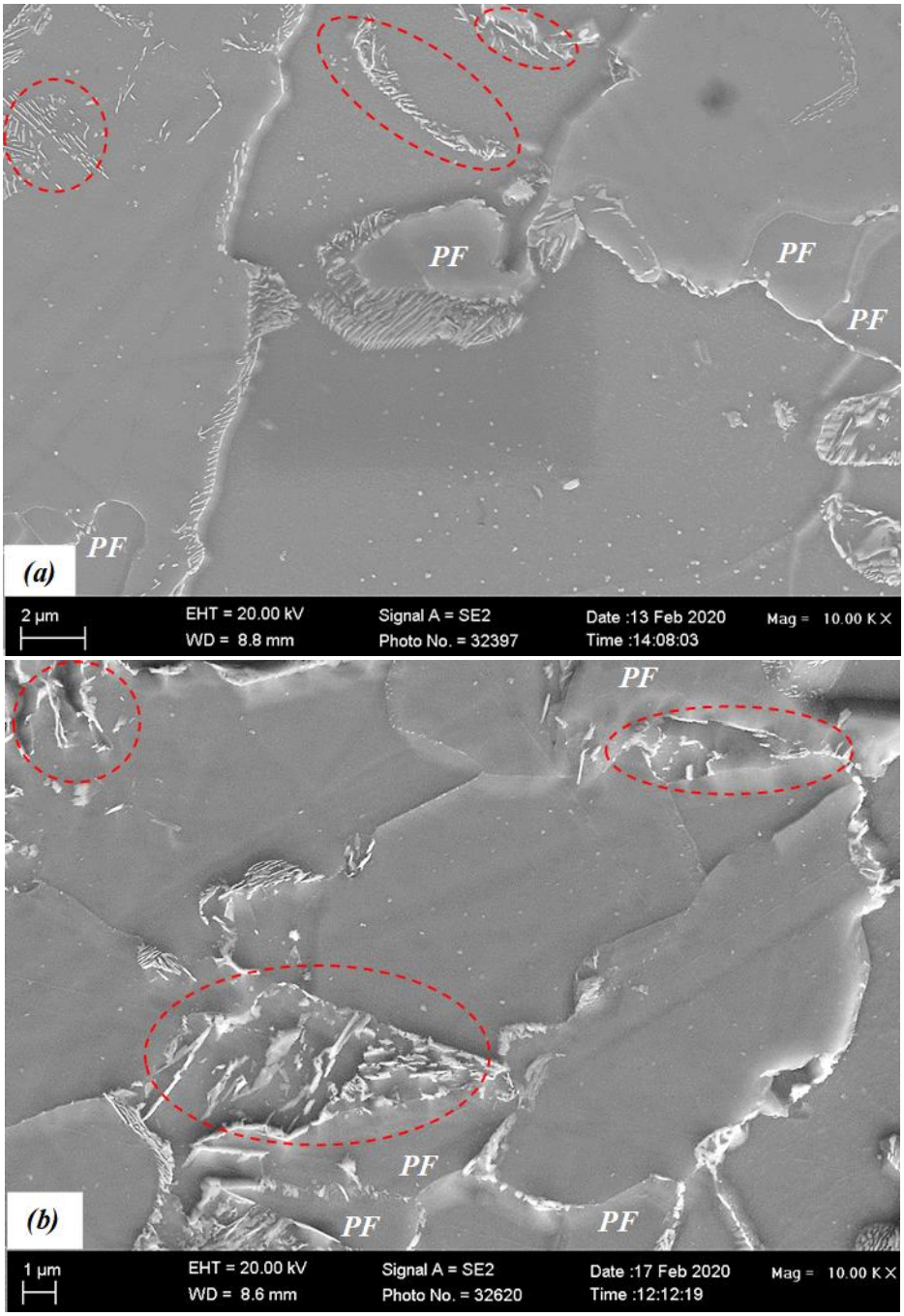


Figure 4.15: SEM secondary images showing precipitate free (PF) epitaxial ferrite grains and degenerate pearlite in both steel samples after the IAHT. **(a)** NbTiV-steel, **(b)** VN-steel. 2% Nital etch.

4.6 Impact of applied heat treatments on mechanical properties

4.6.1 Tensile test results

Mechanical tests were conducted to analyse the influence of each heat treatment on the two steel grades and therefore determine the optimum heat treatment for the study-steels. Figure 4.16 shows the engineering stress-strain graphical plots comparing the effect of each heat treatment on the yield strength (R_p), tensile strength (R_m or UTS) and fracture elongation (A_5) within the respective steels. The mechanical properties are noticeably dependent on the applied heat treatment route. The engineering stress-strain curves in both steel grades clearly exhibit the yield point phenomenon, thus, the yield point was easily identified. In the NbTiV-steel, the R_p and R_m fall in the range of 350–404 MPa and 518–543 MPa, respectively, and the A_5 in the range 27–31% for all the types of heat treatments. The NHT produced the highest R_p and A_5 values, while those of the DAHT and IAHT were roughly the same. The IAHT produced the highest R_m and lowest R_p which gave it the smallest R_p/R_m ratio as will be shown later. The DAHT tensile properties are relatively intermediate.

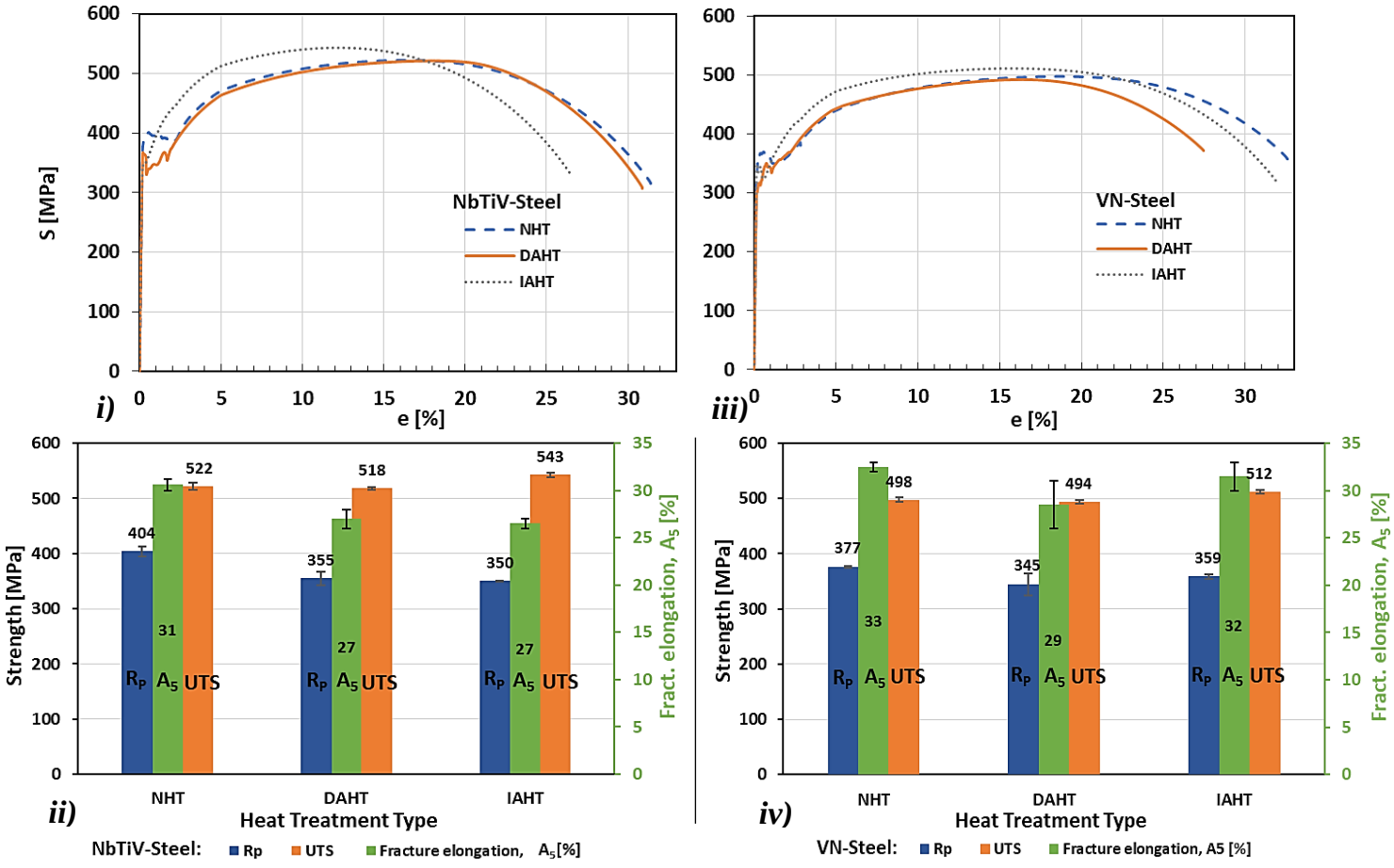


Figure 4.16: Comparison of the NHT, DAHT and IAHT tensile properties of the study-steels. **(i)&(iii)** Engineering stress-strain curves for the NbTiV & VN-steels respectively; **(ii)&(iv)** tensile property comparison with respective heat treatment in NbTiV & VN-steels, respectively.

4.6.2 Work hardening behaviour of the heat-treated samples.

The work hardening behaviour of materials after yielding is linked to the Hollomon strain hardening exponent, n also called the n-value. The n-value of metallic materials gives a measure of how rapidly the strength of a material increases during deformation [152], and therefore represents the work hardening capacity of the material. A high value of n signifies a high work hardening rate of that material, and more deformation before plastic instability sets in [153], see equation 4.1 [154];

$$\frac{d\sigma_1}{d\varepsilon_1} = n\left(\frac{\sigma_1}{\varepsilon_1}\right) \qquad 4.1$$

The left-hand side of equation 4.1 is the work hardening rate at a specific strain ε_1, and specific stress σ_1, (ratio of change in true stress to change in true strain). One way of determining the n–value, is through the Hollomon power-law that involves plotting the log-log of true stress-strain and generating a straight line with a constant slope. However, this is seldom the case in practice where the slope usually varies with strain along the plastic region of the true stress-strain curve [155]. Therefore, the common practice is to plot the log-log of true stress-strain in the region between 10% elongation and the maximum stress (UTS) of the engineering stress-strain curve where n is reasonably stable [156]. Analyses of the work hardening behaviour of the heat-treated study steels were done and the results are shown in Figure 4.17.

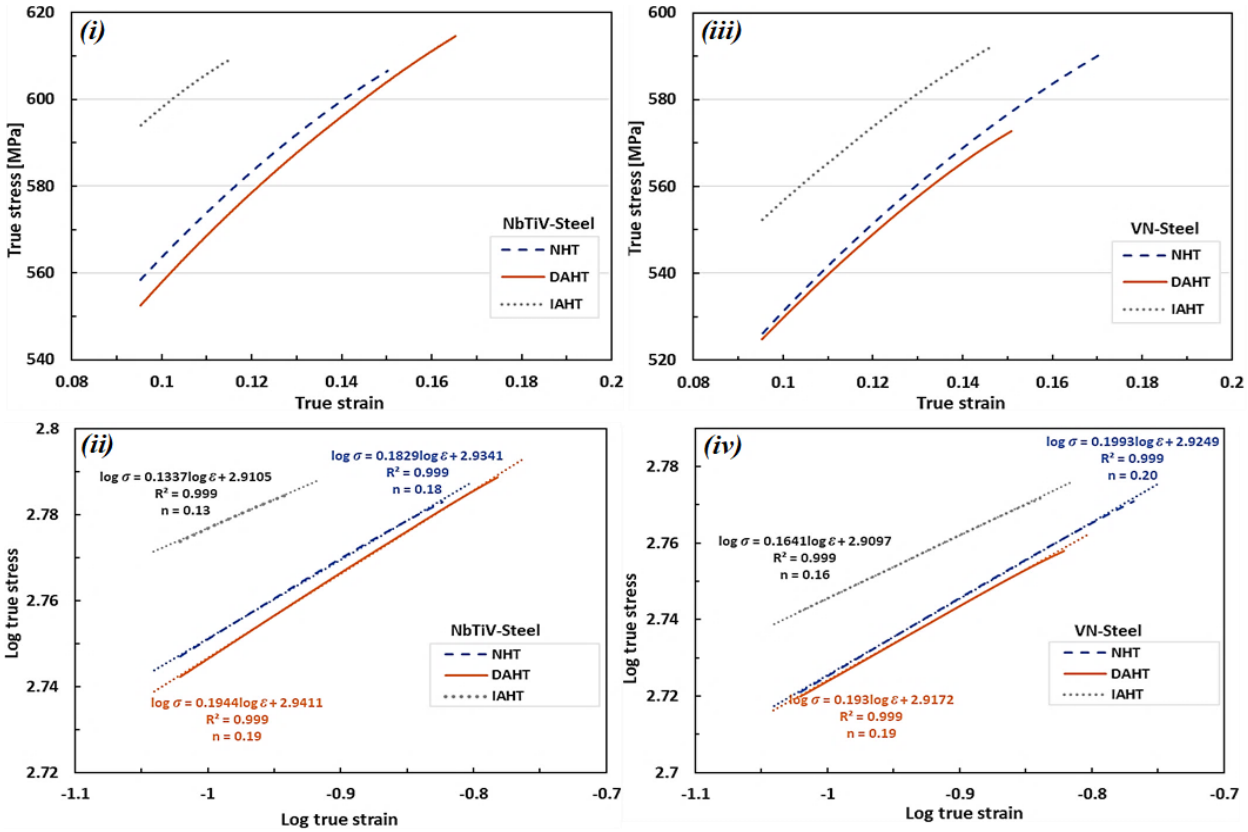


Figure 4.17: Determining the strain hardening exponents of the heat-treated study steels through the Hollomon power-law. (i) & (iii) True stress-strain plots. (ii) & (iv) True stress-strain log-log plots depicting the n-values for the study-steels.

In both steel grades, the n–values after the NHT and DAHT did not differ greatly. However, the difference was observed in the IAHT, which produced consistently lower n-values. This indicates a low work hardening capacity for those samples that were exposed to the IAHT.

4.6.3 Hardness

Figure 4.18 shows the influence of each heat treatment on the hardness of the study-steels and comparatively depicts how each heat treatment affects the steels. The general trend observed in both of the steel grades is that the hardness increased from NHT, DAHT and to IAHT. In other words, the heat treatments that involved intercritical annealing produced higher hardness values.

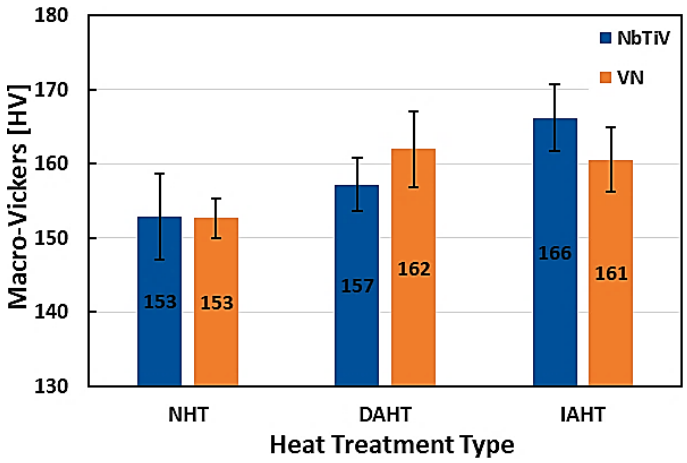


Figure 4.18: Impact of the applied heat treatments on the hardness of NbTiV and VN-steel.

4.6.4 Charpy V-notch impact toughness

The impact of each heat treatment on the impact toughness properties of the study-steels was also investigated. Charpy V-notch (CVN) impact tests were conducted on the two heat treated steel grades. The CVN values of each steel are compared in Figure 4.19. Generally, it can be observed in both steel grades that for the samples that were exposed to the IAHT, their CVN impact curve lies below those of the NHT and DAHT and have higher DBTTs. The DAHT produced the highest upper-shelf energy (USE) and intermediate DBTT in both steel grades. In the NbTiV-steel, the NHT and DAHT exhibited nearly the same impact toughness properties. While in the VN-steel, the DAHT curve was slightly towards lower test temperatures and higher absorbed impact energies than the NHT. Table 4-4 gives a summary of all the mechanical properties of the two steel samples as influenced by the heat treatments that were applied to the steels. And from the table, it can be observed that the VN-steel was generally tougher than the NbTiV-steel.

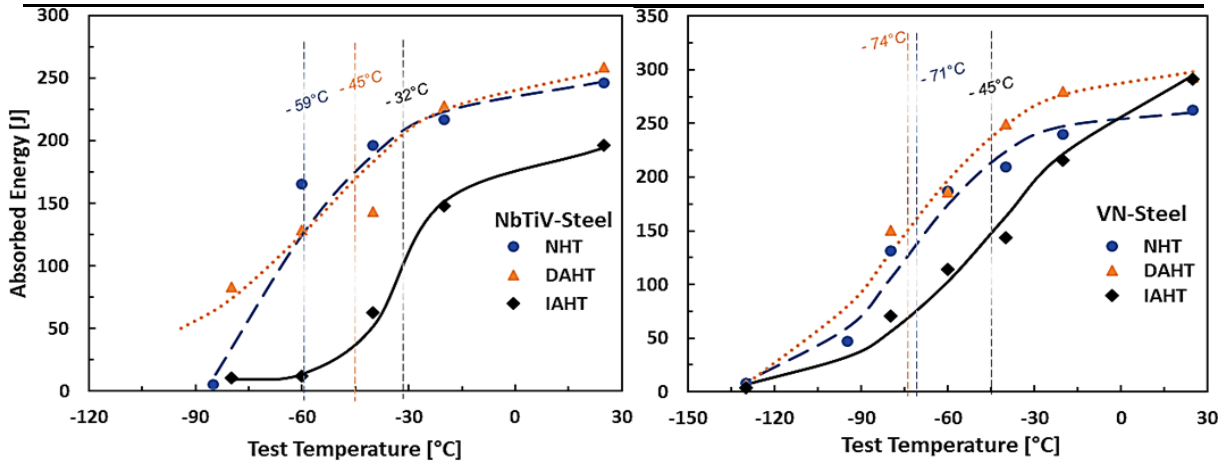


Figure 4.19: Charpy V-notch impact graphs for the NbTiV and VN-steels showing the effect of the heat treatments on the impact toughness properties.

Table 4-4: A summary of the mechanical properties of the heat-treated steel specimens

Steel Type	Heat Treatment	R_p [MPa]	R_m [MPa]	R_p/R_m [ratio]	A_5 [%]	n–values	USE [J]	Energy at – 40°C [J]
NbTiV	NHT	**404**	522	0.77	**31**	0.18	246	**196**
	DAHT	355 ***345***	518 ***450***	0.69 ***0.8$_{max}$***	27 ***18***	0.19	259 ***>27$_{+20}$***	143 ***27$_L$***
	IAHT	350	**543**	0.64	27	0.13	196	63
VN	NHT	**377**	498	0.76	**33**	0.20	263	210
	DAHT	345 ***355***	494 ***470***	0.70 ***0.76$_{max}$***	29 ***22***	0.19	293 ***>54$_{+21}$***	**249** ***34$_L$***
	IAHT	359	**512**	0.70	32	0.16	291	143

NB: *The extra column with figures in red font colour shows the minimum specification requirements according to* [157]–[159].

Figure 4.20 gives a graphical summary of the combination between the CVN impact toughness and strength properties of the two steel grades after the applied respective heat treatments. The red indicators in the graph show the limits beyond which the achieved properties either fail or pass the minimum standard specification requirements for structural applications according to the standards in [157]–[159]. The closed symbols depict the upper shelf energy at 20 °C and the open symbols depict the absorbed impact energy at –40 °C. Although it appears in both steel grades that the DAHT gave a better toughness at room temperature, however, the difference with the NHT is small. The impact toughness at –40 °C for the NbTiV-steel after the IAHT and DAHT was much lower relative to the NHT condition, with significant changes of 68% and 45% respectively, and 15% and 51% for the VN-steel respectively.

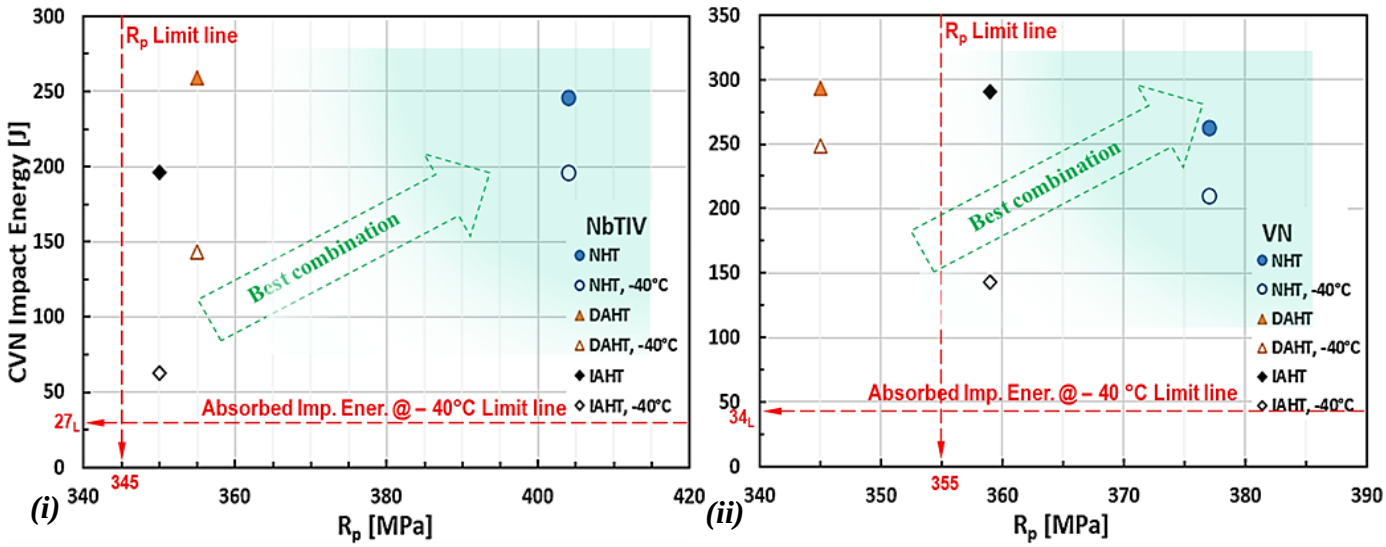


Figure 4.20: Representation of yield strength-impact toughness combination of the heat-treated NbTiV and VN-steels. The closed symbols depict the impact energy at 20 °C, and open symbols absorbed impact energy at –40 °C. The red indicators show minimum specification requirement limits as per [157]–[159]. The highlighted green zone shows the region of the best strength-toughness combination.

4.7 Fractographic analysis of the CVN fracture surfaces

Figure 4.21, Figure 4.22 and Figure 4.23 show SEM fractographs of the fractured surfaces from the CVN impact test after the NHT, DAHT and IAHT, respectively. The fractured surfaces were from a few selected test temperatures –90, –85, –40 and –20 °C to indicate the fracture surface transition.

Looking at the CVN impact curves, the test temperature of –20 °C seems to be the start of the USE region for all the heat treatment types in both steel samples. This can be related to the first group of fractographs in all the figures where dimpled fracture surfaces are apparent, indicating ductile failure. For the NHT and DAHT, the intermediate groups of fractographs (both NbTiV and VN) at the test temperature of –40 °C still exhibit ductile modes of fracture on their surfaces, which can be seen from the dimples and tearing. This is not the case with the IAHT where at –40 °C the surfaces of the VN-steel appear to have undergone a mixed-mode of ductile and cleavage, while the NbTiV-steel is full cleavage. This observation can be validated from the flat facets and tearing ridges that have been pointed out on the fracture surfaces (see Figure 4.23, at –40°C). At the test temperatures of –90, –85, and –80 °C for all heat treatment conditions and in both samples, cleavage fracture is evident on the fracture surfaces from the plane, smooth facets and cleavage cracks (such as those shown in Figure 4.21, at –85 and 90 °C).

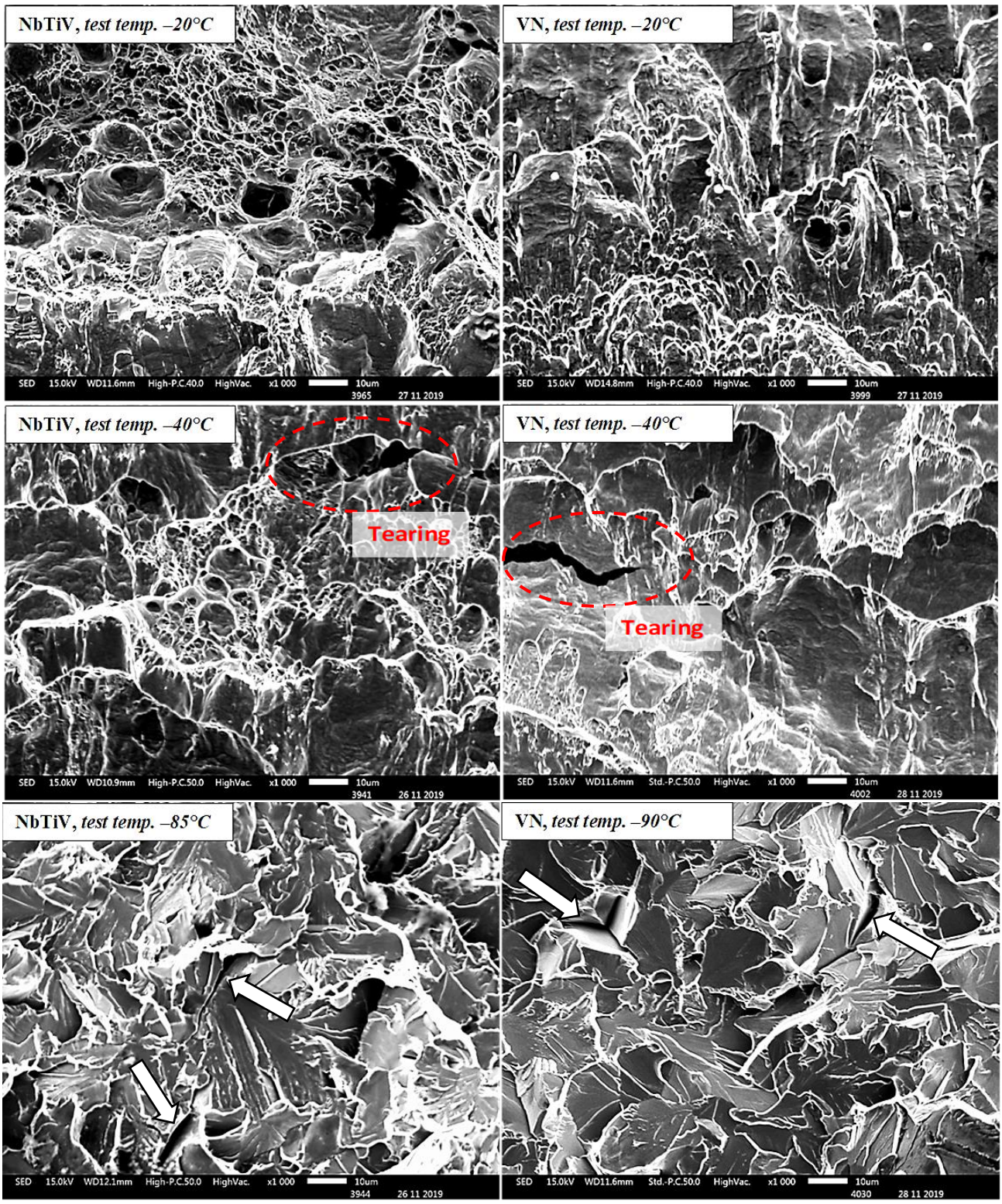


Figure 4.21: SEM fractographs for the NbTiV (left) and VN (right) after the **NHT**. Test temperatures are also indicated in the inserts. White arrows show cleavage cracks (at –85 & –90 °C). At a test temperature of –40 °C, ductile modes are characterised by dimples and tearing (red circled area) in both samples.

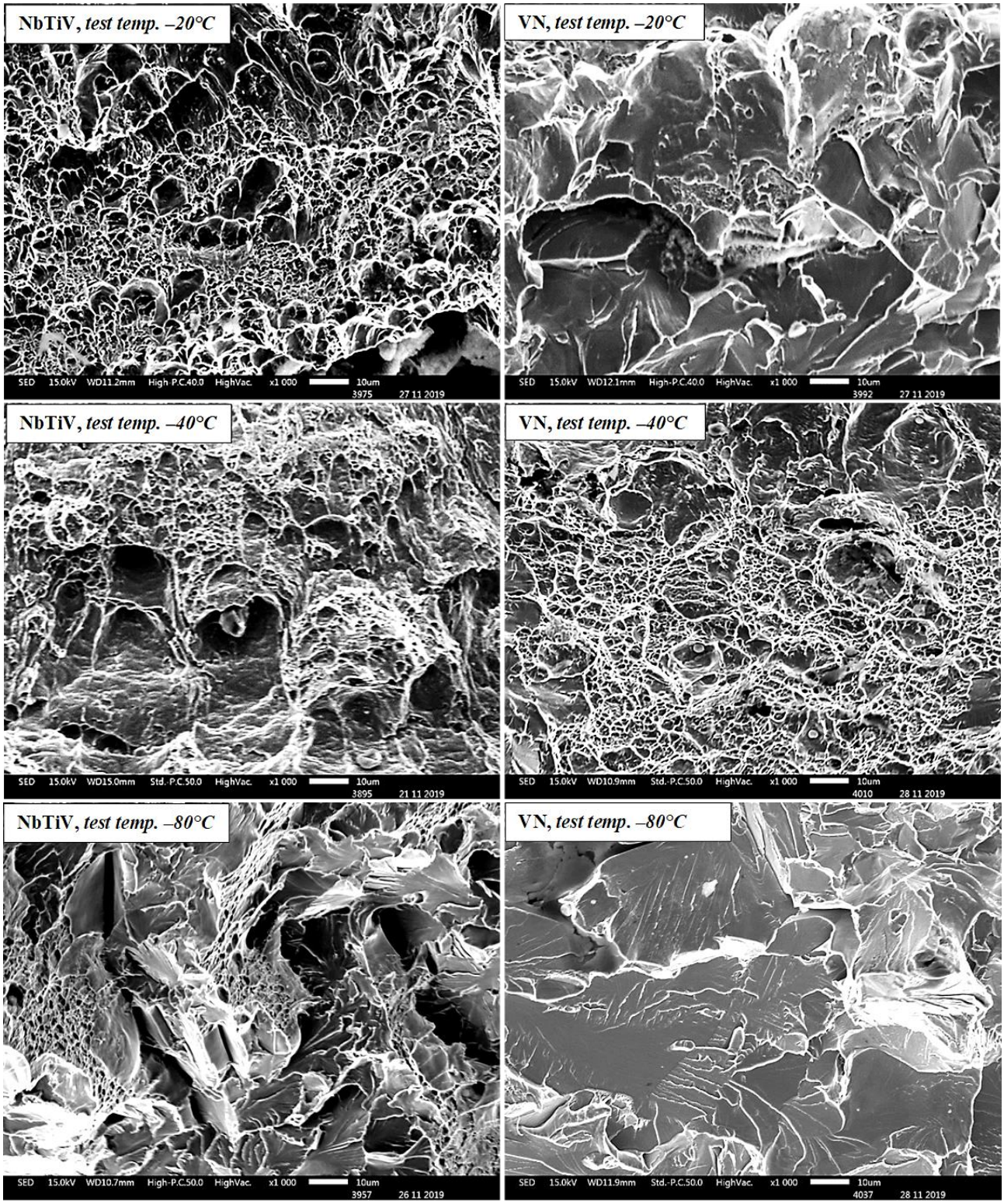


Figure 4.22: SEM fractographs for the NbTiV (left) and VN (right) after the **DAHT**. Test temperatures also indicated in the inserts. Plane and smooth faceted fracture surfaces at a test temperature of –80 °C. Test temperature of –40 °C showing ductile modes characterised by dimples in both samples.

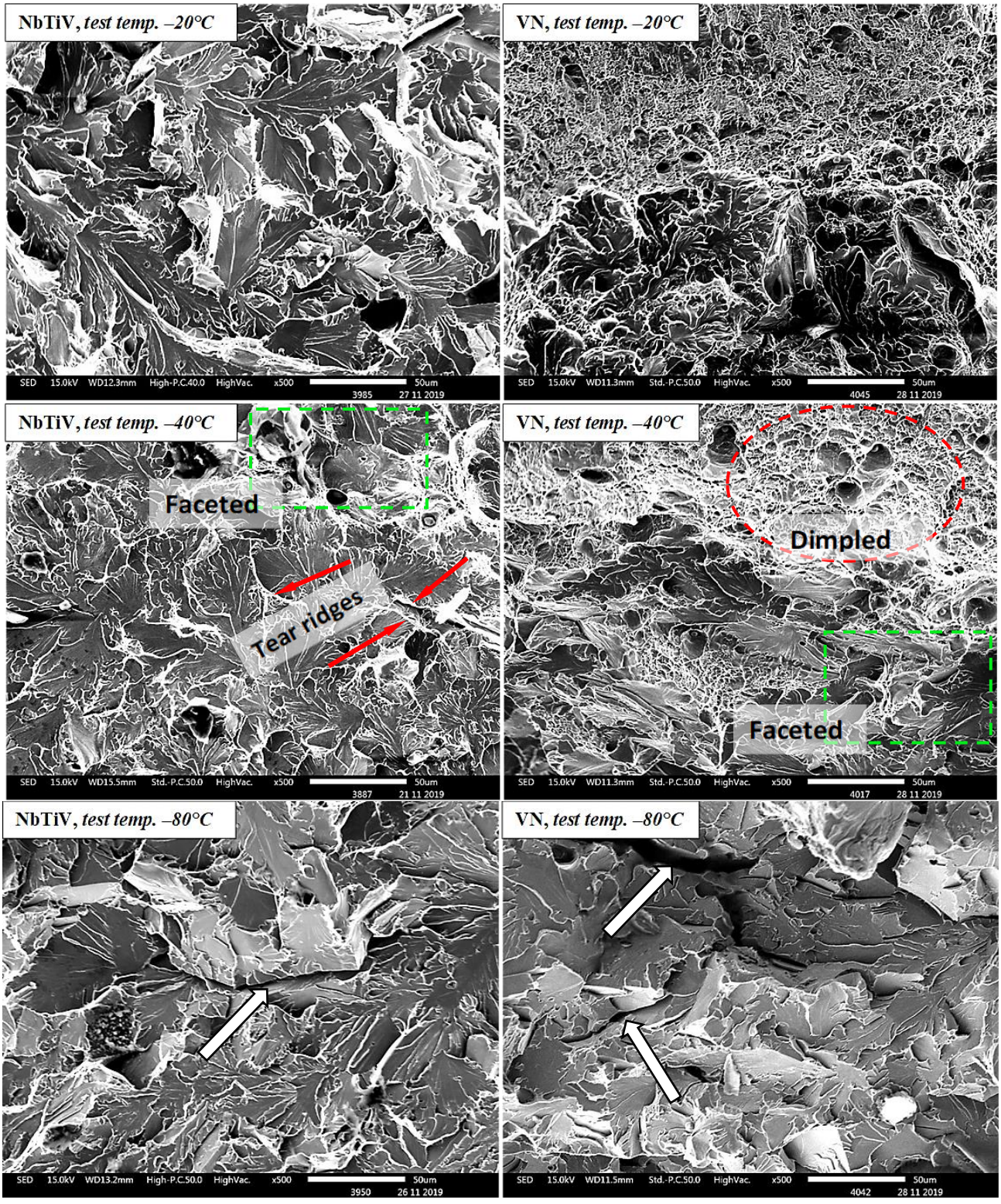


Figure 4.23: SEM fractographs for the NbTiV (left) and VN (right) after the **IAHT**. Test temperatures are also indicated in the inserts. Smooth-faceted fracture surfaces. White arrows showing cleavage cracks at a test temperature of –80 °C. A mixed-mode of fracture at a test temperature of –40 °C.

CHAPTER 5 ANALYSIS AND DISCUSSION

5.1 Introduction

This chapter presents the analysis and discussion of the results of this study. The influence of the applied heat treatments on the microstructural evolution towards homogenisation and elimination of microstructural banding in the NbTiV and VN microalloyed steels will be discussed. Furthermore, the influence of the heat treatments on the mechanical properties of the NbTiV and VN microalloyed steels will also be discussed. Finally, conclusions on the responses of the study-steels towards the applied heat treatment cycles will be drawn and presented.

5.2 Effect of heat treatment on the microstructural evolution of the NbTiV and VN microalloyed steels

5.2.1 Normalising Heat Treatment (NHT)

This heat treatment involved heating the hypoeutectoid study-steels (VN-steel, 16 mm and NbTiV-steel, 30 mm plates) for 30 minutes to the austenitisation temperature; soaking at 930 °C for 30 minutes and air-cooling them to room temperature, each steel with its cooling path. Section 4.5 shows microstructures of both steel samples after undergoing the NHT (Figure 4.11*a* & Figure 4.12*a*). The NbTiV microstructure shown in Figure 4.11(a) shows a refined ferrite grain structure with an average ferrite grain size of 11 ± 1 μm, from that of 27.5 ± 2.9 μm in the as-hot rolled condition. This is expected, as normalising heat treatment produces grain refinement [112], [160], [161]. During the austenitisation period, the diffusion-controlled formation of austenite, which mainly takes place preferentially at ferrite-pearlite interphases, proceeds along with redistribution and homogenisation (if enough time at temperature) of chemical elements (chiefly carbon) in the austenite matrix [54], [122]. The Thermo-Calc predictions for the NbTiV-steel (Figure 3.7 *ii*) showed undissolved TiC, AlN, TiN and (Nb, Ti)C precipitates (increasing volume fractions in that order) at 930 °C. All these precipitates play a measurable role in inhibiting austenite grain growth during austenitisation. This,

therefore, maintains a fine austenite grain structure which provides an increased grain boundary area and high nucleation rate of the ferrite hence, the refined ferrite grain size. This was also reported in other studies [98], [162], [163]. The same behaviour was also observed in the VN-steel, with an average ferrite grain size of 18 ± 1 μm, from that of 21 ± 1.5 μm in the as-hot rolled condition. The precipitates predicted in the VN-steel by Thermo-Calc were at 930 °C and was AlN only (Figure 3.8 *ii*), and these were the ones responsible for inhibiting austenite grain growth at this austenitisation temperature.

Also, for continuous cooling transformations such as air-cooling, the transformation only takes place in a particular temperature range, where the transformation from austenite to pearlite decreases with increasing cooling rate. Air-cooling rates result in a high driving force and hence a high nucleation rate for the ferrite reaction that results in a fine mean ferrite grain size [164], as opposed to furnace cooling rates where the ferrite nucleation rate is slow. This is what is being observed in the NHT microstructures in Figure 4.11*(a)*. The same also applies to the VN-steel microstructures in Figure 4.12*(a)* that underwent the NHT.

Another observation in the microstructures of the NbTiV-steel in Figure 4.11*(a)* is the ferrite-pearlite banding that has been retained even after undergoing the NHT. This implies that the austenite matrix did not completely homogenise during austenitisation. Such that upon air cooling, the unhomogenised austenite, therefore, resulted in a banded ferrite-pearlite. It has been shown in the literature that these chemical inhomogeneities that are present in the austenite matrix render sites preferential to ferrite or pearlite nucleation depending on the chemical gradients, therefore, leading to the retention of the ferrite-pearlite banding [79], [91]–[93]. The austenite inhomogeneity was also evident in the PAG microstructure of both NbTiV and VN-steels presented in Figure 4.7*(b)* and *(d)*, respectively, in section 4.4. A dark centre line in the middle of the plate as that reported by Pallaspuro *et al*. [165], was apparent after revealing the quenched PAG structure.

Between the two studied steel grades, the apparent retention of ferrite-pearlite banding after the NHT was more severe in the VN-steel. There seems to be some consistency for the VN-steel to retain the banding more after a certain heat treatment than the NbTiV-steel. This aspect seems to correlate with the initial state of banding in the as-hot rolled condition. That is, the higher the degree of banding in the as-hot rolled condition, the greater the retention after the NHT (see the comparison in Figure 4.9 for the DAHT, and Figure 4.10 for the IAHT).

5.2.2 Double Austenitisation Heat Treatment (DAHT)

The DAHT involved heating for 30 minutes to the austenitisation temperature (930 °C); soaking for 30 minutes followed by air-cooling to room temperature, and then heating for 30 minutes to another austenitisation cycle in the intercritical temperature region at 775 °C and finally air-cooling to room temperature. This heat treatment like the NHT also resulted in ferrite grain refinement (12 ± 1 μm), and a more remarkable pearlite refinement than in the NHT. Another important observation from the optical micrographs for the NbTiV-steel in Figure 4.11 *(b)* and *(c)* is the absence of ferrite-pearlite banding and the apparent homogeneous pearlite.

Austenite transformation during austenitisation in the intercritical temperature region only takes place in the carbon-rich regions that initially contained pearlite while the carbon-lean regions remain ferritic [80]. Therefore, the pearlite bands dissolve and transform to austenite during the intercritical annealing and carbon diffuses through shorter distances thereby ensuring austenite homogenisation. With enough time allowed at the soaking temperature other elements such as Mn also redistribute in austenite [123], [125]. This is what is manifesting in the NbTiV-steel microstructures (Figure 4.11*c*, large white arrows), and to a lesser extent also in the VN-steel. During air-cooling, the stabilised austenite due to the carbon enrichment delays pearlite transformation to lower temperatures, hence, this produces the very fine pearlite, Figure 4.11*(c)* (black arrows). A confirmation at high magnification (x4000), Figure 4.14*(a)* & *(c)*, shows the fine pearlite colonies along the ferrite grain boundaries and on grain corners. It was also reported in other studies [122], [127] in which, through CCT diagrams, it was shown that cooling the austenite phase from the intercritical phase region significantly delays the transformation of pearlite compared to cooling from the fully single austenite phase region thereby increasing the undercooling that results in fine pearlite.

The DAHTs were also performed for intercritical annealing temperatures of 740 and 810 °C in an optimisation investigation of the microstructures of both steel samples. As it can be observed from the optical microstructures in Figure 4.9, banding was still heavily retained after intercritical annealing at 740 °C, and lightly retained at 810 °C. However, among the three intercritical annealing temperatures, DAHT-810 °C produced the finest ferrite-pearlite structure with the intermediate one being DAHT-775 °C. This is expected as the DAHT-810 °C gave the largest undercooling. With regards to the absence of the ferrite-pearlite banding and a more uniform pearlite distribution, DAHT-775 °C was optimal. This is because the effective carbon content in the austenite at the intercritical temperature of 775 °C is higher than that at 810 °C due to the higher austenite volume fraction, see Figure 4.2. Because of the higher effective carbon content in austenite at 775 °C, which enriches the austenite more than at 810 °C, upon continuous air-cooling the pearlite transformation was delayed much longer in the 775 °C, resulting in a reduced volume fraction of pearlite (degenerate).

At 740 °C, the kinetics are slower (due to slow diffusion rates), such that the magnitude of austenite heterogeneity due to carbon enrichment (at prior pearlite regions) was higher for the intercritical annealing temperature of 740 °C than that of 775 °C. It was therefore expected that the austenite at 740 °C was more heterogeneous, with a very high effective carbon concentration, than that at 775 °C. Furthermore, the pearlite dissolution rate at low intercritical annealing temperatures is several magnitudes lower than at higher temperatures. Speich *et al*. [124] referred to this as partial pearlite dissolution. For instance, Garcia and Deardo [166], Fonstein [122], and Speich [124] reported that the pearlite dissolution rate in an initial microstructure of ferrite and pearlite increases by three orders of magnitude with annealing temperature increase from 730 to 780 °C, which is a relatively similar temperature range of the current study (740 to 775 °C).

5.2.3 Intercritical Annealing Heat Treatment (IAHT)

In this heat treatment, the steel samples were heated to the intercritical annealing temperature of 775 °C for 30 minutes, soaked at that temperature for 30 minutes and then air-cooled to room temperature. The optical micrographs for both steel samples in Figure 4.11*(d)* and Figure 4.12*(c)* show the microstructures that underwent the IAHT, and both portray similar characteristics. The microstructure contains a bimodal ferrite grain size distribution, Figure 4.13, with some fine ferrite grains and mostly coarse ferrite grains. An apparent increase in the ferrite volume fraction also occurred after this heat treatment (see inserts in Figure 4.11 and Figure 4.12). Moreover, the heat treatment also produced pearlite refinement, relatively intermediate between the NHT and DAHT. The pearlite in the microstructures was also mostly degenerated, in combinations with some lamellar pearlite nodules. According to Ohmori [167], a degenerated pearlite morphology comprises colonies of nonparallel and broken up cementite lamellae in a ferritic matrix. This is what is being observed in the red-dot circled regions from the SEM micrographs in Figure 4.15 *(a)* and *(b)* (NbTiV and VN-steel respectively).

The reason for the bimodal ferrite grain size distribution is that, during the intercritical annealing, the microstructure comprises retained ferrite (that does not transform to austenite during intercritical annealing), and the austenite that formed from the pearlite. Therefore, cooling from the intercritical (α+γ) phase region promotes the epitaxial growth of ferrite. Sarwar *et al*. [168] defined epitaxial ferrite as, "ferrite formed by the transformation of austenite by epitaxial growth on the retained ferrite (used as a substrate) without the nucleation stage when cooling from the intercritical temperature". This epitaxial ferrite is finer than the retained ferrite, hence the bimodal ferrite distribution. Another characteristic feature that can be observed from the epitaxial ferrite, is that it is usually precipitate-free (PF). SEM micrographs in Figure 4.15 show the PF ferrite grains which indicates the epitaxial

growth process that occurred during air cooling. The PF ferrite grains were also observed in another study by Geib *et al*. [45], where with the aid of an etchant (boiling alkaline chromate), the authors managed to differentiate the retained ferrite from epitaxial ferrite since the two types of ferrite etch differently (Figure 2.21). It was concluded that intercritical annealing yields precipitation in the retained ferrite, and no precipitation in the epitaxial ferrite. This was also observed in the current study. Finally, on the slight increase in the ferrite volume fraction, the epitaxial ferrite causes a further enrichment of the surrounding austenite with carbon. As mentioned earlier in section 5.2.2, air cooling this austenite delays pearlite transformation, while on the other hand raising the ferrite start temperature [127]. This could be the explanation for the slight increase in the ferrite volume fraction (see inserts in Figure 4.11*d* and Figure 4.12*c*); also reported by [169].

The degenerate pearlite, like the normal lamellar pearlite, also forms through the diffusion of carbon. Ohmori [167] investigated the mechanism by which degenerate pearlite forms, and attributed the formation of degenerated pearlite to carbon depletion along the austenite grain boundaries. This consequently leads to inadequate carbon diffusion to form continuous cementite lamellae. In the current study, this behaviour was observed after air cooling from the intercritical annealing temperature. Lu *et al*. [170], proposed that fast cooling rates as those involved during the normalising heat treatment also contribute to the insufficient carbon diffusion for the formation of continuous cementite lamella. Austenitisation in the two-phase region produces an austenite phase that is characterised by significant chemistry heterogeneities as opposed to full austenitisation. Hence, this might be the explanation for the formation of the degenerate pearlite upon cooling from an intercritical annealing temperature. Other authors also suggested another cause of degenerate pearlite as being the interphase precipitation of carbides that take up carbon [167], [170]–[172]. Honeycombe [173] and, Davenport and Becker [174] pointed out that interphase precipitation during continuous cooling is most often observed in steels alloyed with strong carbide formers such as Nb, Ti, V, Mo, Cr and W; and the steels in the current study are microalloyed with these elements.

5.3 Impact of heat treatment on mechanical properties of NbTiV and VN microalloyed steels

5.3.1 Tensile properties

Figure 4.16 shows that the NHT produced the highest yield strength and fracture elongation in both steel grades. It was shown in Figure 4.11 *(a)* and also discussed in section 5.2.1 that this heat treatment resulted in ferrite grain refinement. This could be the explanation for the relatively high yield strength and fracture elongation, which typifies the Hall-Petch relationship [175]. The yield strength and fracture elongation from the DAHT and IAHT samples were lower than those of the NHT; that is, despite the ferrite grain refinement that was also observed in the NbTiV-steel after the DAHT, there was a 12% drop in the yield strength (from 404 to 355 MPa). The drop in the yield strength after the IAHT was justifiable since this heat treatment resulted in a coarse ferrite grain structure. The drop in strength after the DAHT can be explained by the effect of the number of normalising cycles on the physical mechanisms in the microstructure, such as coarsening of precipitates that do not dissolve at that soaking temperature (775 °C). Precipitation strengthening becomes progressively compromised with multiple normalising cycles [176]. A similar trend in the yield strength and fracture elongation was also observed in the VN-steel shown in the same Figure 4.16 *(iii) & (iv)*. These yield strength results show that the tensile properties of the NbTiV and VN-steels are not affected by banding. This can be evidenced by the best tensile properties (especially R_p and A_5) that were found in the steel samples that underwent the NHT and significantly retained the ferrite-pearlite banding. Similar conclusions were also made in other studies [81], [98]–[100]. However, the conclusions regarding the effect of pearlite banding on the total elongations varied among the aforesaid studies. In the current study, the fracture elongation of the studied steels has shown to be unaffected by the ferrite-pearlite banding. Regarding hardness, the steel samples that underwent the IAHT gave the highest hardness values, followed by the DAHT and then the NHT. Similarly, the IAHT also gave the highest UTS values. This was expected since there exists a linear relationship between UTS and hardness.

Regarding the work hardening results in Figure 4.17 and Table 4-4, the n–values after the NHT and DAHT did not differ much in both steel grades. However, the difference was observed in the IAHT which produced fairly the lowest n–values. This indicates low work hardening capacity for those samples that underwent the IAHT. A notable microstructural difference brought about by the IAHT that could attribute to this work hardening behaviour is the coarse ferrite grain structure. This can be explained by McCabe *et al*'s [177] model regarding geometrically necessary dislocations (GNDs).

According to their model, the effects of GNDs (normally located at grain boundaries) extend into the grains for some distance thereby occupying some volume fraction. Therefore, with a small grain size distribution, the volume of GNDs tends to occupy a larger fraction of the total volume in the material. This implies that with the same amount of deformation, a material with fine grains work-hardens more rapidly than that with coarse grains.

The ferrite volume fraction in a two-phase material is also known to affect the work hardening rate. As was shown in Figure 4.11*d* and Figure 4.12*c* (also discussed in section 5.2.3), the IAHT yielded the highest ferrite volume fraction. In the current study, TEM work was not performed, as it was out of the scope of this study, but this technique can be utilised to analyse and confirm the deformation behaviour of ferrite and pearlite. However, it has been reported elsewhere that the ferrite volume fraction influences the work hardening behaviour of a steel's microstructure comprising ferrite+harder phase [153], [155], [178]. The resultant pearlite after the IAHT contains a high carbon content due to an increase in the ferrite volume fraction and epitaxial ferrite formation during intercritical annealing. Therefore, this increases the strength difference between the ferrite and pearlite. Hence, the work hardening capacity of the steel is slightly reduced because of the resistance to plastic deformation by the harder phase, which makes it difficult for the transitioning of the work hardening from ferrite (softer phase) to pearlite (harder phase) [54], [153], [178].

Micro-Vickers hardness measurements on the ferrite matrix were performed to investigate the cause of the high hardness values that were observed in the IAHT samples. Just as with macro-HV, the samples that underwent the IAHT recorded the highest hardness values (Table 4-4). The reason for this high hardness in the ferrite matrix could be attributed to precipitation hardening together with the inhomogeneous distribution of carbon during the annealing. To substantiate this claim, SEM-EDS spectra were done on the particles in the ferrite matrix for both steel grades after the IAHT and DAHT. According to the EDS spectra for the NbTiV-steel sample that underwent the IAHT that is shown in Figure 8.8*(a)* in Appendix A.8 (section 8.8), some of the particles can be identified as carbides of (Nb, Ti, V)(C, N) and AlN. Also judging from the SEM micrographs, the DAHT sample in Figure 8.8*(b)* shows a lower particle volume fraction than that of the IAHT sample. As discussed earlier, this could be due to coarsening (at the expense of fine particles) of some of the particles during the multiple normalising cycles. Figure 8.8*(c)* and *(d)* show the VN-steel samples that were exposed to the IAHT and DAHT respectively and are also depicting the same coarsening aspect. It can also be seen from the EDS spectra for the VN-steel samples that the particles are identified as AlN (spectrum 4, Figure 8.8 *(c)*) and cementite carbides (spectrum 57, Figure 8.8 *(d)*).

5.3.2 Charpy V-Notch impact toughness

The DAHT exhibited the highest USE in both steel samples, though with a relatively insignificant difference from the NHT. Table 5-1 shows the influence of the test temperature on the absorbed impact energy for the steel samples after the respective heat treatments. In the NbTiV-steel, the DAHT's absorbed impact energy dropped significantly (by 45%) with a decrease in the test temperature to –40 °C, and by 15% in the VN-steel. The drop in the impact absorbed energy was highest in the IAHT with 68% and 51% for the NbTiV and VN-steel, respectively.

Table 5-1: Percentage decrease in the impact-absorbed energy between the upper shelf energy (USE) and at a test temperature of –40 °C in the heat treated NbTiV and VN-steel samples.

Heat Treatment Type	% Decrease in impact absorbed energy $= \frac{(USE - E_{at\ -40°C})}{USE} \times 100$	
	NbTiV-steel	VN-steel
NHT	20	20
DAHT	45	15
IAHT	68	51

These trends in the CVN impact toughness properties for the heat treatment investigated can be linked to the microstructural characteristics. These characteristics, discussed in section 5.2 with the aid of microstructures show that the DAHT and NHT produced ferrite grain refinement in the study-steels which explains the comparable CVN impact curves shown in Figure 4.19. The upper shelf energy in both steel samples for the DAHT, which was higher than that of the NHT, could be attributed to the more uniform distribution of the pearlite in the ferrite-pearlite microstructure that was produced by the DAHT. The NHT samples still had pearlite banding retention, where the banding retention was greater in the VN-steel as compared to the NbTiV-steel.

For both steel samples, the IAHT produced the lowest CVN shelf energy. It was shown in Figure 4.11 and Figure 4.12 that the IAHT resulted in a coarse ferrite grain size distribution. It is well known that coarse ferrite grains yield low CVN impact shelf energies, since fine microstructural features such as the ferrite grain size in this case, renders strong resistances to cleavage microcracking [179]. Furthermore, the IAHT samples recorded relatively high macro-Vickers hardness and UTS values, which also explains the low impact toughness. Also, when the test temperature decreased to –40 °C, the IAHT recorded the largest drop in the impact-absorbed energy in both steel grades. This factor could also be linked to the significant drop in the amount of absorbed impact energy in the DAHT for the NbTiV-steel. The intercritical annealing cycle in the DAHT indicates a negative impact on the CVN impact toughness, especially in the NbTiV-steel.

Regarding the yield strength specification requirements (for structural applications) for the NbTiV-steel in Figure 4.20, the IAHT was marginally above the minimum requirement, whereas the DAHT and NHT were well above the minimum requirement. In the VN-steel, the DAHT failed to meet the minimum yield strength requirement, the IAHT marginally above again, and the NHT was well above the minimum requirement. The minimum requirements for the CVN impact toughness were met for all heat treatments in both steel grades. Overall, the summary in Figure 4.20 shows that the best combination of impact toughness and yield strength is achieved with the NHT (both at room temperature and –40 °C) in both steel grades.

CHAPTER 6 CONCLUSIONS AND RECOMMENDATIONS

6.1 Conclusions

The influence of the normalising heat treatment, double austenitisation heat treatment and intercritical annealing heat treatment on the NbTiV and VN microalloyed steels for high strength, high impact toughness and microstructural homogenisation was investigated in this study. And from the results of the investigation, the following important conclusions were drawn:

- The incoming as-hot rolled microstructure of both steel grades showed banding, with more microstructural banding in the 16 mm thick VN-steel than the 30 mm thick NbTiV-steel plate. These differences in the excessiveness of banding were directly linked with the amount of deformation after hot rolling.

- DAHT-775 proved to be the heat treatment route that successfully eliminated the microstructural banding and achieved pearlite homogeneity, in addition to the ferrite grain refinement. This was apparent in both steel grades. The IAHT also produced some noticeable pearlite homogeneity, though with a coarse and bimodal ferrite grain size distribution due to the epitaxial mechanism of ferrite formation during air-cooling from the intercritical annealing temperature.

- The DAHT produced superior upper shelf energy values in both steel grades (NbTiV– 259 J and VN– 293 J) though not far from the NHT (NbTiV– 246 J and VN– 263 J). The best impact toughness at –40 °C, in the NbTiV-steel (196 J), was achieved through the NHT, and the DAHT in the VN-steel (249 J). The second intercritical annealing cycle was associated with a drop of the impact toughness at –40 °C, for instance, from 196 to 143 J in the NbTiV-steel. However, the best impact toughness-strength combination was achieved with the NHT in both study-steels, while the IAHT attributed the worst CNV impact toughness properties due to its coarse and bimodal ferrite grain size distribution.

- All heat treatments passed the standard minimum requirements for the CVN impact toughness properties, nevertheless, only the DAHT in the VN-steel fell below the standard yield strength minimum requirements.

- The tensile properties (R_p, UTS and A_5) were not affected by microstructural banding.

- A higher degree of banding in the as-hot rolled condition, correlated to greater retention of microstructural banding after the applied heat treatment.

6.2 Recommendations

Based on this work, the following recommendations have been made and may be considered for future work:

- Further work into precipitation analysis could also be done through TEM to quantify how the DAHT and IAHT impacted precipitation and hence the mechanical properties.

- Compare the response of studied steels to the heat treatments with the same initial as-hot rolled conditions, that is, subjecting the studied steels to the same amount of deformation before the investigation of the different heat treatment routes.

- Inclusion of the transverse orientation in addition to the longitudinal should also have been explored. An-isotropic impact strengths in the transverse directions to the hot rolling directions of the study steels would have added significant findings on the role of the applied heat treatments to the mitigation by the heat treatments of the differences in impact toughness between the rolling and transverse directions.

CHAPTER 7 REFERENCES

[1] GWEC, “Global wind energy council report 2018,” *Wind Glob. Counc. Energy*, no. April, pp. 1–61, 2019.

[2] S. Sawyer, D. Morten, and A. Rebollo, “Annual market update 2017; Global wind report,” 2015.

[3] J. Patel and S. Jansto, “Niobium high strength steels for greener wind power generation,” *Millenium Steel*, pp. 171–175, 2012.

[4] W. Paper, “Steelmakers Meet Demand for Taller Wind Towers with Low Carbon Structural Steel Containing Niobium,” no. September, 2018.

[5] K. Taylor *et al.*, “Evaluation of low and medium-carbon Nb-Microalloyed plate steels for wind tower applications,” *Iron Steel Technol.*, vol. 8, no. 10, pp. 127–137, 2011.

[6] ASTM A572/A572M − 18, “Standard Specification for High-Strength Low-Alloy Columbium-Vanadium Structural Steel,” *Am. Soc. Test. Mater. Int.*, pp. 1–4, 2018.

[7] S. G. Hong, H. J. Jun, K. B. Kang, and C. G. Park, “Evolution of precipitates in the Nb-Ti-V microalloyed HSLA steels during reheating,” *Scr. Mater.*, vol. 48, no. 8, pp. 1201–1206, 2003.

[8] B. R. Kumar, “A Review on the importance of microalloying in steel,” *Int. J. Mech. Eng. Technol.*, vol. 5, no. 2, pp. 187–193, 2014.

[9] T. N. Baker, “Microalloyed steels,” *Adv. Mater. Process.*, vol. 137, no. 1, pp. 17–18, 1990.

[10] G. S. Rohrer, “‘‘Introduction to Grains, Phases, and Interfaces — An Interpretation of Microstructure",” *Miner. Met. Mater. Soc. ASM Int.*, vol. 175, no. May, pp. 15–51, 2010.

[11] S. Vervynckt, K. Verbeken, B. Lopez, and J. J. Jonas, “Modern HSLA steels and role of non-recrystallisation temperature,” *Int. Mater. Rev.*, vol. 57, no. 4, pp. 187–207, 2012.

[12] S. F. Medina, M. I. Vega, M. Gómez, and P. P. Gómez, “Influence of the Size and Volume Fraction of TiN Particles on Hot Strength and Dynamic Recrystallisation in Structural Steels,” *ISIJ Int.*, vol. 45, no. 9, pp. 1307–1315, 2005.

[13] T. PAN, C. fu YANG, Y. MA, D. mei XUE, and Y. Q. ZHANG, "Chemistry and Process Optimization of V-Microalloyed N80-Class Seamless Casing Tube," *J. Iron Steel Res. Int.*, vol. 17, no. 3, pp. 72–78, 2010.

[14] S. Endo and N. Nakata, "Development of Thermo-Mechanical Control Process (TMCP) and high-performance steel in JFE Steel," *JFE Tech. Rep.*, vol. 20, no. 20, pp. 1–7, 2015.

[15] R. Lagneborg, T. Siwecki, S. Zajac, and B. Hutchinson, "The Role Of Vanadium In Microalloyed Steels," *Scand. J. Metall.*, vol. 28, no. 5, pp. 186–241, 1999.

[16] A. McCrone and U. Moslener, "Global Trends in Renewable Energy Investment 2018," 2018.

[17] D. Oakley and N. Baddoo, "Niobium Microalloyed Structural Steels," 2014. [Online]. Available: https://www.oakleysteel.co.uk/niobium-microalloyed-structural-steels. [Accessed: 20-Nov-2019].

[18] S. Mraz, "Microalloying Strengthens Steel," 2016. [Online]. Available: http://machinedesign.com/materials/microalloying-strengthens-steel. [Accessed: 20-Nov-2019].

[19] W. L. Gao, Y. Leng, D. F. Fu, and J. Teng, "Effects of niobium and heat treatment on microstructure and mechanical properties of low carbon cast steels," *Mater. Des.*, vol. 105, pp. 114–123, 2016.

[20] H. Najafi, J. Rassizadehghani, and S. Asgari, "As-cast mechanical properties of vanadium/niobium microalloyed steels," *Mater. Sci. Eng. A*, vol. 486, no. 1–2, pp. 1–7, 2008.

[21] H. Najafi, J. Rassizadehghani, and S. Norouzi, "Mechanical properties of as-cast microalloyed steels produced via investment casting," *Mater. Des.*, vol. 32, no. 2, pp. 656–663, 2011.

[22] X. Chen *et al.*, "Design, Manufacture and Maintenance of High-Parameter Pressure Vessels in China," 2014, p. V001T01A082.

[23] J. Patel, "The value of high strength steels, enabling low carbon energy technologies: Offshore wind farms," *SEAISI Q. (South East Asia Iron Steel Institute)*, vol. 46, no. 4, pp. 68–75, 2017.

[24] S. Cai and J. D. Boyd, "Mechanism of Microstructural Banding in Hot Rolled Microalloyed Steels," *Mater. Sci. Forum*, vol. 500–501, no. August, pp. 171–178, 2005.

[25] ASTM E 1268-01, "Standard Practice for Assessing the Degree of Banding or Orientation of Microstructures," *Am. Soc. Test. Mater. Int.*, no. Reapproved 2016, pp. 1–29, 2016.

[26] F. G. Caballero, A. Garcia-Junceda, C. Capdevila, and C. G. de Andres, "Evolution of Microstructural Banding during the Manufacturing Process of Dual-Phase Steels," *Mater. Trans.*, vol. 47, no. 9, pp. 2269–2276, 2006.

[27] W. A. Spitzig, “Effect of sulfide inclusion morphology and pearlite banding on anisotropy of mechanical properties in normalized C-Mn steels,” *Metall. Trans. A*, vol. 14A, no. 2, pp. 471–484, 1983.

[28] R. A. Grange, “Effect of microstructural banding in steel,” *Metall. Trans.*, vol. 2, pp. 417–426, 1971.

[29] R. Rana and S. B. Singh, *Automotive Steels: Design, Metallurgy, Processing and Applications*. Cambridge: Woodhead publishing, 2016.

[30] J. C. Villalobos, A. Del-Pozo, B. Campillo, J. Mayen, and S. Serna, “Microalloyed steels through history until 2018: Review of chemical composition, processing and hydrogen service,” *Metals (Basel).*, vol. 8, no. 5, 2018.

[31] D. L. Silva, W. Regone, and S. T. Button, “Microstructure and mechanical properties of microalloyed steel forgings manufactured from cross-wedge-rolled preforms,” *Brazilian J. Chem. Eng.*, vol. 54, no. 2, pp. 213–218, 2006.

[32] P. Russo Spena and D. Firrao, “Thermomechanical warm forging of Ti-V, Ti-Nb, and Ti-B microalloyed medium carbon steels,” *Mater. Sci. Eng. A*, vol. 560, pp. 208–215, 2013.

[33] P. Skubisz, Ł. Lisiecki, and P. Micek, “Effect of Direct Cooling Conditions on Characteristics of Drop Forged Ti+V+B Microalloy Steel,” *Procedia Manuf.*, vol. 2, no. February, pp. 428–433, 2015.

[34] J. W. Morris, C. S. Lee, and Z. Guo, “The nature and consequences of coherent transformations in steel,” *ISIJ Int.*, vol. 43, no. 3, pp. 410–419, 2003.

[35] J.R. Davis, *Alloying Understand The Basic*. Ohio: ASM International, 2001.

[36] S. W. Thompson, D. J. Vin Col, and G. Krauss, “Continuous cooling transformations and microstructures in a low-carbon, high-strength low-alloy plate steel,” *Metall. Trans. A*, vol. 21, no. 6, pp. 1493–1507, 1990.

[37] M. C. Zhao, K. Yang, F. R. Xiao, and Y. Y. Shan, “Continuous cooling transformation of undeformed and deformed low carbon pipeline steels,” *Mater. Sci. Eng. A*, vol. 355, no. 1–2, pp. 126–136, 2003.

[38] W. Yan, Y. Y. Shan, and K. Yang, “Effect of TiN inclusions on the impact toughness of low-carbon microalloyed steels,” *Metall. Mater. Trans. A Phys. Metall. Mater. Sci.*, vol. 37, no. 7, pp. 2147–2158, 2006.

[39] H. Beladi and P. D. Hodgson, “Effect of carbon content on the recrystallization kinetics of Nb-steels,” *Scr. Mater.*, vol. 56, no. 12, pp. 1059–1062, 2007.

[40] J. M. Gray and F. Siciliano, “High Strength Microalloyed Linepipe : Half a Century of Evolution,” *Proc. an Int. Symp. high-strength, low-alloy steels.*, pp. 1–26, 1959.

[41] Z. Chen, M. H. Loretto, and R. C. Cochrane, “Nature of large precipitates in titanium-containing HSLA steels,” *Mater. Sci. Technol. (United Kingdom)*, vol. 3, no. 10, pp. 836–844, 1987.

[42] M. Prikryl, A. Kroupa, G. C. Weatherly, and S. V. Subramanian, “Precipitation behavior in a medium carbon, Ti-V-N microalloyed steel,” *Metall. Mater. Trans. A Phys. Metall. Mater. Sci.*, vol. 27, no. 5, pp. 1149–1165, 1996.

[43] A. Karmakar, S. Biswas, S. Mukherjee, D. Chakrabarti, and V. Kumar, “Effect of composition and thermo-mechanical processing schedule on the microstructure, precipitation and strengthening of Nb-microalloyed steel,” *Mater. Sci. Eng. A*, vol. 690, no. February, pp. 158–169, 2017.

[44] L. Ming, Q. Wang, H. Wang, C. Zhang, Z. Wei, and A. Guo, “A remarkable role of niobium precipitation in refining microstructure and improving toughness of A QT-treated 20CrMo47NbV steel with ultrahigh strength,” *Mater. Sci. Eng. A*, vol. 613, pp. 240–249, 2014.

[45] M. D. Geib, D. K. Matlock, and G. Krauss, “The effect of intercritical annealing temperature on the structure of niobium microalloyed dual-phase steel,” *Metall. Trans. A*, vol. 11, no. 10, pp. 1683–1689, Oct. 1980.

[46] Gladman T, McIvor ID, and Pickering FB, “Effect of carbide and nitride particles on the recrystallization of ferrite,” *J Iron Steel Inst*, 1971.

[47] K. J. Lee and J. K. Lee, “Modelling of γ/α transformation in niobium-containing microalloyed steels,” *Scr. Mater.*, vol. 40, no. 7, pp. 831–836, 1999.

[48] X. Q. Yuan, Z. Y. Liu, S. H. Jiao, L. Q. Ma, and G. D. Wang, “The onset temperatures of γ to α-phase transformation in hot deformed and non-deformed Nb micro-alloyed steels,” *ISIJ Int.*, vol. 46, no. 4, pp. 579–585, 2006.

[49] S. C. Hong, S. H. Lim, H. S. Hong, K. J. Lee, D. H. Shin, and K. S. Lee, “Effects of Nb on strain induced ferrite transformation in C-Mn steel,” *Mater. Sci. Eng. A*, vol. 355, no. 1–2, pp. 241–248, 2003.

[50] Q. Yu and Y. Sun, “Abnormal growth of austenite grain of low-carbon steel,” *Mater. Sci. Eng. A*, vol. 420, no. 1–2, pp. 34–38, 2006.

[51] S. A. J. Chalimba, R. J. Mostert, W. E. Stumpf, C. W. Siyasiya, and K. M. Banks, “Effects of Roughing on Finish Rolling Simulations in Microalloyed Strip Steels,” *J. Mater. Eng. Perform.*, vol. 26, no. 11, pp. 5294–5303, 2017.

[52] S. Zajac, T. Siwecki, W. B. Hutchinson, and R. Lagneborg, “The role of carbon in enhancing precipitation strengthening of V-microalloyed steels,” *Mater. Sci. Forum*, vol. 284–286, pp.

295–302, 1998.

[53] S. Zajac, T. Siwecki, W. B. Hutchinson, and R. Lagneborg, “Strengthening mechanisms in vanadium microalloyed steels intended for long products,” *ISIJ Int.*, vol. 38, no. 10, pp. 1130–1139, 1998.

[54] T. Gladman, *The Physical Metallurgy of Microalloyed Steels*, 1st ed. Leeds: Maney Publishing, 1997.

[55] W. Roberts, “Recent Innovations in Alloy Design and Processing of Microalloyed Steels.,” in *ASM HSLA Steels Technology and Applications Conference*, 1983, pp. 1–33.

[56] T. N. Baker, “Titanium microalloyed steels,” *Iron Mak. Steel Mak.*, vol. 46, no. 1, pp. 1–55, 2019.

[57] L. J. Cuddy and J. C. Raley, “Austenite grain coarsening in microalloyed steels,” *Metall. Trans. A*, vol. 14, no. 10, pp. 1989–1995, 1983.

[58] W. J. Liu, S. Yue, and J. J. Jonas, “Characterization of Ti carbosulfide precipitation in Ti microalloyed steels,” *Metall. Trans. A*, vol. 20, no. 10, pp. 1907–1915, 1989.

[59] W. J. Liu, S. Yue, and J. J. Jonas, “Characterization of Ti carbosulfide precipitation in Ti microalloyed steels,” *Metall. Trans. A*, vol. 20, no. 10, pp. 1907–1915, 1989.

[60] M. I. Vega, S. F. Medina, M. Chapa, and A. Quispe, “Determination of critical temperatures (Tnr, Ar3, Ar1) in hot rolling of structural steels with different Ti and N contents,” *ISIJ Int.*, vol. 39, no. 12, pp. 1304–1310, 1999.

[61] D. Bai, R. Bodnar, S. Sanders, J. Ward, and J. Dorricott, “Development of discrete X80 line pipe plate at SSAB Americas,” in *International Symposium on the Recent Developments in Plate Steels*, 2011, pp. 13–22.

[62] F. Fletcher, “Meta-analysis of Tnr measurements: Determining new empirical models based on composition and strain,” in *Austenite Processing Symposium (Internal company presentation)*, 2008, pp. 1–14.

[63] F. Boratto, R. Barbosa, S. Yue, and J. J. Jonas, “Effect of chemical composition on critical temperatures of microalloyed steels,” in *International Conference on Physical Metallurgy of Thermomechanical Processing of Steels and Other Metals. THERMEC-88.*, 1988, pp. 383–390.

[64] C. N. Homsher, “Determination of the Non-recrystallization Temperature (TNR) in Multiple Microalloyed Steels,” 2013.

[65] A. I. Zaky, “Determinations of the non-recrystallization temperature for X52 steel produced by compact slab process combined with direct hot rolling,” *J. Mater. Eng. Perform.*, vol. 15, no. 6, pp. 651–655, 2006.

[66] J. Gautam, A. Miroux, J. Moerman, C. Barbatti, P. Van Liempt, and L. A. I. Kestens, "Determination of the non-recrystallisation temperature (Tnr) of austenite in high strength C-Mn steels," *Mater. Sci. Forum*, vol. 706–709, pp. 2722–2727, 2012.

[67] H. Yang, X. Zhou, Z. Liu, and G. Wang, "Determination of no-recrystallization temperature for a Nb-bearing steel," *J. Wuhan Univ. Technol. Mater. Sci. Ed.*, vol. 31, no. 3, pp. 644–647, 2016.

[68] D. Q. Bai, S. Yue, W. P. Sun, and J. J. Jonas, "Effect of deformation parameters on the no-recrystallization temperature in Nb-bearing steels," *Metall. Trans. A*, vol. 24, no. October, pp. 2151–2159, 1993.

[69] J. O. Andersson, T. Helander, L. Höglund, P. Shi, and B. Sundman, "Thermo-Calc & DICTRA, computational tools for materials science," *Calphad Comput. Coupling Phase Diagrams Thermochem.*, vol. 26, no. 2, pp. 273–312, 2002.

[70] S. Jin, Q. Chen, and J. Bratberg, "Thermodynamic Calculations and Precipitation Simulations of HSLA Steels," *HSLA Steels 2015, Microalloying 2015 Offshore Eng. Steels 2015 Conf. Proc.*, pp. 173–177, 2015.

[71] B. Sundman, B. Jansson, and J. O. Andersson, "The Thermo-Calc databank system," *Calphad*, vol. 9, no. 2, pp. 153–190, 1985.

[72] Thermo-Calc, "TCFE9: TCS Steel and Fe-alloys Database Extended Information," in *Thermo-Calc*, 2017, pp. 1–44.

[73] M. Mihaliková, K. Zgodavová, and A. Lišková, "Testing of Microalloyed Steel Quality under Creep Conditions for a New Intended Use," *Adv. Mater. Sci. Eng.*, vol. 2017, pp. 1–7, 2017.

[74] S. Akamatsu, Y. Matsumura, T. Senuma, H. Yada, and S. Ishikawa, "Modelling of NbC precipitation kinetics in hot deformed austenite on Nb bearing low carbon steels," *Tetsu-To-Hagane/Journal Iron Steel Inst. Japan*, 1989.

[75] F. Perrard, A. Deschamps, P. Maugis, P. Donnadieu, and F. Bley, "Characterization and Modeling of NbC Precipitation in Model Microalloyed Steels," in *Solid State Transformation and Heat Treatment*, 2005.

[76] S. W. Thompson and P. R. Howell, "Factors influencing ferrite/pearlite banding and origin of large pearlite nodules in a hypoeutectoid plate steel," *Mater. Sci. Technol. (United Kingdom)*, vol. 8, no. 9, pp. 777–784, 1992.

[77] Heiser FA and Hertzberg RW, "Structural control and fracture anisotropy of banded steel," *J Iron Steel Inst*, 1971.

[78] S. E. Offerman, N. H. Van Dijk, M. T. Rekveldt, J. Sietsma, and S. Van der Zwaag, "Ferrite/pearlite band formation in hot rolled medium carbon steel," *Mater. Sci. Technol.*, vol.

18, no. 3, pp. 297–303, 2002.

[79] J. Verhoeven, “Banding: Microsegregation-Induced,” *Encycl. Iron, Steel, Their Alloy.*, no. January 2000, pp. 320–330, 2016.

[80] R. Grossterlinden, R. Kawalla, U. Lotter, and H. Pircher, “Formation of pearlitic banded structures in ferritic-pearlitic steels,” *Steel Res.*, vol. 63, no. 8, pp. 331–336, 1992.

[81] A. S. Bor, “Effect of Pearlite Banding on Mechanical Properties of Hot-rolled Steel Plates,” *ISIJ Int.*, vol. 31, no. 12, pp. 1445–1446, 1991.

[82] G. Krauss, “Solidification, segregation, and banding in carbon and alloy steels,” *Metall. Mater. Trans. B*, vol. 34, no. 6, pp. 781–792, Dec. 2003.

[83] G. Krauss, *Steels - Processing, Structure, and Performance*, Second. USA: ASM International, 2015.

[84] T. F. Majka, D. K. Matlock, and G. Krauss, “Development of microstructural banding in low-alloy steel with simulated Mn segregation,” *Metall. Mater. Trans. A Phys. Metall. Mater. Sci.*, 2002.

[85] S. Seetharaman, *Fundamentals of Metallurgy*. Cambridge: Woodhead publishing, 2005.

[86] M. C. Flemmings, *Solidification Processing*. New York: McGraw-Hill, 1974.

[87] R. Abbaschian, L. Abbaschian, and R. E. Reed-Hill, *Physical Metallurgy Principles*, Fourth. Boston: Cengage Learning, 2009.

[88] J. W. Rutter and B. Chalmers, “a Prismatic Substructure Formed During Solidification of Metals,” *Can. J. Phys.*, vol. 31, no. 1, pp. 15–39, 1953.

[89] D. Walton, W. A. Tiller, J. W. Rutter, and W. C. Winegard, “Instability of a Smooth Solid-Liquid Interface During Solidification,” *J. Met.*, vol. 7, no. 9, pp. 1023–1026, 1955.

[90] W. A. Tiller, K. A. Jackson, J. W. Rutter, and B. Chalmers, “The redistribution of solute atoms during the solidification of metals,” *Acta Metall.*, vol. 1, no. 4, pp. 428–437, 1953.

[91] L. E. Samuels, *Light Microscopy of Carbon Steels*. 1999.

[92] J. D. Verhoeven, “Review of microsegregation induced banding phenomena in steels,” *J. Mater. Eng. Perform.*, vol. 9, no. 3, pp. 286–296, 2000.

[93] J. D. Verhoeven, “Genuine Damascus steel: A type of banded microstructure in hypereutectoid steels,” *Steel Res.*, vol. 73, no. 8, pp. 356–365, 2002.

[94] J. S. Kirkaldy, J. von Destinon-Forstmann, and R. J. Brigham, “Simulation of banding in steels,” *Can. Metall. Q.*, vol. 1, no. 1, pp. 59–81, 1962.

[95] J. A. Eckert, P. R. Howell, and S. W. Thompson, “Banding and the nature of large, irregular pearlite nodules in a hot-rolled low-alloy plate steel: A second report,” *J. Mater. Sci.*, vol. 28, no. 16, pp. 4412–4420, 1993.

[96] H. Farahani, W. Xu, and S. van der Zwaag, "A Novel Approach for Controlling the Band Formation in Medium Mn Steels," *Metall. Mater. Trans. A*, vol. 49, no. 6, pp. 1998–2010, Jun. 2018.

[97] S. Celotto, H. Ghadbeigi, C. Pinna, B. A. Shollock, and P. Efthymiadis, "Deformation-Induced Microstructural Banding in TRIP Steels," *Metall. Mater. Trans. A Phys. Metall. Mater. Sci.*, vol. 49, no. 7, pp. 2893–2906, 2018.

[98] F. A. Khalid, M. Farooque, A. Ul Haq, and A. Q. Khan, "Role of ferrite/pearlite banded structure and segregation on mechanical properties of microalloyed hot rolled steel," *Mater. Sci. Technol.*, vol. 15, no. 10, pp. 1209–1215, 1999.

[99] W. A. Spitzig and R. J. Sober, "Influence of Sulfide Inclusions and Pearlite Content on the Mechanical Properties of Hot-Rolled Carbon Steels," *Metall. Trans. A*, vol. 12A, no. 2, pp. 281–291, 1981.

[100] A. Siddiqui and N. Shaikh, "Effect of Ferrite-Pearlite Layering on Ductile to Brittle Transition Temperature of API-X60 Steel," *NED Univ. J. Res.*, vol. XIII, no. 2, pp. 15–23, 2017.

[101] J. Komenda and R. Sandström, "Assessment of pearlite banding using automatic image analysis: application to hydrogen-induced cracking," *Mater. Charact.*, vol. 31, no. 3, pp. 143–153, 1993.

[102] J. A. Ronevich, B. P. Somerday, and C. W. San Marchi, "Effects of microstructure banding on hydrogen assisted fatigue crack growth in X65 pipeline steels," *Int. J. Fatigue*, vol. 82, pp. 497–504, 2016.

[103] I. Moro, L. Briottet, P. Lemoine, E. Andrieu, C. Blanc, and G. Odemer, "Hydrogen embrittlement susceptibility of a high strength steel X80," *Mater. Sci. Eng. A*, vol. 527, no. 27–28, pp. 7252–7260, 2010.

[104] C. San Marchi, B. P. Somerday, K. A. Nibur, D. G. Stalheim, T. Boggess, and S. Jansto, "Fracture Resistance and Fatigue Crack Growth of X80 Pipeline Steel in Gaseous Hydrogen," in *ASME 2011 Pressure Vessels and Piping Conference: Volume 6, Parts A and B*, 2011, no. Table 1, pp. 841–849.

[105] A. A. Korda, Y. Mutoh, Y. Miyashita, T. Sadasue, and S. L. Mannan, "In situ observation of fatigue crack retardation in banded ferrite-pearlite microstructure due to crack branching," *Scr. Mater.*, vol. 54, no. 11, pp. 1835–1840, 2006.

[106] K. Minakawa, Y. Matsuo, and A. J. McEvily, "The influence of a duplex microstructure in steels on fatigue crack growth in the near-threshold region," *Fatigue Fract. Eng. Mater. Struct.*, vol. 13A, no. 1, pp. 439–445, Mar. 1982.

[107] R. M. Ramage, K. V. Jata, G. J. Shiflet, and E. A. Starke, "The effect of phase continuity on

the fatigue and crack closure behavior of a dual-phase steel," *Metall. Trans. A*, vol. 18, no. 7, pp. 1291–1298, Jul. 1987.

[108] D. S. MacKenzie and G. Graham, "Beer, blood and urine - Mythological quenchants of ancient blacksmiths," in *23rd International Federation of Heat Treatment and Surface Engineering Congress 2016, IFHTSE 2016*, 2016.

[109] V. B. Trindade, J. C. Payão-Filho, A. S. Guimarães, and R. P. R. Paranhos, "Effect of normalizing heat treatment on the mechanical behaviour of low-alloy steel weld metals," *Mater. Struct. Constr.*, vol. 38, no. 277, pp. 353–357, 2005.

[110] T. Pan, X. yang Chai, J. guang Wang, H. Su, and C. fu Yang, "Precipitation Behavior of V-N Microalloyed Steels during Normalizing," *J. Iron Steel Res. Int.*, vol. 22, no. 11, pp. 1037–1042, 2015.

[111] G. E. Totten, *Steel Heat Treatment Handbook*, Second Edi. New York: Taylor and Grancis Group, 2007.

[112] X. li Wen, Z. Mei, B. Jiang, L. chong Zhang, and Y. zheng Liu, "Effect of normalizing temperature on microstructure and mechanical properties of a Nb-V microalloyed large forging steel," *Mater. Sci. Eng. A*, vol. 671, pp. 233–243, 2016.

[113] V. I. Savran, S. E. Offerman, and J. Sietsma, "Austenite nucleation and growth observed on the level of individual grains by three-dimensional X-ray diffraction microscopy," *Metall. Mater. Trans. A Phys. Metall. Mater. Sci.*, vol. 41, no. 3, pp. 583–591, 2010.

[114] M. M. Souza, J. R. C. Guimarães, and K. K. Chawla, "Intercritical Austenitization of Two Fe-Mn-C Steels," *Metall. Trans. A*, vol. 13, no. 4, pp. 575–579, Apr. 1982.

[115] M. Avrami, "Kinetics of Phase Change. II Transformation-Time Relations for Random Distribution of Nuclei," *J. Chem. Phys.*, vol. 8, no. 2, pp. 212–224, Feb. 1940.

[116] E. B. Hawbolt, B. Chau, and J. K. Brimacombe, "Kinetics of Austenite-Pearlite Transformation in Eutectoid Carbon Steel," *Metall. Trans. A*, vol. 14A, no. 9, pp. 1803–1815, 1983.

[117] A. Chatterjee, D. Chakrabarti, A. Moitra, R. Mitra, and A. K. Bhaduri, "Effect of normalization temperatures on ductile–brittle transition temperature of a modified 9Cr–1Mo steel," *Mater. Sci. Eng. A*, vol. 618, pp. 219–231, Nov. 2014.

[118] B. Wang, H. M. Hu, and C. Zhou, "The Method of Eliminating Banded Structure and the Effects of Banded Structure on the Transverse Properties in 20G Steel," *Appl. Mech. Mater.*, vol. 347–350, pp. 1171–1175, Aug. 2013.

[119] T. D. Isfahani and H. Sharifi, "A Study on the Mechanical Properties of Dual Phase Steels Prepared by the Direct and Step Quenching Procedure," *Issi*, vol. 11, no. 2, pp. 28–33, 2014.

[120] A. Ghaheri, A. Shafyei, and M. Honarmand, “Effects of inter-critical temperatures on martensite morphology, volume fraction and mechanical properties of dual-phase steels obtained from direct and continuous annealing cycles,” *Mater. Des.*, vol. 62, pp. 305–319, Oct. 2014.

[121] R. C. Voigt, “Analysis of intercritical heat treatment of cast steels,” *J. Heat Treat.*, vol. 7, no. 2, pp. 95–105, 1989.

[122] N. Fonstein, *Advanced high strength sheet steels: Physical metallurgy, design, processing, and properties*. Springer US, 2015.

[123] R. Schneider, K. Steineder, D. Krizan, and C. Sommitsch, “Effect of the heat treatment on the microstructure and mechanical properties of medium-Mn-steels,” *Mater. Sci. Technol. (United Kingdom)*, vol. 35, no. 17, pp. 2045–2053, 2019.

[124] G. R. Speich, V. A. Demarest, and R. L. Miller, “Formation of Austenite During Intercritical Annealing of Dual-Phase Steels,” *Metall. Mater. Trans. A*, 1981.

[125] J. Huang, W. J. Poole, and M. Militzer, “Austenite formation during intercritical annealing,” *Metall. Mater. Trans. A Phys. Metall. Mater. Sci.*, vol. 35 A, no. 11, pp. 3363–3375, 2004.

[126] P. A. Wycliffe, G. R. Purdy, and J. D. Embury, “Growth of Austenite in the Intercritical Annealing of Fe-C-Mn Dual Phase Steels,” *Can. Metall. Q.*, vol. 20, no. 3, pp. 339–350, Jul. 1981.

[127] O. A. Girina, N. M. Fonstein, and D. Bhattacharya, “Effect of Annealing Parameters on Austenite Decomposition in a Continuously Annealed Dual-Phase Steel,” in *45th MWSP Conference Proceedings*, 2003, vol. XLI, pp. 403–414.

[128] H. Chen, B. Appolaire, and S. van der Zwaag, “Application of cyclic partial phase transformations for identifying kinetic transitions during solid-state phase transformations: Experiments and modeling,” *Acta Mater.*, vol. 59, no. 17, pp. 6751–6760, Oct. 2011.

[129] H. Chen and S. van der Zwaag, “The Effect of Interfacial Element Partitioning on Ferrite and Bainite Formation,” *JOM*, vol. 68, no. 5, pp. 1320–1328, May 2016.

[130] Y. S. Ahn, H. D. Kim, T. S. Byun, Y. J. Oh, G. M. Kim, and J. H. Hong, “Application of intercritical heat treatment to improve toughness of SA508 Cl.3 reactor pressure vessel steel,” *Nucl. Eng. Des.*, vol. 194, no. 2–3, pp. 161–177, 1999.

[131] J. Kang, C. Wang, and G. D. Wang, “Microstructural characteristics and impact fracture behavior of a high-strength low-alloy steel treated by intercritical heat treatment,” *Mater. Sci. Eng. A*, vol. 553, no. 11, pp. 96–104, 2012.

[132] P. O. Offor and B. A. Ezekoye, “Intercritical Heat Treatment Effects on Low Carbon Steels Quenched from Intermediate Temperature Austenitization,” *Niger. J. Technol.*, vol. 28, no.

2, pp. 39–47, 2012.

[133] G. Mukherjee, “Banding in wrought low alloy steel,” *Tool Alloy Steel*, vol. 11, no. 2, pp. 55–58, 1977.

[134] W. C. Leslie, *The Physical Metallurgy of Steels*, 1st ed. New York: McGraw-Hill College, 1981.

[135] B. K. Show, R. Veerababu, R. Balamuralikrishnan, and G. Malakondaiah, “Effect of vanadium and titanium modification on the microstructure and mechanical properties of a microalloyed HSLA steel,” *Mater. Sci. Eng. A*, vol. 527, no. 6, pp. 1595–1604, 2010.

[136] ASTM E3-11, “Standard guide for preparation of metallographic specimens,” *Am. Soc. Test. Mater. Int.*, pp. 1–12, 2017.

[137] G. F. Vander Voort, *Metallography: Principles and Practice*. New York: McGraw-Hill, 1984.

[138] A. Benscoter and M. Perricone, “Marshall’s Reagent: Origins, Modifications, and New Applications,” *Microsc. Microanal.*, vol. 11, no. S02, pp. 76–77, Aug. 2005.

[139] ASTM E112 − 13, “Standard Test Methods for Determining Average Grain Size,” *Am. Soc. Test. Mater. Int.*, no. Reapproved 2014, pp. 1–28, 2014.

[140] ASTM E 562-11, “Standard Test Method for Determining Volume Fraction by Systematic Manual Point Count,” *Am. Soc. Test. Mater. Int.*, no. Reapproved 2011, pp. 1–7, 2011.

[141] V. Sinha, E. J. Payton, M. Gonzales, R. A. Abrahams, and B. S. Song, “Delineation of Prior Austenite Grain Boundaries in a Low-Alloy High-Performance Steel,” *Metallogr. Microstruct. Anal.*, vol. 6, no. 6, pp. 610–618, 2017.

[142] ASTM A 1033-18, “Standard practice for quantitative measurement and reporting of hypoeutectoid carbon and low-alloy steel phase transformations,” *Am. Soc. Test. Mater. Int.*, pp. 1–14, 2018.

[143] M. Atkins, *Atlas of continuous cooling transformation diagrams for engineering steels*, Revised ed. Sheffield: ASM International, 1980.

[144] “What is Physical Simulation,” *Gleeble*, 2002. [Online]. Available: https://www.gleeble.com/index.php/resources/what-is-physical-simulation.html.

[145] V. Kumar, “Thermo-mechanical simulation using Gleeble system - Advantages and Limitations,” *J. Metall. Mater. Sci.*, vol. 58, no. 1, pp. 81–88, 2016.

[146] ASTM E23 − 16b, “Standard Test Methods for Notched Bar Impact Testing of Metallic Materials,” *Am. Soc. Test. Mater. Int.*, vol. i, pp. 1–26, 2009.

[147] ASTM E92 − 17, “Standard Test Methods for Vickers Hardness and Knoop Hardness of Metallic Materials,” *Am. Soc. Test. Mater. Int.*, pp. 1–27, 2017.

[148] ASTM E140 − 12b, "Standard Hardness Conversion Tables for Metals Relationship Among Brinell Hardness, Vickers Hardness, Rockwell Hardness, Superficial Hardness, Knoop Hardness, Scleroscope Hardness, and Leeb Hardness," *Am. Soc. Test. Mater.*, no. Reapproved, pp. 1–25, 2019.

[149] ASTM E8/E8M − 16a, "ASTM E8/E8M standard test methods for tension testing of metallic materials," *Am. Soc. Test. Mater. Int.*, no. C, pp. 1–30, 2016.

[150] ASTM A 370-17a, "Standard test methods and definitions for mechanical testing of steel products," *Am. Soc. Test. Mater. Int.*, pp. 1–50, 2014.

[151] T. Schambron *et al.*, "Thermomechanical processing of pipeline steels with a reduced Mn content," *ISIJ Int.*, vol. 49, no. 2, pp. 284–292, 2009.

[152] J. Rowe, *Advanced Materials in Automotive Engineering*, First. Woodhead publishing, 2012.

[153] M. R. Akbarpour and A. Ekrami, "Effect of ferrite volume fraction on work hardening behavior of high bainite dual phase (DP) steels," *Mater. Sci. Eng. A*, vol. 477, no. 1–2, pp. 306–310, 2008.

[154] G. E. Dieter, *Mechanical metallurgy*. New York,: McGraw-Hill, 1961.

[155] T. Xu, Y. Feng, Z. Jin, S. Song, and D. Wang, "Determination of the maximum strain-hardening exponent," *Mater. Sci. Eng. A*, vol. 550, pp. 80–86, 2012.

[156] J. Galán, L. Samek, P. Verleysen, K. Verbeken, and Y. Houbaert, "Advanced high strength steels for automotive industry," *Rev. Metal.*, vol. 48, no. 2, pp. 118–131, 2012.

[157] S355 European Standard Practice, "European Standard Steel," *Eur. Stand. Steel S355 EN 10025 2004 Stand. Struct. Steel Plate*, vol. 1, no. 7, pp. 1–7, 2004.

[158] ASTM A633/A633M − 18, "Standard Specification for Normalized High-Strength Low-Alloy Structural Steel Plates 1," *Am. Soc. Test. Mater. Int.*, pp. 18–20, 2019.

[159] ASTM International, "Standard Specification for Structural Steel with Low Yield to Tensile Ratio for Use in," *Annu. B. ASTM Stand.*, vol. 05, no. Reapproved 2018, pp. 6–8, 2013.

[160] J. Zhao, T. Lee, J. H. Lee, Z. Jiang, and C. S. Lee, "Effects of tungsten addition on the microstructure and mechanical properties of microalloyed forging steels," *Metall. Mater. Trans. A Phys. Metall. Mater. Sci.*, vol. 44, no. 8, pp. 3511–3523, 2013.

[161] J. Zhao, J. Hun Lee, Y. Woo Kim, Z. Jiang, and C. S. Lee, "Enhancing mechanical properties of a low-carbon microalloyed cast steel by controlled heat treatment," *Mater. Sci. Eng. A*, vol. 559, pp. 427–435, 2013.

[162] A. T. Davenport, L. C. Brossard, and R. E. Miner, "Precipitation in Microalloyed High-Strength Low-Alloy Steels.," *J Met*, vol. 27, no. 6, pp. 21–27, 1975.

[163] S. Serajzadeh and A. Karimi Taheri, "A study on austenite decomposition during continuous

cooling of a low carbon steel," *Mater. Des.*, vol. 25, no. 8, pp. 673–679, 2004.

[164] M. Umemoto, Z. H. Guo, and I. Tamura, "Effect of cooling rate on grain size of ferrite in a carbon steel," *Materials Science and Technology (United Kingdom)*, vol. 3, no. 4. pp. 249–255, 1987.

[165] S. Pallaspuro, S. Mehtonen, J. Kömi, Z. Zhang, and D. Porter, "Effects of local grain size and inclusions on the low-temperature toughness of low-carbon as-quenched martensite," *Mater. Sci. Eng. A*, vol. 743, pp. 611–622, 2019.

[166] C. I. Garcia and A. J. Deardo, "Formation of austenite in 1.5 pct Mn steels," *Metall. Trans. A*, vol. 12, no. 3, pp. 521–530, Mar. 1981.

[167] Y. Ohmori, "Isothermal decomposition of an Fe- C- B austenite," *Trans Iron Steel Inst Jap*, vol. 11, no. 5, pp. 339–348, 1971.

[168] M. Sarwar, E. Ahmad, K. A. Qureshi, and T. Manzoor, "Influence of epitaxial ferrite on tensile properties of dual phase steel," *Mater. Des.*, p. 335, 2007.

[169] P. I. Kambilinya, C. W. Siyasiya, K. M. Banks, and R. J. Mostert, "Effect of intercritical annealing of normalised Nb-Ti-V microalloyed plate steel on microstructural evolution," in *IOP Conf. Ser.: Mater. Sci. Eng. 655 012004*, 2019.

[170] S. Lu, S. Wei, Z. Liu, D. Li, and Y. Li, "Effects of Normalizing Process on the Microstructural Evolution and Mechanical Properties of Low Carbon Steel Weld Metal with Niobium Addition," *ISIJ Int.*, vol. 50, no. 2, pp. 248–254, 2010.

[171] T. Yamane, K. Hisayuki, Y. Kawazu, T. Takahashi, Y. Kimura, and S. Tsukuda, "Improvement of toughness of low carbon steels containing nitrogen by fine microstructures," *J. Mater. Sci.*, vol. 37, no. 18, pp. 3875–3879, 2002.

[172] S. Shanmugam, N. K. Ramisetti, R. D. K. Misra, J. Hartmann, and S. G. Jansto, "Microstructure and high strength-toughness combination of a new 700 MPa Nb-microalloyed pipeline steel," *Mater. Sci. Eng. A*, vol. 478, no. 1–2, pp. 26–37, 2008.

[173] R. W. K. Honeycombe, "Transformation From Austenite in Alloy Steels.," *Metall. Mater. Trans. A*, vol. 7A, no. 7, pp. 915–936, 1976.

[174] A. T. Davenport and P. C. Becker, "Interphase precipitation of cementite in a continuously-cooled plain-carbon steel," *Metall. Trans.*, vol. 2, no. 10, pp. 2962–2964, 1971.

[175] N. J. Petch, "The cleavage strength of polycrystals," *J. Iron Steel Res. Int.*, vol. 174, pp. 25–28, 1953.

[176] S. Wei and S. Lu, "Effects of multiple normalizing processes on the microstructure and mechanical properties of low carbon steel weld metal with and without Nb," *Mater. Des.*, vol. 35, pp. 43–54, 2012.

[177] R. J. McCabe, A. Misra, and T. E. Mitchell, “Experimentally determined content of a geometrically necessary dislocation boundary in copper,” *Acta Mater.*, vol. 52, no. 3, pp. 705–714, 2004.

[178] B. Hwang and C. G. Lee, “Influence of thermomechanical processing and heat treatments on tensile and Charpy impact properties of B and Cu bearing high-strength low-alloy steels,” *Mater. Sci. Eng. A*, vol. 527, no. 16–17, pp. 4341–4346, 2010.

[179] J. H. Chen and R. Cao, “Effects of Material Microstructure on Cleavage Fracture,” in *Micromechanism of Cleavage Fracture of Metals*, Elsevier Inc., 2015, pp. 241–270.

CHAPTER 8 APPENDIX A

8.1 A.1 Parameters for assessing the Degree of Banding

$\bar{N}_{L\perp}$: The mean number of feature interceptions per test line perpendicular to the rolling direction. This mean quantity gives a measure of the number of bands per unit length in μm.

$\bar{N}_{L\parallel}$: The mean number of feature interceptions per test line parallel to the rolling direction. This mean quantity gives a measure of the number of bands per unit length in μm.

AI: A ratio of $\bar{N}_{L\perp}$ to $\bar{N}_{L\parallel}$ that is used to measure the extent of microstructural banding, i.e., a non-banded or randomly oriented matrix will have an AI = 1, and a banded matrix AI > 1.

$SB_{\perp}$: This quantity measures the average distance from centre to centre of the banded phase.

$\lambda_{\perp}$: This quantity measures the average free path spacing of the bands from edge-to-edge and is a function of the volume fraction of the banded phase.

$SB_{\perp}$–$\lambda_{\perp}$: This is the difference between the mean spacing and the mean free path spacing. It gives the average width of the banded phase.

These parameters have been illustrated in **Error! Reference source not found.**.

95% confidence interval (95% CI);

$$95\%\ \text{CI} = \pm \frac{ts}{\sqrt{n}} \qquad 8.1$$

where, s is the standard deviation; t is a multiplier that is related to the number of field measurements, n, and therefore varies with the number of measurements; t – values can be obtained from "Table 2" in [25].

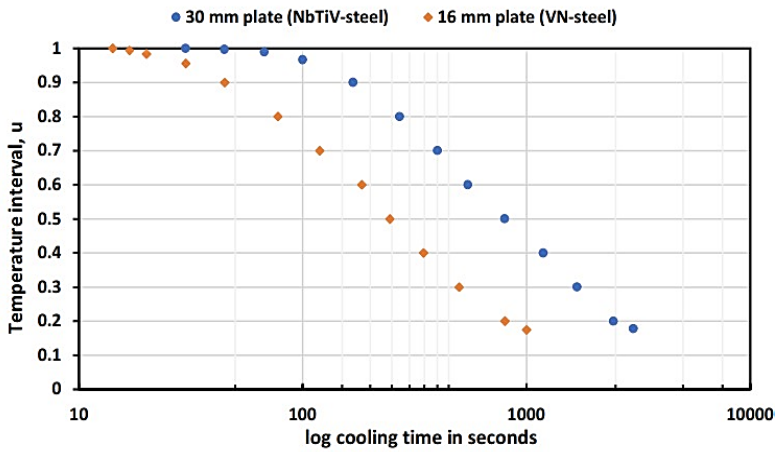
Percentage relative accuracy (% RA);

$$\%\ \text{RA} = \frac{95\%\ \text{CI}}{\bar{\text{X}}} \times 100; \quad \textit{where}, \bar{\text{X}} = \frac{(\bar{\text{N}}_{\text{L}\perp} + \bar{\text{N}}_{\text{L}\parallel})}{2} \qquad 8.2$$

The % RA value gives an approximation of the % error of each measurement as influenced by the field-to-field variability of the values; with the acceptable % RA being $\leq$ 30% [25].

8.2 A.2 Cooling profile excel template

Time, *s*	Temp. inter.	Temp. °C	Time, *s*	Temp. inter.	Temp. °C
30	1	775	14.1	1	775
44.7	0.9972	773	16.82	0.994	771
67.4	0.989	766	20	0.983	762
100	0.967	749	30	0.956	741
168.2	0.9	697.5	44.7	0.9	698
271.1	0.8	620	77.4	0.8	620
400	0.7	542.5	118.9	0.7	543
547.7	0.6	465	183.4	0.6	465
800	0.5	387.5	245	0.5	388
1189.2	0.4	310	346.4	0.4	310
1681.8	0.3	232.5	500	0.3	233
2449.5	0.2	155	800	0.2	155
3000	0.178	138	1000	0.174	135
16mm					
30mm		*775*			



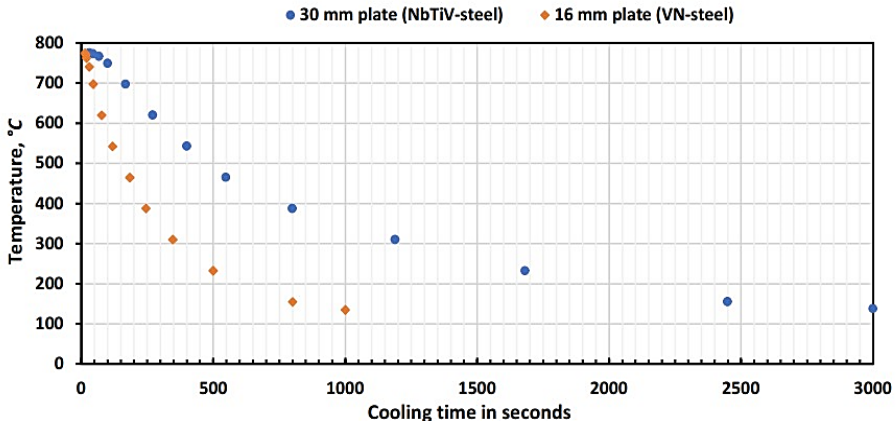


Figure 8.1: Templates for the simulated cooling profiles for the 30 mm thick by 2500 mm wide NbTiV-steel plate and the 16 mm thick by 2500 mm wide VN-steel plate. Cooling profiles generated from [143].

8.3 A.3 NbTiV-steel intercritical annealing Thermo-Calc predictions

SYSTEM

Moles	1	
Mass	55.31835873 [g]	
Temperature	**1013.15 [K]**	**740 [°C]**
Total Gibbs Energy	-45217.18759 [J]	
Enthalpy	25437.24673 [J]	
Volume	7.27066E-06 [m3]	

	Moles	Mass	Volume Fraction
BCC_A2#1	0.716079136	39.78047204	**0.721004725**

Composition Component	Mole Fraction	Mass Fraction
Fe	0.979521054	0.984701755
Mn	0.009900914	0.009791274
Si	0.008421154	0.00425748
Al	0.000834688	0.000405405
Cr	0.000225944	0.000211476
V	0.000202758	0.000185925
Ni	0.000170394	0.000180015
P	0.00032211	0.000179594
C	0.000400664	8.66264E-05
Nb	2.52072E-07	4.21559E-07
Ti	1.75212E-08	1.51011E-08
N	5.06307E-08	1.27659E-08
S	2.08812E-09	1.20529E-09

	Moles	Mass
FCC_A1#1	0.282257251	15.4753448

Composition Component	Mole Fraction	Mass Fraction
Fe	0.945753775	0.963346902
Mn	0.028146017	0.028202952
C	0.018266482	0.004001648
Si	0.006547971	0.003354296
Ni	0.00040255	0.000430912
Cr	0.000362492	0.000343774
Al	0.000317868	0.000156432
V	0.000133031	0.000123602
P	6.86546E-05	3.87857E-05
Nb	2.5871E-07	4.38391E-07
N	8.54693E-07	2.18353E-07
Ti	4.54915E-08	3.97273E-08
S	5.83395E-10	3.41202E-10

SYSTEM

Moles	1	
Mass	55.31835873 [g]	
Temperature	**1048.15 [K]**	**775 [°C]**
Total Gibbs Ener	-47692.51306 [J]	
Enthalpy	27401.1874 [J]	
Volume	7.26705E-06 [m3]	

	Moles	Mass	Volume Fraction
BCC_A2#1	0.566866084	31.48580425	**0.572052223**

Composition Component	Mole Fraction	Mass Fraction
Fe	0.979525703	0.984875575
Mn	0.009403298	0.009300766
Si	0.008683937	0.004391089
Al	0.000955721	0.00046427
V	0.000338857	0.000310778
Cr	0.000224019	0.00020971
P	0.000370819	0.000206788
Ni	0.000157148	0.00016605
C	0.000339442	7.34025E-05
Nb	8.99745E-07	1.50497E-06
Ti	4.10084E-08	3.53503E-08
N	1.09621E-07	2.76442E-08
S	6.3162E-09	3.64642E-09

	Moles	Mass	Volume Fraction
FCC_A1#1	0.431737	23.77813051	**0.426702286**

Composition Component	Mole Fractic	Mass Fraction
Fe	0.9568696	0.97027344
Mn	0.0224773	0.022421154
Si	0.0068463	0.003491295
C	0.0124559	0.002716414
Ni	0.0003395	0.000361735
Cr	0.0003205	0.000302613
Al	0.000395	0.000193515
V	0.0002015	0.000186363
P	9.225E-05	5.18831E-05
Nb	6.936E-07	1.1701E-06
N	1.456E-06	3.7029E-07
Ti	5.298E-08	4.60547E-08
S	1.91E-09	1.1122E-09

SYSTEM

Moles	1	
Mass	55.31835873 [g]	
Temperature	**1083.15 [K]**	**810 [°C]**
Total Gibbs Ener	-50230.67805 [J]	
Enthalpy	29255.53141 [J]	
Volume	7.25358E-06 [m3]	

	Moles	Mass	Volume Fraction
BCC_A2#1	0.314806787	17.4798927	**0.318830068**

Composition Component	Mole Fraction	Mass Fraction
Fe	0.979650472	0.98531779
Mn	0.008521361	0.008431156
Si	0.009101265	0.004603593
Al	0.001191164	0.00057883
V	0.000414248	0.000380043
P	0.000490391	0.000273555
Cr	0.000218201	0.00020433
Ni	0.000139125	0.000147053
C	0.00027047	5.85064E-05
Nb	2.98759E-06	4.99884E-06
Ti	9.35772E-08	8.06918E-08
N	2.04632E-07	5.16207E-08
S	1.76236E-08	1.01776E-08

	Moles	Mass	Volume Fraction
FCC_A1#1	0.683872714	37.78587133	**0.679987363**

Composition Component	Mole Fraction	Mass Fraction
Fe	0.965056551	0.975435252
Mn	0.018062132	0.01795923
Si	0.007330728	0.003726343
C	0.008075865	0.001755553
Ni	0.000280521	0.000297972
Cr	0.000288136	0.000271152
Al	0.000531087	0.00025935
V	0.000230937	0.000212915
P	0.000139874	7.84117E-05
Nb	1.90317E-06	3.20013E-06
N	2.18475E-06	5.53851E-07
Ti	7.44704E-08	6.45332E-08
S	5.7245E-09	3.32222E-09

Figure 8.2: NbTiV-steel Thermo-Calc predictions for the ferrite and austenite volume fractions at intercritical temperatures of 740, 775 and 810 °C respectively.

8.4 A.4 VN-steel intercritical annealing Thermo-Calc predictions

SYSTEM

Moles	1	
Mass	55.44731998	[g]
Temperature	**1013.15**	**[K]** **740 [°C]**
Total Gibbs Ene	-44540.70817	[J]
Enthalpy	26052.40629	[J]
Volume	7.27651E-06	[m3]

	Moles	Mass	Volume Fraction
BCC_A2#1	0.713021961	39.71191711	**0.717750716**

Composition		
Component	Mole Fraction	Mass Fraction
Fe	0.984670713	0.987354074
Mn	0.009885592	0.00975119
Si	0.003816882	0.001924778
Cr	0.000278128	0.000259655
V	0.000221082	0.00020221
Al	0.00041398	0.000200556
P	0.000268605	0.00014938
C	0.000370831	7.99718E-05
Ni	7.38872E-05	7.78602E-05
Nb	1.71752E-07	2.86502E-07
N	1.15935E-07	2.9157E-08
Ti	9.97009E-09	8.57108E-09
S	2.29999E-09	1.3242E-09

	Moles	Mass	Volume Fraction
FCC_A1#1	0.285369059	15.69004205	**0.28089549**

Composition		
Component	Mole Fraction	Mass Fraction
Fe	0.950660683	0.965624234
Mn	0.02829939	0.028276958
C	0.017111155	0.003738017
Si	0.002950238	0.001507057
Cr	0.000442469	0.000418442
Ni	0.000179554	0.000191665
V	0.000148808	0.000137872
Al	0.000148811	7.30286E-05
P	5.65344E-05	3.18488E-05
N	2.14948E-06	5.47596E-07
Nb	1.81898E-07	3.07365E-07
Ti	2.58326E-08	2.2496E-08
S	6.25329E-10	3.647E-10

SYSTEM

Moles	1	
Mass	55.44731998	[g]
Temperature	**1048.15**	**[K]** **775 [°C]**
Total Gibbs Ener	-47015.06743	[J]
Enthalpy	28094.82415	[J]
Volume	7.27159E-06	[m3]

	Moles	Mass	Volume Fraction
BCC_A2#1	0.54260843	30.21773583	**0.547526937**

Composition		
Component	Mole Fraction	Mass Fraction
Fe	0.984847201	0.987627832
Mn	0.009249369	0.00912451
Si	0.00397329	0.002003848
V	0.000480107	0.000439167
Cr	0.000273916	0.000255748
Al	0.000483253	0.000234139
P	0.000317177	0.00017641
Ni	6.70516E-05	7.06639E-05
C	0.000307611	6.63446E-05
Nb	7.50981E-07	1.25285E-06
N	2.45369E-07	6.17149E-08
Ti	2.26237E-08	1.94511E-08
S	7.09861E-09	4.08736E-09

	Moles	Mass	Volume Fraction
FCC_A1#1	0.456255712	25.19968587	**0.451510065**

Composition		
Component	Mole Fraction	Mass Fraction
Fe	0.962263002	0.97298652
Mn	0.022150481	0.022032775
C	0.011398615	0.002478817
Si	0.003084863	0.001568697
Cr	0.000388621	0.000365855
V	0.000294654	0.000271764
Ni	0.00014803	0.0001573
Al	0.000189621	9.26349E-05
P	7.79205E-05	4.36981E-05
Nb	5.99928E-07	1.00915E-06
N	3.56134E-06	9.03175E-07
Ti	2.94321E-08	2.55146E-08
S	2.09821E-09	1.21816E-09

SYSTEM

Moles	1	
Mass	55.44731998	[g]
Temperature	**1083.15**	**[K]** **810 [°C]**
Total Gibbs Ener	-49555.51835	[J]
Enthalpy	30057.6355	[J]
Volume	7.25473E-06	[m3]

	Moles	Mass	Volume Fraction
BCC_A2#1	0.237484371	13.22270358	**0.240602056**

Composition		
Component	Mole Fraction	Mass Fraction
Fe	0.985100374	0.988086814
Mn	0.008170245	0.008061627
Si	0.004263009	0.002150408
V	0.000886305	0.000810896
Al	0.000556363	0.000269617
P	0.000458916	0.000255297
Cr	0.000264005	0.000246545
Ni	5.76992E-05	6.08203E-05
C	0.000238748	5.15031E-05
Nb	3.77354E-06	6.29662E-06
N	4.97663E-07	1.25197E-07
Ti	4.5952E-08	3.95161E-08
S	2.033E-08	1.17084E-08

	Moles	Mass	Volume Fraction
FCC_A1#1	0.761733867	42.20735214	**0.75871202**

Composition		
Component	Mole Fraction	Mass Fraction
Fe	0.970803676	0.978467529
Mn	0.017309106	0.017161792
Si	0.003348977	0.001697529
C	0.007185961	0.001557683
V	0.000513379	0.000471977
Cr	0.00034606	0.000324741
Ni	0.00011844	0.000125452
Al	0.000236518	0.000115174
P	0.000129532	7.24087E-05
Nb	2.51355E-06	4.21451E-06
N	5.79366E-06	1.46458E-06
Ti	3.75292E-08	3.24294E-08
S	6.48642E-09	3.75375E-09

Figure 8.3: VN-steel Thermo-Calc predictions for the ferrite and austenite volume fractions at intercritical temperatures of 740, 775 and 810 °C respectively.

8.5 A.5 As-hot rolled ferrite grain size measurement templates

Steel Type: NbTiV-Steel

Near-Surface

FERRITE GRAIN SIZE MEASUREMENTS

	Vertical	Horizontal	Average
Test Line Length [µm]	127,000	173,000	150,000

	Line 1	Line 2	Line 3	Line 4	Line 5	Line 6	Line 7	Line 8	Line 9	Line 10	Line 11	Line 12	Line 13	Line 14	Line 15	Line 16	Line 17	Line 18	Line 19	Line 20
Number of Vertical Intercepts	64	50	58	61	47	58	59	63	58	57	65	62	64	59	61	45	48	52	52	61
Number of Horizontal Intercepts	78	71	64	78	79	70	73	67	58	67	62	77	80	70	74	64	70	62	70	64
Average Number of Intercepts	71	60.5	61	69.5	63	64	66	65	58	62	63.5	69.5	72	64.5	67.5	54.5	59	57	61	62.5
Ferrite Grain size [µm]	14.2	16.7	16.6	14.5	16.0	15.8	15.3	15.6	17.4	16.3	15.9	14.5	14.0	15.7	15.0	18.6	17.1	17.7	16.6	16.2

Average Ferrite Grain Size [µm]	16.0
Standard Deviation	1.2

FERRITE VOLUME FRACTION

Number of point counts	736
Total number of Grid points	1,092
Ferrite volume fraction	0.67

Qaurter-Thickness

FERRITE GRAIN SIZE MEASUREMENTS

	Vertical	Horizontal	Average
Test Line Length [µm]	127,000	173,000	150,000

	Line 1	Line 2	Line 3	Line 4	Line 5	Line 6	Line 7	Line 8	Line 9	Line 10	Line 11	Line 12	Line 13	Line 14	Line 15	Line 16	Line 17	Line 18	Line 19	Line 20
Number of Vertical Intercepts	35	39	40	46	46	46	44	41	46	50	37	36	44	48	43	46	43	44	42	50
Number of Horizontal Intercepts	59	60	54	48	46	60	61	60	64	52	55	60	55	49	61	54	55	51	53	50
Average Number of Intercepts	47	49.5	47	47	46	53	52.5	50.5	55	51	46	48	49.5	48.5	52	50	49	47.5	47.5	50
Ferrite Grain size [µm]	21.0	19.9	21.0	21.0	21.4	18.6	18.8	19.5	17.9	19.3	21.4	20.5	19.9	20.3	19.0	19.7	20.1	20.8	20.8	19.7

Average Ferrite Grain Size [µm]	20.0
Standard Deviation	0.98

FERRITE VOLUME FRACTION

Number of point counts	284
Total number of Grid points	432
Ferrite volume fraction	0.66

Mid-Thickness

FERRITE GRAIN SIZE MEASUREMENTS

	Vertical	Horizontal	Average
Test Line Length [µm]	127,000	173,000	150,000

	Line 1	Line 2	Line 3	Line 4	Line 5	Line 6	Line 7	Line 8	Line 9	Line 10	Line 11	Line 12	Line 13	Line 14	Line 15	Line 16	Line 17	Line 18	Line 19	Line 20
Number of Vertical Intercepts	52	59	42	37	57	54	62	52	58	56	52	38	49	52	43	48	53	55	42	45
Number of Horizontal Intercepts	39	66	62	54	54	45	63	59	57	61	50	48	36	39	42	46	54	55	44	46
Average Number of Intercepts	45.5	62.5	52	45.5	55.5	49.5	62.5	55.5	57.5	58.5	51	43	42.5	45.5	42.5	47	53.5	55	43	45.5
Ferrite Grain size [µm]	23.1	16.8	20.2	23.1	19.0	21.3	16.8	19.0	18.3	18.0	20.6	24.5	24.8	23.1	24.8	22.4	19.7	19.1	24.5	23.1

Average Ferrite Grain Size [µm]	21.1
Standard Deviation	2.7

FERRITE VOLUME FRACTION

Number of point counts	379
Total number of Grid points	540
Ferrite volume fraction	0.70

Steel Type: VN-Steel

Near-Surface

FERRITE GRAIN SIZE MEASUREMENTS

	Vertical	Horizontal	Average
Test Line Length [µm]	127,000	173,000	150,000

	Line 1	Line 2	Line 3	Line 4	Line 5	Line 6	Line 7	Line 8	Line 9	Line 10	Line 11	Line 12	Line 13	Line 14	Line 15	Line 16	Line 17	Line 18	Line 19	Line 20
Number of Vertical Intercepts	68	66	65	65	69	72	70	67	64	67	55	61	63	54	57	60	55	70	64	79
Number of Horizontal Intercepts	86	88	82	78	73	83	78	78	85	74	84	72	71	67	72	78	77	63	75	63
Average Number of Intercepts	77	77	73.5	71.5	71	77.5	74	72.5	74.5	70.5	69.5	66.5	67	60.5	64.5	69	66	66.5	69.5	71
Ferrite Grain size [µm]	13.2	13.2	13.8	14.2	14.3	13.1	13.7	14.0	13.6	14.4	14.6	15.3	15.1	16.8	15.7	14.7	15.4	15.3	14.6	14.3

Average Ferrite Grain Size [µm]	14.5
Standard Deviation	0.9

FERRITE VOLUME FRACTION MEASUREMENTS

Number of point counts	334
Total number of Grid points	494
Ferrite volume fraction	0.68

Qaurter-Thickness

FERRITE GRAIN SIZE MEASUREMENTS

	Vertical	Horizontal	Average
Test Line Length [µm]	127,000	173,000	150,000

	Line 1	Line 2	Line 3	Line 4	Line 5	Line 6	Line 7	Line 8	Line 9	Line 10	Line 11	Line 12	Line 13	Line 14	Line 15	Line 16	Line 17	Line 18	Line 19	Line 20
Number of Vertical Intercepts	54	55	55	54	46	58	50	55	55	46	42	61	47	50	59	58	54	53	50	52
Number of Horizontal Intercepts	71	55	62	60	52	51	62	58	57	62	52	68	60	55	59	69	68	54	59	70
Average Number of Intercepts	62.5	55	58.5	57	49	54.5	56	56.5	56	54	47	64.5	53.5	52.5	59	63.5	61	53.5	54.5	61
Ferrite Grain size [µm]	14.6	16.6	15.6	16.0	18.6	16.7	16.3	16.1	16.3	16.9	19.4	14.1	17.0	17.4	15.4	14.3	14.9	17.0	16.7	14.9

Average Ferrite Grain Size [µm]	16.2
Standard Deviation	1.3

FERRITE VOLUME FRACTION MEASUREMENTS

Number of point counts	328
Total number of Grid points	540
Ferrite volume fraction	0.61

Mid-Thickness

FERRITE GRAIN SIZE MEASUREMENTS

	Vertical	Horizontal	Average
Test Line Length [µm]	127,000	173,000	150,000

	Line 1	Line 2	Line 3	Line 4	Line 5	Line 6	Line 7	Line 8	Line 9	Line 10	Line 11	Line 12	Line 13	Line 14	Line 15	Line 16	Line 17	Line 18	Line 19	Line 20
Number of Vertical Intercepts	51	58	57	50	57	55	49	56	53	67	57	49	52	55	63	55	50	53	51	55
Number of Horizontal Intercepts	49	62	56	62	72	40	66	58	55	67	56	59	64	63	61	43	57	57	57	66
Average Number of Intercepts	50	60	56.5	56	64.5	47.5	57.5	57	54	67	56.5	54	58	59	62	49	53.5	55	54	60.5
Ferrite Grain size [µm]	19.6	16.3	17.3	17.5	15.2	20.6	17.0	17.2	18.1	14.6	17.3	18.1	16.9	16.6	15.8	20.0	18.3	17.8	18.1	16.2

Average Ferrite Grain Size [µm]	17.4
Standard Deviation	1.5

FERRITE VOLUME FRACTION MEASUREMENTS

Number of point counts	352
Total number of Grid points	540
Ferrite volume fraction	0.65

Figure 8.4: Showing the NbTiV and VN calculation templates that were used in the determination of ferrite grain sizes and volume fractions.

8.6 A.6 VN-steel pearlite volume fraction by thresholding

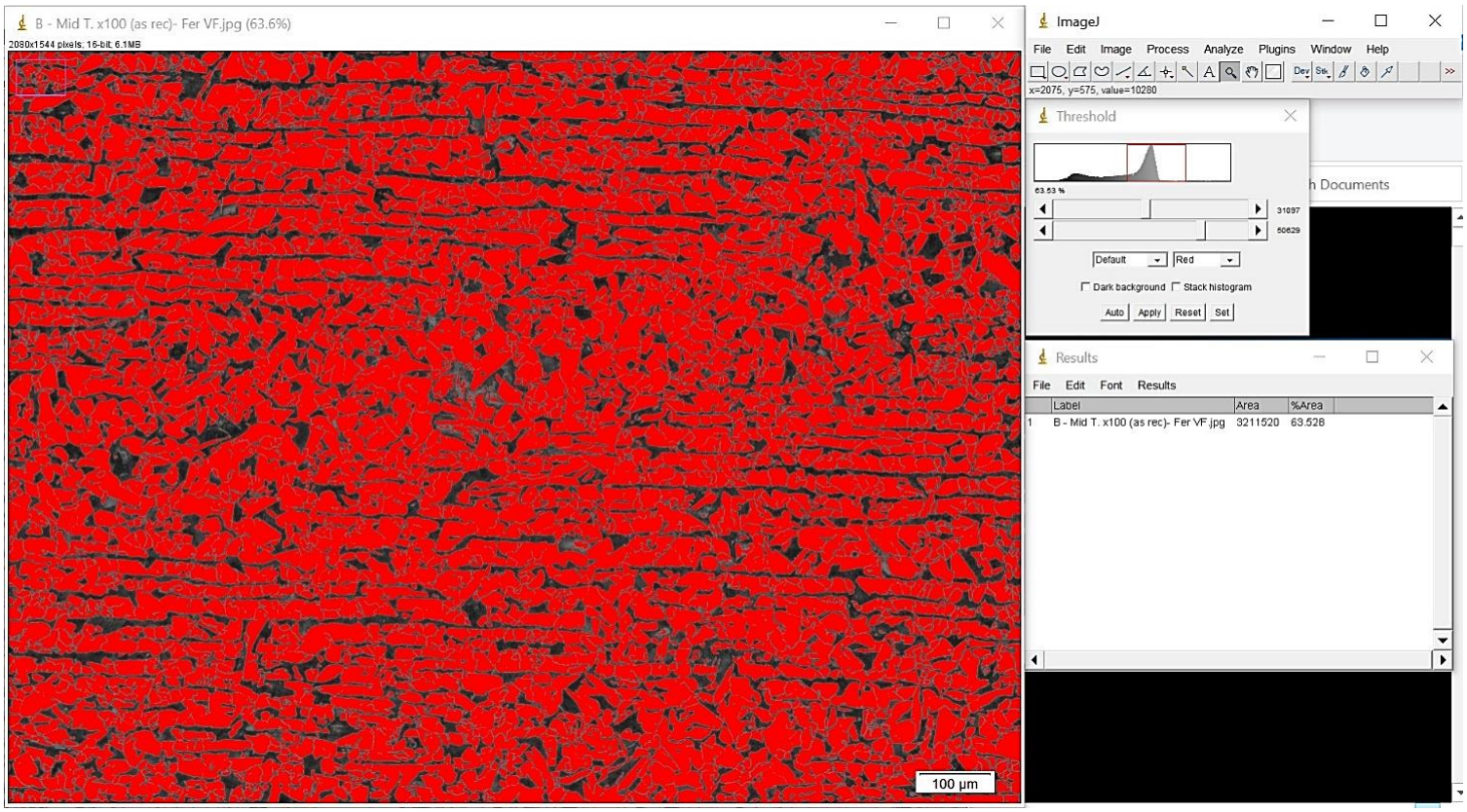


Figure 8.5: An illustration of the volume fraction estimation through thresholding procedure in ImageJ Software©. VN-steel microstructure, Mid-thickness. 2% Nital etch.

8.7 A.7 Prior austenite grain size measurement templates

NbTiV-Steel	L, *mm*	L, *μm*	N	Av. Gs, *μm*	SD	V, *μm*	150,000.0	Nv	Nh	Av.
965 Near S	199.7	199,653.7	38.0	26.3	3.4	H, *um*	180,000.0	36	40	38
	199.7	199,653.7	34.5	28.9		D1 , *um*	234,307.5	30	39	34.5
	199.7	199,653.7	43.5	22.9		D2 , *um*	234,307.5	40	47	43.5
	199.7	199,653.7	39.0	25.6		Av.	199,653.7	42	36	39
	199.7	199,653.7	34.0	29.4				35	33	34
	199.7	199,653.7	39.0	25.6				38	40	39
	199.7	199,653.7	36.0	27.7				32	40	36
	199.7	199,653.7	36.5	27.3				40	33	36.5
	199.7	199,653.7	41.5	24.1				43	40	41.5
	199.7	199,653.7	40.0	25.0				43	37	40
	199.7	199,653.7	28.0	35.7				27	29	28
	199.7	199,653.7	35.5	28.1				30	41	35.5
	199.7	199,653.7	31.5	31.7				33	30	31.5
Av.	*199.7*	*199,653.7*	*36.7*	*27.6*						

985 Near S	L, *mm*	L, *um*	N	Av. Gs, *um*	SD	V, *um*	150,000.0	Nv	Nh	Av.
	199.7	199,653.7	36.5	27.3	2.0	H, *um*	180,000.0	32	41	36.5
	199.7	199,653.7	34.0	29.4		D1 , *um*	234,307.5	33	35	34
	199.7	199,653.7	32.0	31.2		D2 , *um*	234,307.5	34	30	32
	199.7	199,653.7	35.0	28.5		Av.	199,653.7	36	34	35
	199.7	199,653.7	36.5	27.3				36	37	36.5
	199.7	199,653.7	34.0	29.4				34	34	34
	199.7	199,653.7	33.5	29.8				30	37	33.5
	199.7	199,653.7	33.0	30.3				32	34	33
	199.7	199,653.7	31.5	31.7				30	33	31.5
	199.7	199,653.7	31.0	32.2				33	29	31
	199.7	199,653.7	29.5	33.8				29	30	29.5
	199.7	199,653.7	36.0	27.7				34	38	36
	199.7	199,653.7	31.5	31.7				33	30	31.5
Av.	*199.7*	*199,653.7*	*33.4*	*30.0*						

965 Quarter T	L, *mm*	L, *um*	N	Av. Gs, *um*	SD	V, *um*	140,000.0	Nv	Nh	Av.
	187.6	187,613.6	33.5	28.0	1.4	H, *um*	170,000.0	30	37	33.5
	187.6	187,613.6	35.0	26.8		D1 , *um*	220,227.2	40	30	35
	187.6	187,613.6	35.0	26.8		D2 , *um*	220,227.2	32	38	35
	187.6	187,613.6	31.5	29.8		Av.	187,613.6	30	33	31.5
	187.6	187,613.6	30.5	30.8				30	31	30.5
	187.6	187,613.6	33.5	28.0				31	36	33.5
	187.6	187,613.6	31.5	29.8				30	33	31.5
	187.6	187,613.6	34.0	27.6				31	37	34
	187.6	187,613.6	35.0	26.8				30	40	35
	187.6	187,613.6	34.0	27.6				35	33	34
	187.6	187,613.6	36.0	26.1				28	44	36
	187.6	187,613.6	32.5	28.9				33	32	32.5
	187.6	187,613.6	35.0	26.8				37	33	35
Av.	*187.6*	*187,613.6*	*33.6*	*28.0*						

985 Quarter T	L, *mm*	L, *um*	N	Av. Gs, *um*	SD	V, *um*	150,000.0	Nv	Nh	Av.
	199.7	199,653.7	34.5	28.9	1.6	H, *um*	180,000.0	38	31	34.5
	199.7	199,653.7	33.5	29.8		D1 , *um*	234,307.5	30	37	33.5
	199.7	199,653.7	35.5	28.1		D2 , *um*	234,307.5	37	34	35.5
	199.7	199,653.7	31.5	31.7		Av.	199,653.7	30	33	31.5
	199.7	199,653.7	32.5	30.7				32	33	32.5
	199.7	199,653.7	34.0	29.4				33	35	34
	199.7	199,653.7	33.5	29.8				37	30	33.5
	199.7	199,653.7	29.5	33.8				29	30	29.5
	199.7	199,653.7	30.0	33.3				29	31	30
	199.7	199,653.7	32.0	31.2				31	33	32
	199.7	199,653.7	33.0	30.3				32	34	33
	199.7	199,653.7	31.5	31.7				30	33	31.5
	199.7	199,653.7	32.5	30.7				34	31	32.5
Av.	*199.7*	*199,653.7*	*32.6*	*30.7*						

965 Mid T	L, *mm*	L, *um*	N	Av. Gs, *um*	SD	V, *um*	140,000.0	Nv	Nh	Av.
	181.3	181,301.5	32.5	27.9	1.3	H, *um*	160,000.0	35	30	32.5
	181.3	181,301.5	29.5	30.7		D1 , *um*	212,602.9	29	30	29.5
	181.3	181,301.5	33.0	27.5		D2 , *um*	212,602.9	38	28	33
	181.3	181,301.5	31.0	29.2		Av.	181,301.5	35	27	31
	181.3	181,301.5	32.5	27.9				35	30	32.5
	181.3	181,301.5	30.5	29.7				24	37	30.5
	181.3	181,301.5	33.5	27.1				38	29	33.5
	181.3	181,301.5	30.0	30.2				28	32	30
	181.3	181,301.5	31.0	29.2				33	29	31
	181.3	181,301.5	32.0	28.3				33	31	32
	181.3	181,301.5	30.5	29.7				38	23	30.5
	181.3	181,301.5	30.5	29.7				37	24	30.5
	181.3	181,301.5	29.0	31.3				25	33	29
Av.	*181.3*	*181,301.5*	*31.2*	*29.1*						

985 Mid T	L, *mm*	L, *um*	N	Av. Gs, *um*	SD	V, *um*	129,000.0	Nv	Nh	Av.
	184.1	184,051.7	30.5	30.2	1.8	H, *um*	174,000.0	32	29	30.5
	184.1	184,051.7	29.0	31.7		D1 , *um*	216,603.3	28	30	29
	184.1	184,051.7	30.0	30.7		D2 , *um*	216,603.3	28	32	30
	184.1	184,051.7	26.5	34.7		Av.	184,051.7	25	28	26.5
	184.1	184,051.7	30.0	30.7				27	33	30
	184.1	184,051.7	29.5	31.2				30	29	29.5
	184.1	184,051.7	32.5	28.3				33	32	32.5
	184.1	184,051.7	31.0	29.7				29	33	31
	184.1	184,051.7	29.0	31.7				26	32	29
	184.1	184,051.7	28.0	32.9				30	26	28
	184.1	184,051.7	27.5	33.5				28	27	27.5
	184.1	184,051.7	30.0	30.7				29	31	30
	184.1	184,051.7	27.5	33.5				25	30	27.5
Av.	*184.1*	*184,051.7*	*29.3*	*31.5*						

1005 Near S	L, *mm*	L, *um*	N	Av. Gs, *um*	SD	V, *um*	170,000.0	Nv	Nh	Av.
	217.5	217,475.5	32.0	34.0	1.2	H, *um*	190,000.0	29	35	32
	217.5	217,475.5	32.0	34.0		D1 , *um*	254,951.0	34	30	32
	217.5	217,475.5	31.5	34.5		D2 , *um*	254,951.0	32	31	31.5
	217.5	217,475.5	31.0	35.1		Av.	217,475.5	33	29	31
	217.5	217,475.5	31.0	35.1				30	32	31
	217.5	217,475.5	33.0	33.0				32	34	33
	217.5	217,475.5	33.5	32.5				34	33	33.5
	217.5	217,475.5	31.0	35.1				33	29	31
	217.5	217,475.5	35.0	31.1				32	38	35
	217.5	217,475.5	31.5	34.5				28	35	31.5
	217.5	217,475.5	33.5	32.5				36	31	33.5
	217.5	217,475.5	31.5	34.5				33	30	31.5
	217.5	217,475.5	32.5	33.5				35	30	32.5
Av.	*217.5*	*217,475.5*	*32.2*	*33.8*						

1005 Quarter T	L, *mm*	L, *um*	N	Av. Gs, *um*	SD	V, *um*	177,000.0	Nv	Nh	Av.
	221.6	221,585.5	33.0	33.6	1.8	H, *um*	190,000.0	37	29	33
	221.6	221,585.5	35.0	31.7		D1 , *um*	259,670.9	40	30	35
	221.6	221,585.5	31.5	35.2		D2 , *um*	259,670.9	33	30	31.5
	221.6	221,585.5	34.5	32.1		Av.	221,585.5	33	36	34.5
	221.6	221,585.5	36.5	30.4				36	37	36.5
	221.6	221,585.5	33.0	33.6				36	30	33
	221.6	221,585.5	33.5	33.1				29	38	33.5
	221.6	221,585.5	33.0	33.6				38	28	33
	221.6	221,585.5	32.0	34.6				35	29	32
	221.6	221,585.5	33.5	33.1				34	33	33.5
	221.6	221,585.5	38.0	29.2				39	37	38
	221.6	221,585.5	36.5	30.4				40	33	36.5
	221.6	221,585.5	34.5	32.1				35	34	34.5
Av.	*221.6*	*221,585.5*	*34.2*	*32.5*						

1005 Mid T	L, *mm*	L, *um*	N	Av. Gs, *um*	SD	V, *um*	177,000.0	Nv	Nh	Av.
	221.6	221,585.5	32.5	34.1	1.4	H, *um*	190,000.0	32	33	32.5
	221.6	221,585.5	30.5	36.3		D1 , *um*	259,670.9	31	30	30.5
	221.6	221,585.5	29.0	38.2		D2 , *um*	259,670.9	27	31	29
	221.6	221,585.5	30.5	36.3		Av.	221,585.5	34	27	30.5
	221.6	221,585.5	30.0	36.9				28	32	30
	221.6	221,585.5	31.0	35.7				32	30	31
	221.6	221,585.5	30.0	36.9				32	28	30
	221.6	221,585.5	30.0	36.9				33	27	30
	221.6	221,585.5	30.0	36.9				34	26	30
	221.6	221,585.5	33.0	33.6				31	35	33
	221.6	221,585.5	32.0	34.6				31	33	32
	221.6	221,585.5	30.0	36.9				30	30	30
	221.6	221,585.5	29.5	37.6				31	28	29.5
Av.	*221.6*	*221,585.5*	*30.6*	*36.2*						

1050 Near S	L, *mm*	L, *um*	N	Av. Gs, *um*	SD	V, *um*	177,000.0	Nv	Nh	Av.
	221.6	221,585.5	35.0	31.7	1.6	H, *um*	190,000.0	35	35	35
	221.6	221,585.5	33.0	33.6		D1 , *um*	259,670.9	36	30	33
	221.6	221,585.5	31.5	35.2		D2 , *um*	259,670.9	33	30	31.5
	221.6	221,585.5	32.5	34.1		Av.	221,585.5	32	33	32.5
	221.6	221,585.5	34.0	32.6				35	33	34
	221.6	221,585.5	30.5	36.3				31	30	30.5
	221.6	221,585.5	34.0	32.6				32	36	34
	221.6	221,585.5	33.5	33.1				34	33	33.5
	221.6	221,585.5	35.5	31.2				28	43	35.5
	221.6	221,585.5	32.0	34.6				32	32	32
	221.6	221,585.5	32.0	34.6				34	30	32
	221.6	221,585.5	32.5	34.1				32	33	32.5
	221.6	221,585.5	35.5	31.2				36	35	35.5
Av.	*221.6*	*221,585.5*	*33.2*	*33.4*						

1050 Quarter T	L, *mm*	L, *um*	N	Av. Gs, *um*	SD	V, *um*	177,000.0	Nv	Nh	Av.
	221.6	221,585.5	31.5	35.2	1.2	H, *um*	190,000.0	32	31	31.5
	221.6	221,585.5	34.0	32.6		D1 , *um*	259,670.9	36	32	34
	221.6	221,585.5	31.5	35.2		D2 , *um*	259,670.9	33	30	31.5
	221.6	221,585.5	34.0	32.6		Av.	221,585.5	36	32	34
	221.6	221,585.5	31.0	35.7				32	30	31
	221.6	221,585.5	31.5	35.2				33	30	31.5
	221.6	221,585.5	33.0	33.6				35	31	33
	221.6	221,585.5	33.0	33.6				33	33	33
	221.6	221,585.5	32.0	34.6				34	30	32
	221.6	221,585.5	31.0	35.7				32	30	31
	221.6	221,585.5	32.5	34.1				32	33	32.5
	221.6	221,585.5	34.0	32.6				33	35	34
	221.6	221,585.5	33.0	33.6				30	36	33
Av.	*221.6*	*221,585.5*	*32.5*	*34.2*						

1050 Mid T	L, *mm*	L, *um*	N	Av. Gs, *um*	SD	V, *um*	177,000.0	Nv	Nh	Av.
	221.6	221,585.5	32.5	34.1	0.7	H, *um*	190,000.0	32	33	32.5
	221.6	221,585.5	30.5	36.3		D1 , *um*	259,670.9	31	30	30.5
	221.6	221,585.5	32.0	34.6		D2 , *um*	259,670.9	32	32	32
	221.6	221,585.5	32.5	34.1		Av.	221,585.5	33	32	32.5
	221.6	221,585.5	32.5	34.1				32	33	32.5
	221.6	221,585.5	32.0	34.6				33	31	32
	221.6	221,585.5	31.5	35.2				31	32	31.5
	221.6	221,585.5	32.5	34.1				32	33	32.5
	221.6	221,585.5	32.5	34.1				33	32	32.5
	221.6	221,585.5	32.0	34.6				32	32	32
	221.6	221,585.5	33.0	33.6				33	33	33
	221.6	221,585.5	32.5	34.1				32	33	32.5
	221.6	221,585.5	31.5	35.2				32	31	31.5
Av.	*221.6*	*221,585.5*	*32.1*	*34.5*						

Figure 8.6: NbTiV-steel prior austenite grain size measurement excel templates. Measurements were taken at near-surface, quarter-thickness and mid-thickness. Austenitising temperature has also been included in the templates.

VN-Steel	L, *mm*	L, *µm*	N	Av. Gs, *µm*	SD	V, *µm*	170,000.0	Nv	Nh	Av.
965 Near S	217.5	217,475.5	40.0	27.2	1.1	H, *µm*	190,000.0	40	40	40
	217.5	217,475.5	43.0	25.3		D1 , *µm*	254,951.0	42	44	43
	217.5	217,475.5	41.0	26.5		D2 , *µm*	254,951.0	41	41	41
	217.5	217,475.5	40.0	27.2		Av.	217,475.5	40	40	40
	217.5	217,475.5	40.5	26.8				38	43	40.5
	217.5	217,475.5	38.0	28.6				37	39	38
	217.5	217,475.5	42.5	25.6				44	41	42.5
	217.5	217,475.5	40.5	26.8				39	42	40.5
	217.5	217,475.5	39.0	27.9				40	38	39
	217.5	217,475.5	38.0	28.6				39	37	38
	217.5	217,475.5	38.0	28.6				37	39	38
	217.5	217,475.5	42.0	25.9				42	42	42
	217.5	217,475.5	40.0	27.2				41	39	40
Av.	*217.5*	*217,475.5*	*40.2*	*27.1*						
965 Quarter T	L, *mm*	L, *µm*	N	Av. Gs, *µm*	SD	V, *µm*	177,000.0	Nv	Nh	Av.
	221.6	221,585.5	38.5	28.8	1.0	H, *um*	190,000.0	39	38	38.5
	221.6	221,585.5	42.0	26.4		D1 , *um*	259,670.9	47	37	42
	221.6	221,585.5	39.5	28.0		D2 , *um*	259,670.9	39	40	39.5
	221.6	221,585.5	37.5	29.5		Av.	221,585.5	40	35	37.5
	221.6	221,585.5	39.0	28.4				42	36	39
	221.6	221,585.5	37.5	29.5				40	35	37.5
	221.6	221,585.5	37.5	29.5				40	35	37.5
	221.6	221,585.5	39.0	28.4				41	37	39
	221.6	221,585.5	39.5	28.0				43	36	39.5
	221.6	221,585.5	40.5	27.4				39	42	40.5
	221.6	221,585.5	38.5	28.8				37	40	38.5
	221.6	221,585.5	39.0	28.4				43	35	39
	221.6	221,585.5	41.0	27.0				47	35	41
Av.	*221.6*	*221,585.5*	*39.2*	*28.3*						
965 Mid T	L, *mm*	L, *µm*	N	Av. Gs, *µm*	SD	V, *µm*	177,000.0	Nv	Nh	Av.
	221.6	221,585.5	39.0	28.4	0.8	H, *um*	190,000.0	37	41	39
	221.6	221,585.5	36.0	30.8		D1 , *um*	259,670.9	35	37	36
	221.6	221,585.5	38.5	28.8		D2 , *um*	259,670.9	40	37	38.5
	221.6	221,585.5	37.5	29.5		Av.	221,585.5	36	39	37.5
	221.6	221,585.5	39.0	28.4				41	37	39
	221.6	221,585.5	37.0	29.9				39	35	37
	221.6	221,585.5	38.5	28.8				39	38	38.5
	221.6	221,585.5	37.0	29.9				38	36	37
	221.6	221,585.5	37.5	29.5				40	35	37.5
	221.6	221,585.5	37.5	29.5				38	37	37.5
	221.6	221,585.5	38.0	29.2				40	36	38
	221.6	221,585.5	36.0	30.8				36	36	36
	221.6	221,585.5	38.5	28.8				41	36	38.5
Av.	*221.6*	*221,585.5*	*37.7*	*29.4*						

985 Near S	L, *mm*	L, *µm*	N	Av. Gs, *µm*	SD	V, *µm*	170,000.0	Nv	Nh	Av.
	217.5	217,475.5	31.0	35.1	1.4	H, *um*	190,000.0	31	31	31
	217.5	217,475.5	31.0	35.1		D1 , *um*	254,951.0	35	27	31
	217.5	217,475.5	33.5	32.5		D2 , *um*	254,951.0	37	30	33.5
	217.5	217,475.5	33.5	32.5		Av.	217,475.5	36	31	33.5
	217.5	217,475.5	32.5	33.5				33	32	32.5
	217.5	217,475.5	35.0	31.1				30	40	35
	217.5	217,475.5	32.0	34.0				37	27	32
	217.5	217,475.5	34.0	32.0				33	35	34
	217.5	217,475.5	34.0	32.0				33	35	34
	217.5	217,475.5	32.5	33.5				30	35	32.5
	217.5	217,475.5	35.0	31.1				37	33	35
	217.5	217,475.5	31.5	34.5				32	31	31.5
	217.5	217,475.5	32.5	33.5				30	35	32.5
Av.	*217.5*	*217,475.5*	*32.9*	*33.1*						
985 Quarter T	L, *mm*	L, *µm*	N	Av. Gs, *µm*	SD	V, *µm*	177,000.0	Nv	Nh	Av.
	221.6	221,585.5	33.0	33.6	1.5	H, *um*	190,000.0	34	32	33
	221.6	221,585.5	39.0	28.4		D1 , *um*	259,670.9	36	42	39
	221.6	221,585.5	34.5	32.1		D2 , *um*	259,670.9	35	34	34.5
	221.6	221,585.5	33.0	33.6		Av.	221,585.5	37	29	33
	221.6	221,585.5	35.5	31.2				34	37	35.5
	221.6	221,585.5	34.5	32.1				39	30	34.5
	221.6	221,585.5	35.0	31.7				36	34	35
	221.6	221,585.5	35.0	31.7				41	29	35
	221.6	221,585.5	34.5	32.1				42	27	34.5
	221.6	221,585.5	35.0	31.7				37	33	35
	221.6	221,585.5	38.5	28.8				35	42	38.5
	221.6	221,585.5	36.5	30.4				39	34	36.5
	221.6	221,585.5	35.0	31.7				37	33	35
Av.	*221.6*	*221,585.5*	*35.3*	*31.5*						
985 Mid T	L, *mm*	L, *µm*	N	Av. Gs, *µm*	SD	V, *µm*	177,000.0	Nv	Nh	Av.
	221.6	221,585.5	33.0	33.6	1.7	H, *um*	190,000.0	36	30	33
	221.6	221,585.5	31.0	35.7		D1 , *um*	259,670.9	33	29	31
	221.6	221,585.5	32.0	34.6		D2 , *um*	259,670.9	34	30	32
	221.6	221,585.5	32.0	34.6		Av.	221,585.5	36	28	32
	221.6	221,585.5	32.5	34.1				35	30	32.5
	221.6	221,585.5	35.0	31.7				33	37	35
	221.6	221,585.5	31.0	35.7				32	30	31
	221.6	221,585.5	34.0	32.6				37	31	34
	221.6	221,585.5	34.5	32.1				37	32	34.5
	221.6	221,585.5	34.0	32.6				29	39	34
	221.6	221,585.5	37.0	29.9				36	38	37
	221.6	221,585.5	32.0	34.6				35	29	32
	221.6	221,585.5	32.5	34.1				30	35	32.5
Av.	*221.6*	*221,585.5*	*33.1*	*33.5*						

1050 Near S	L, mm	L, um	N	Av. Gs, um	SD	V, um	177,000.0	Nv	Nh	Av.
	221.6	221,585.5	35.0	31.7	1.6	H, um	190,000.0	35	35	35
	221.6	221,585.5	33.0	33.6		D1 , um	259,670.9	36	30	33
	221.6	221,585.5	31.5	35.2		D2 , um	259,670.9	33	30	31.5
	221.6	221,585.5	32.5	34.1		Av.	221,585.5	32	33	32.5
	221.6	221,585.5	34.0	32.6				35	33	34
	221.6	221,585.5	30.5	36.3				31	30	30.5
	221.6	221,585.5	34.0	32.6				32	36	34
	221.6	221,585.5	33.5	33.1				34	33	33.5
	221.6	221,585.5	35.5	31.2				28	43	35.5
	221.6	221,585.5	32.0	34.6				32	32	32
	221.6	221,585.5	32.0	34.6				34	30	32
	221.6	221,585.5	32.5	34.1				32	33	32.5
	221.6	221,585.5	35.5	31.2				36	35	35.5
Av.	221.6	221,585.5	33.2	33.4						

1050 Near S	L, mm	L, um	N	Av. Gs, um	SD	V, um	170,000.0	Nv	Nh	Av.
	217.5	217,475.5	28.5	38.2	1.7	H, um	190,000.0	27	30	28.5
	217.5	217,475.5	26.5	41.0		D1 , um	254,951.0	30	23	26.5
	217.5	217,475.5	26.0	41.8		D2 , um	254,951.0	27	25	26
	217.5	217,475.5	29.5	36.9		Av.	217,475.5	29	30	29.5
	217.5	217,475.5	28.0	38.8				28	28	28
	217.5	217,475.5	30.5	35.7				32	29	30.5
	217.5	217,475.5	28.5	38.2				27	30	28.5
	217.5	217,475.5	29.0	37.5				29	29	29
	217.5	217,475.5	28.5	38.2				30	27	28.5
	217.5	217,475.5	28.0	38.8				29	27	28
	217.5	217,475.5	27.0	40.3				26	28	27
	217.5	217,475.5	27.5	39.5				28	27	27.5
	217.5	217,475.5	28.5	38.2				29	28	28.5
Av.	217.5	217,475.5	28.2	38.7						

1050 Quarter T	L, mm	L, um	N	Av. Gs, um	SD	V, um	177,000.0	Nv	Nh	Av.
	221.6	221,585.5	31.5	35.2	1.2	H, um	190,000.0	32	31	31.5
	221.6	221,585.5	34.0	32.6		D1 , um	259,670.9	36	32	34
	221.6	221,585.5	31.5	35.2		D2 , um	259,670.9	33	30	31.5
	221.6	221,585.5	34.0	32.6		Av.	221,585.5	36	32	34
	221.6	221,585.5	31.0	35.7				32	30	31
	221.6	221,585.5	31.5	35.2				33	30	31.5
	221.6	221,585.5	33.0	33.6				35	31	33
	221.6	221,585.5	33.0	33.6				33	33	33
	221.6	221,585.5	32.0	34.6				34	30	32
	221.6	221,585.5	31.0	35.7				32	30	31
	221.6	221,585.5	32.5	34.1				32	33	32.5
	221.6	221,585.5	34.0	32.6				33	35	34
	221.6	221,585.5	33.0	33.6				30	36	33
Av.	221.6	221,585.5	32.5	34.2						

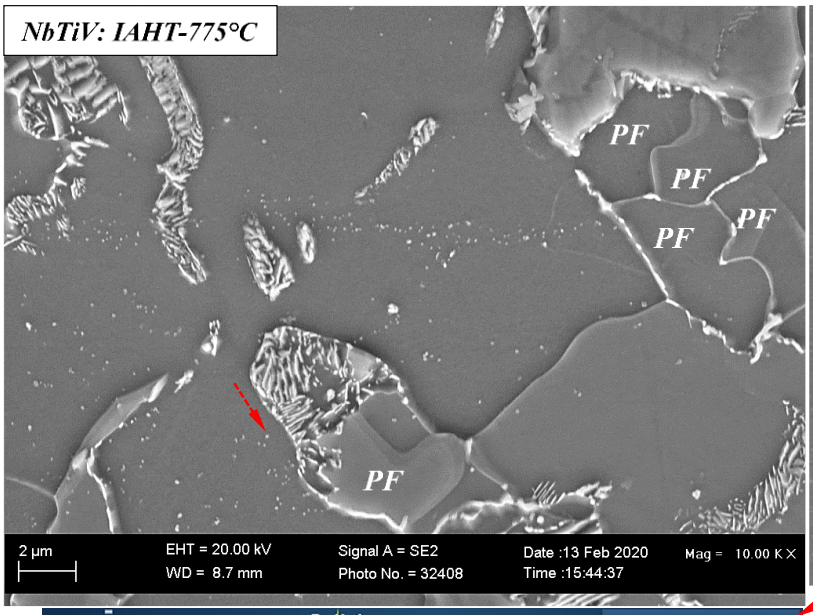
1050 Quarter T	L, mm	L, um	N	Av. Gs, um	SD	V, um	177,000.0	Nv	Nh	Av.
	221.6	221,585.5	30.0	36.9	1	H, um	190,000.0	30	30	30
	221.6	221,585.5	32.0	34.6		D1 , um	259,670.9	32	32	32
	221.6	221,585.5	30.5	36.3		D2 , um	259,670.9	29	32	30.5
	221.6	221,585.5	32.0	34.6		Av.	221,585.5	35	29	32
	221.6	221,585.5	32.5	34.1				32	33	32.5
	221.6	221,585.5	31.0	35.7				33	29	31
	221.6	221,585.5	31.5	35.2				33	30	31.5
	221.6	221,585.5	29.5	37.6				30	29	29.5
	221.6	221,585.5	29.0	38.2				31	27	29
	221.6	221,585.5	31.5	35.2				32	31	31.5
	221.6	221,585.5	30.5	36.3				28	33	30.5
	221.6	221,585.5	30.5	36.3				30	31	30.5
	221.6	221,585.5	32.0	34.6				33	31	32
Av.	221.6	221,585.5	31.0	35.8						

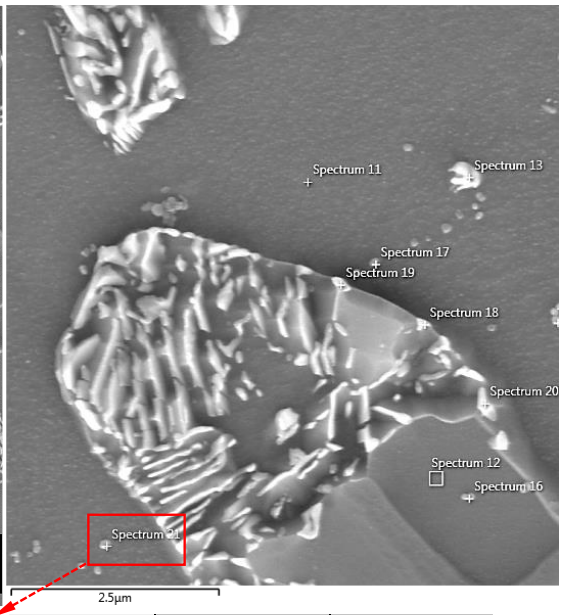
1050 Mid T	L, mm	L, um	N	Av. Gs, um	SD	V, um	177,000.0	Nv	Nh	Av.
	221.6	221,585.5	32.5	34.1	0.7	H, um	190,000.0	32	33	32.5
	221.6	221,585.5	30.5	36.3		D1 , um	259,670.9	31	30	30.5
	221.6	221,585.5	32.0	34.6		D2 , um	259,670.9	32	32	32
	221.6	221,585.5	32.5	34.1		Av.	221,585.5	33	32	32.5
	221.6	221,585.5	32.5	34.1				32	33	32.5
	221.6	221,585.5	32.0	34.6				33	31	32
	221.6	221,585.5	31.5	35.2				31	32	31.5
	221.6	221,585.5	32.5	34.1				32	33	32.5
	221.6	221,585.5	32.5	34.1				33	32	32.5
	221.6	221,585.5	32.0	34.6				32	32	32
	221.6	221,585.5	33.0	33.6				33	33	33
	221.6	221,585.5	32.5	34.1				32	33	32.5
	221.6	221,585.5	31.5	35.2				32	31	31.5
Av.	221.6	221,585.5	32.1	34.5						

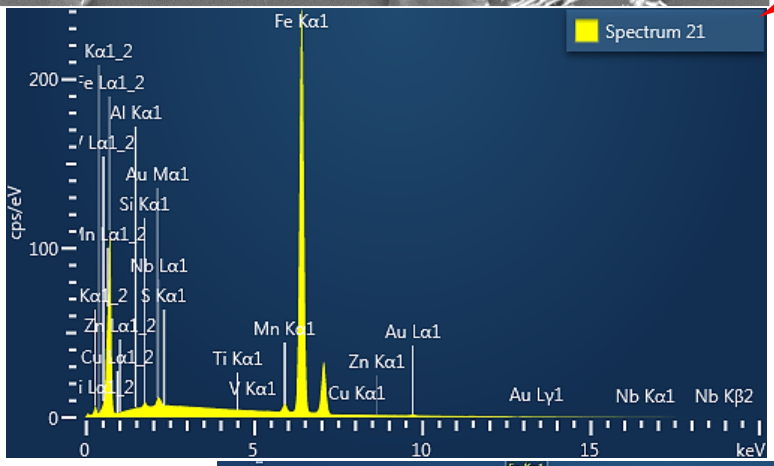
1050 Mid T	L, mm	L, um	N	Av. Gs, um	SD	V, um	170,000.0	Nv	Nh	Av.
	217.5	217,475.5	24.5	44.4	1.0	H, um	190,000.0	27	22	24.5
	217.5	217,475.5	25.0	43.5		D1 , um	254,951.0	23	27	25
	217.5	217,475.5	24.5	44.4		D2 , um	254,951.0	20	29	24.5
	217.5	217,475.5	25.0	43.5		Av.	217,475.5	23	27	25
	217.5	217,475.5	24.0	45.3				22	26	24
	217.5	217,475.5	24.0	45.3				25	23	24
	217.5	217,475.5	25.0	43.5				27	23	25
	217.5	217,475.5	24.5	44.4				22	27	24.5
	217.5	217,475.5	25.5	42.6				28	23	25.5
	217.5	217,475.5	24.0	45.3				22	26	24
	217.5	217,475.5	23.5	46.3				22	25	23.5
	217.5	217,475.5	24.5	44.4				30	19	24.5
	217.5	217,475.5	24.0	45.3				23	25	24
Av.	217.5	217,475.5	24.5	44.5						

Figure 8.7: VN-steel prior austenite grain size measurement excel templates. Measurements were taken at near-surface, quarter-thickness and mid-thickness. Austenitising temperature has also been included in the templates.

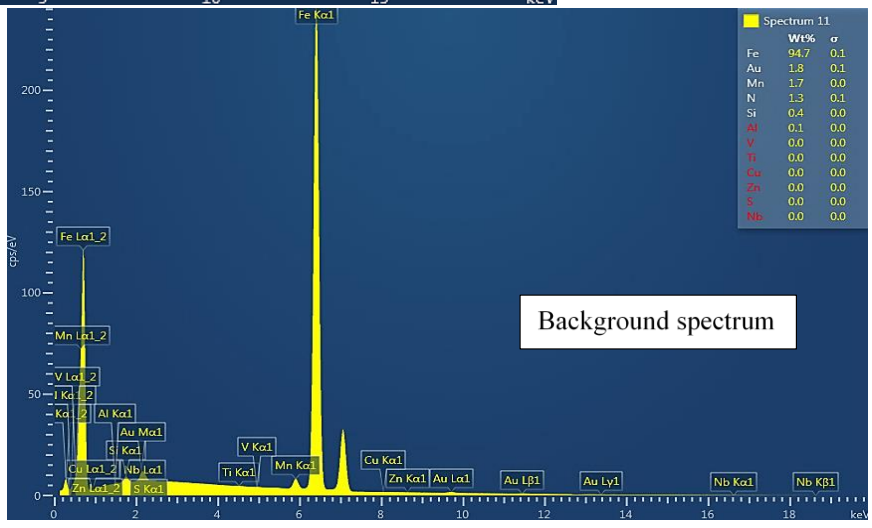
8.8 A.8 SEM-EDS Spectra precipitate analysis after heat treatment



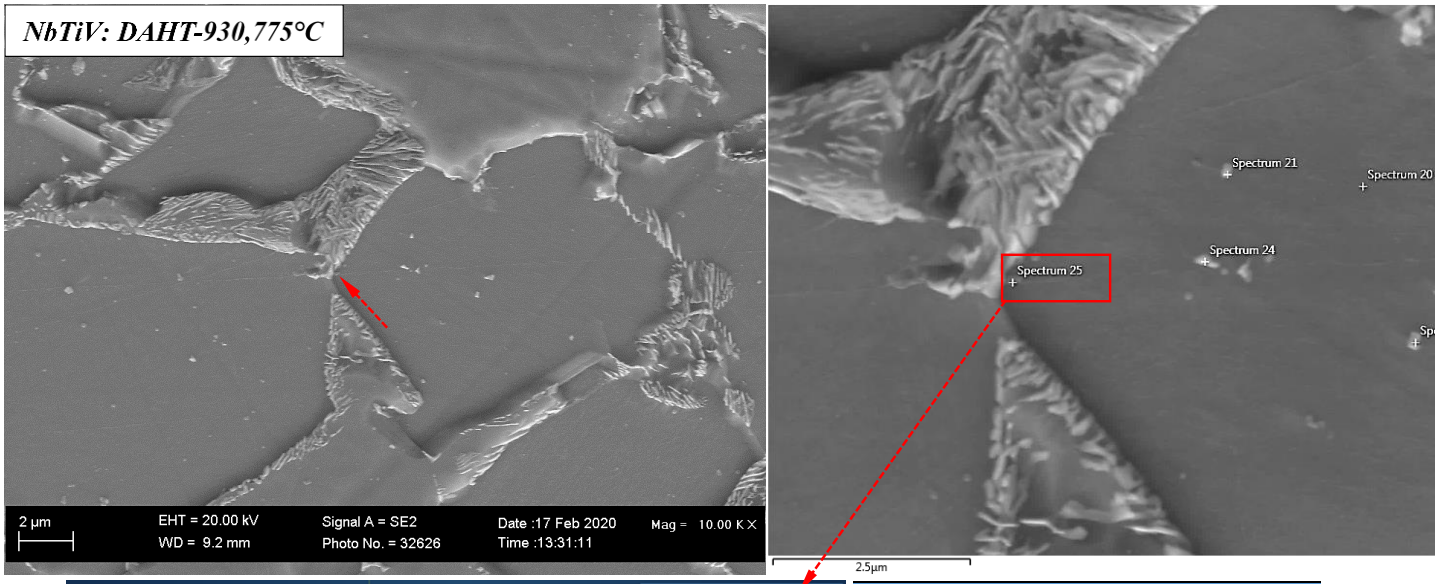


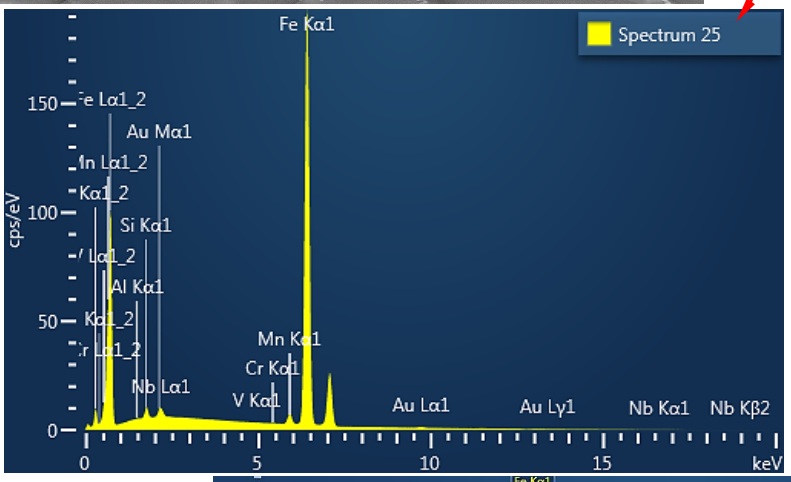


Element	Wt%	Wt% Sigma
N	1.42	0.12
Al	0.08	0.01
Si	0.39	0.01
Ti	0.02	0.01
V	0.04	0.01
Mn	1.74	0.02
Fe	94.36	0.13
Cu	0.03	0.02
Nb	0.02	0.04
Au	1.91	0.05
Total:	**100.00**	

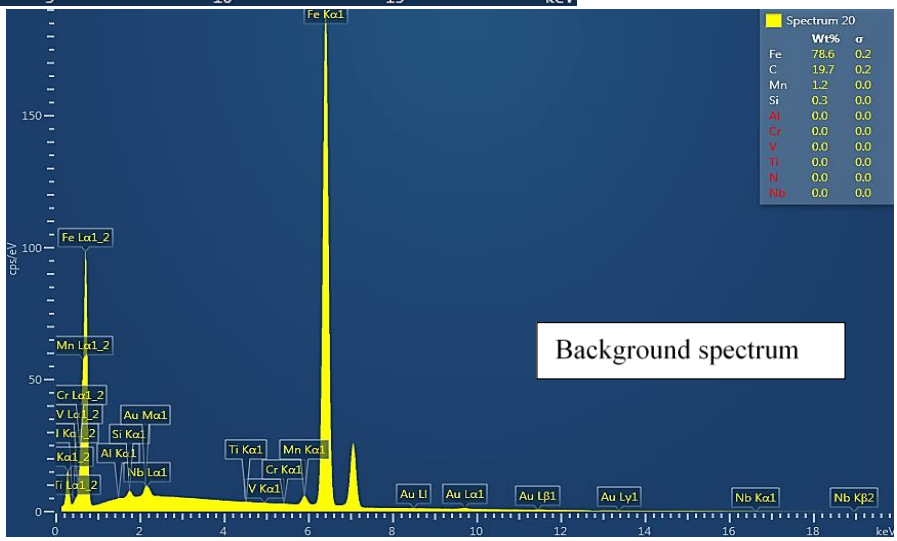


(a)

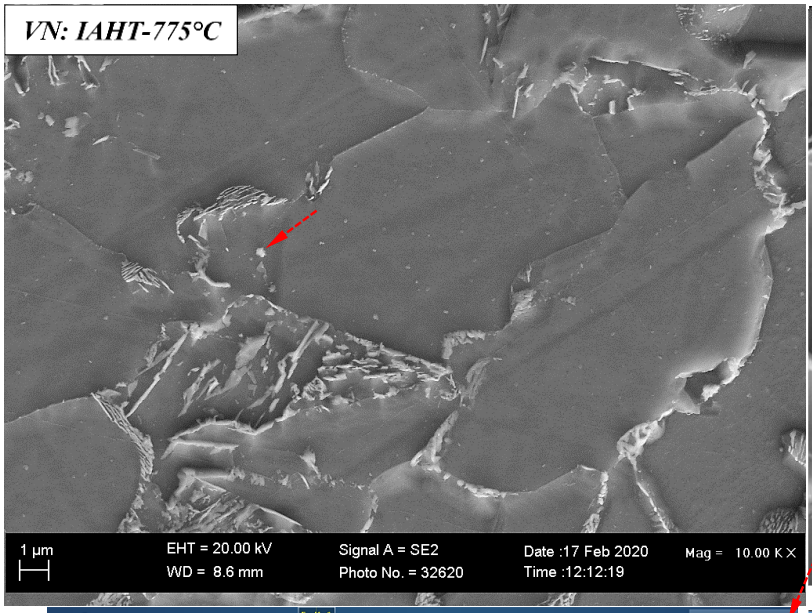


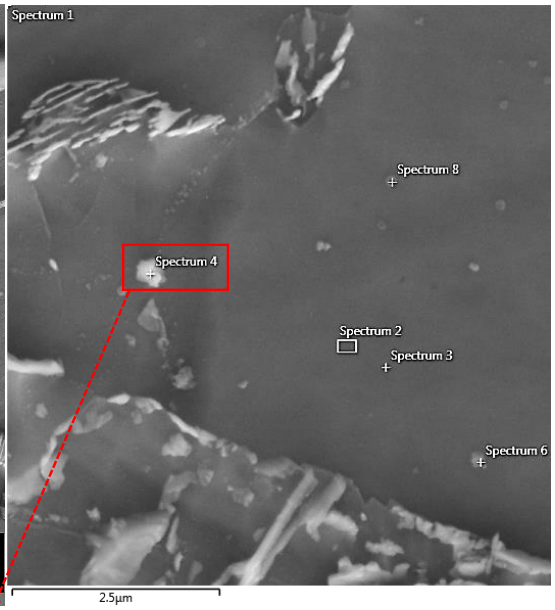


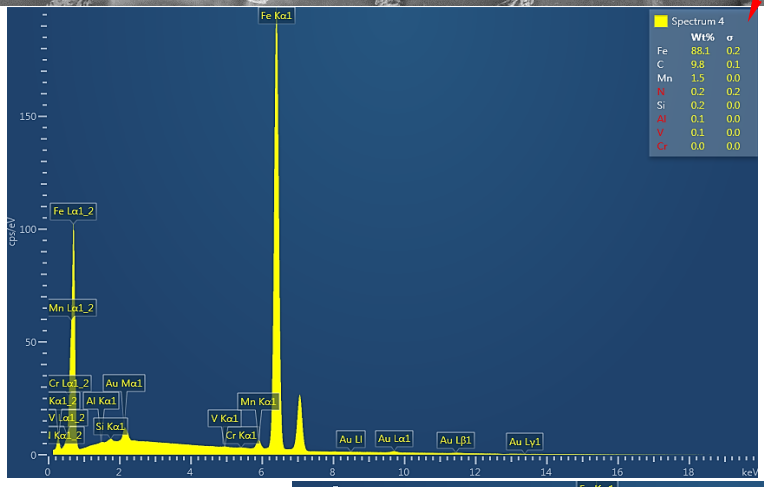
Element	Wt%	Wt% Sigma
C	13.77	0.18
N	1.07	0.18
Al	0.05	0.01
Si	0.74	0.01
V	0.02	0.01
Cr	0.04	0.01
Mn	1.80	0.02
Fe	82.51	0.23
Nb	0.00	0.00
Total:	**100.00**	



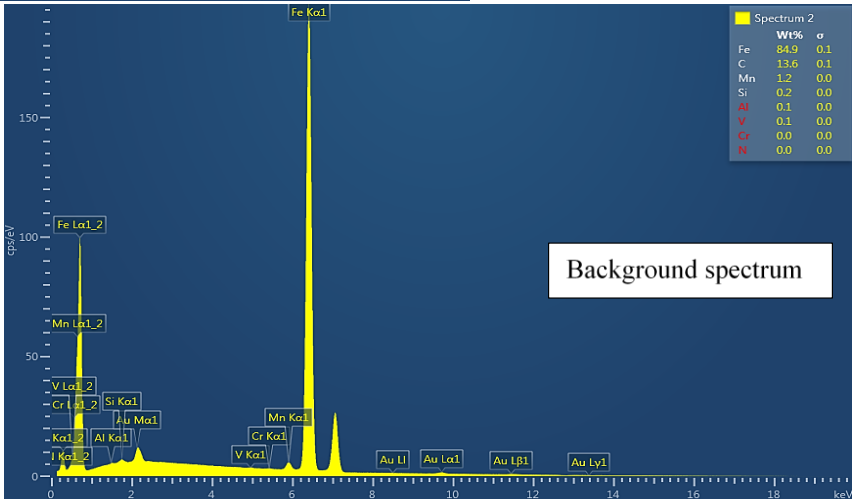
(b)



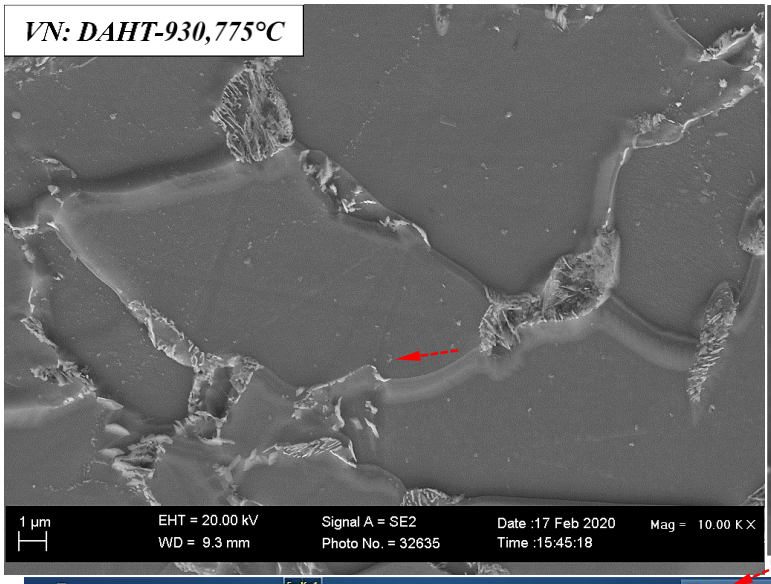


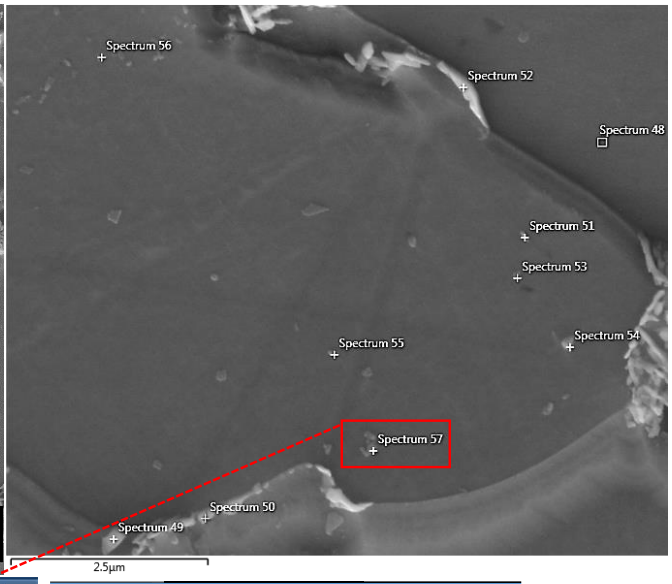


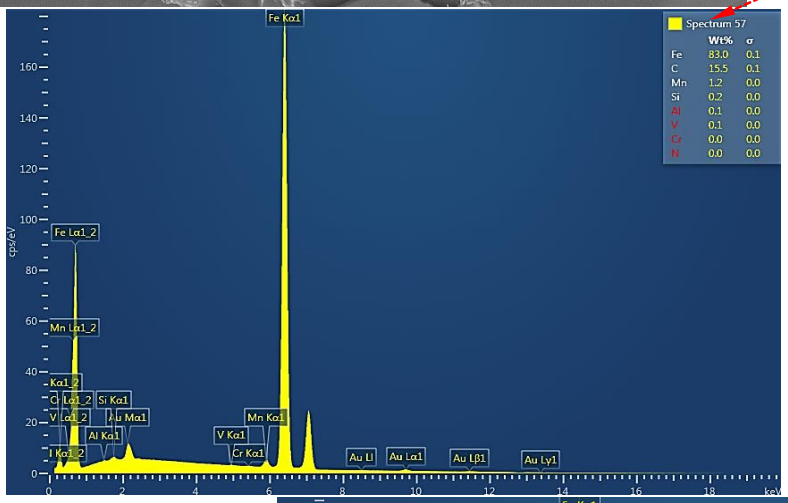
Element	Wt%	Wt% Sigma
C	9.82	0.13
N	0.21	0.21
Al	0.12	0.01
Si	0.20	0.01
V	0.10	0.01
Cr	0.04	0.01
Mn	1.5	0.0
Fe	88.1	0.2
Total:	**100.00**	



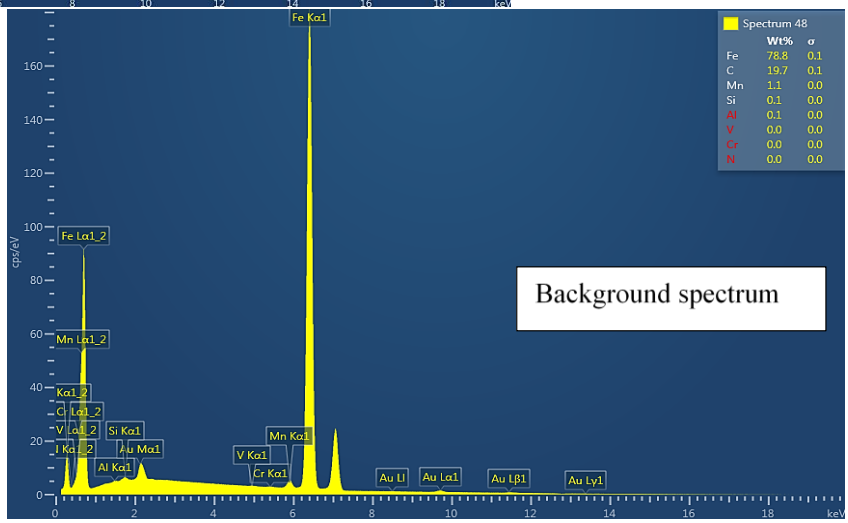
(c)







Element	Wt%	Wt% Sigma
C	15.5	0.13
N	0.00	0.00
Al	0.13	0.01
Si	0.20	0.01
V	0.10	0.01
Cr	0.01	0.01
Mn	1.22	0.0
Fe	83.0	0.1
Total:	**100.00**	



(d)

Figure 8.8: SEM-EDS spectra analysis of precipitates in the ferrite matrix for the heat treated NbTiV and VN-steels. **(a)** NbTiV, IAHT; **(b)** NbTiV, DAHT; **(c)** VN, IAHT; **(d)** VN, DAHT.